Characterization and modelling of the mechanical properties of mineral wool

Chapelle, Lucie; Brøndsted, Povl; Kusano, Yukihiro; Foldschack, Mathilde Rosendahl; Lybye, Dorthe ; Lévesque, Martin

Publication date:
2016

Lucie Chapelle

Characterization and modelling of the mechanical properties of mineral wool

PhD thesis, May 2016

DTU Wind Energy
Department of Wind Energy

ROCKWOOL®
FIRESAFE INSULATION

Preface

This thesis is submitted to the Technical University of Denmark in candidacy for a degree of Doctor of Philosophy, PhD, in applied mechanics. The work is prepared in accordance with the regulations regarding the industrial PhD programme in Denmark.

The topic treated is the characterization of mineral wool materials and modelling of the mechanical properties with emphasis on the compression behaviour. The application in focus is mineral wool products for thermal and acoustic insulation of buildings. Basic knowledge on mechanics, fibres materials, tomography and finite-element methods are assumed. The work presented was carried out in collaboration between the Technical University of Denmark, Department of Wind Energy, Section of Composites and Material Mechanics, ROCKWOOL International A/S, Group Research and Development and the École Polytechnique de Montreal (during the period from September 2014 to December 2014).

Research funding was provided from Innovationsfonden (E-grant no. 1355-00010B) and CINEMA: "the allianCe for ImagiNg of Energy MAterials", DSF-grant no. 1305-00032B under "The Danish Council for Strategic Research". The project has been supervised by Professor Povl Brøndsted (DTU Wind Energy), Senior Researcher Yukihiro Kusano (DTU Wind Energy), Project Manager Mathilde Rosendahl Foldschack (ROCKWOOL International A/S), Programme Manager Dorthe Lybye (ROCKWOOL International A/S) and Professor Martin Lévesque (École Polytechnique de Montreal) during the external stay.

The thesis consists of a full dissertation along with two conference papers and a journal paper under preparation.

Lucie Chapelle

København, 30 April 2016

Acknowledgements

A lot of people have kindly offered their guidance and support during the years, and this section expresses my gratitude.

First of all, I would like to thank my supervisors Povl Brøndsted and Yukihiro Kusano for fruitful discussions and valuable inputs, in addition to pleasant company. Throughout the PhD, they have been a constant source of support.

I wish to acknowledge my industrial supervisors Mathilde Rosendahl Foldschack and Dorthe Lybye for their trust and encouragement throughout the PhD. At all time, they have been available to guide me. Their dedication and enthusiasm for research have been an inspiration for me.

I owe personal thanks to my GD colleagues and in particular my fellow Young Professionals for interesting collaboration, pleasant working environment, and enjoyable company. I am indebted to the employees at section of Composite and Material Mechanics for providing valuable discussions and technical assistance with the experiments.

Special thanks go to my office mates from Hønsegården at Risø: Justine, Helga and Kristine. It has been great fun to share an office with you.

The acquisition of X-ray CT data was facilitated by Carsten Gundlach and his fantastic team at the DTU Imaging Portal. I would like to address them a special thank for helping me with data acquisition and analysis. Special thanks as well to Lars Pilgaard Mikkelsen (DTU Wind Energy) for his expert advice on FEM and valuable inputs.

Part of the work done in the thesis was conducted abroad during a research stay at the École Polytechnique de Montréal. The stay would not have been possible without the entry provided by Leon Mishnaevsky, thanks. Furthermore, I express my gratitude to Martin Lévesque for welcoming me at the Laboratoire Mécanique Multi-échelle.

Without the kind support from CINEMA and Innovationsfonden, the project would not have come into consideration, and the financial aid is appreciated.

Finally, heartfelt thanks go to my family (Moune, Papou and Tom) and Jesper for all your love and support as well as reminding me that there is a life besides the PhD.

Abstract

Mineral wool designates a highly porous network of fibres drawn by spinning molten minerals. Traditionally, mineral wool products have found application as thermal and acoustic insulation of buildings. Recent concepts where mineral wool products are subjected to higher structural loads have emerged and as a consequence focus on the mechanical properties of mineral wool has intensified. Also understanding the deformation mechanisms during compression of low density mineral wool is crucial since better thickness recovery after compression will result in significant savings on transport costs. The mechanical properties of mineral wool relate closely to the arrangement and characteristics of the fibres inside the material. Because of the complex architecture of mineral wool, the characterization and the understanding of the mechanism of deformations require a new methodology.

In this PhD thesis, a methodology based on image analysis to characterize the 3D structure of mineral wool materials in terms of fibre orientation, fibre diameter, contacts and pore size is proposed. The method uses 3D data obtained by X-ray tomography. The measured data are fitted to probability distributions in order to facilitate the comparison of individual characteristics of different mineral wool materials and provide simple descriptors of the 3D structure. All the methods described here are applied to glass wool and stone wool.

By developing a FEM model including the real characteristic of the mineral wool fibre structure, the effect of the structure on mechanical properties can be explored. The size of the representative volume elements for the prediction of the elastic properties is determined for two types of applied boundary conditions. For sufficiently large volumes, the predicted elastic properties are consistent with results from the literature and confirm the transverse isotropy of mineral wool.

Finally, the overall methodology is applied to study the compression of mineral wool products. X-ray tomography and the developed image analysis techniques are employed to quantify the change of the fibre structure under compression and confirm the reorientation of the fibres. A numerical model of the cyclic compression of mineral wool is developed and reproduces successfully the hysteresis observed experimentally. The results of the modelling indicate that the size of the hysteresis is linked to the friction coefficient between the fibres.

Elastic and compressive properties of mineral wool products can now be predicted and optimized with respect to the fibre structure, binder and fibre content using the micromechanical FEM model developed in this PhD study.

Resumé

Mineraluld er et meget porøst netværk af fibre, som er trukket ved at spinde smeltede mineraler. Traditionelt bruges mineraluldsprodukter til at isolere bygninger, både termisk og akustisk. I nyere koncepter udsættes mineraluldsprodukter for højere strukturelle belastninger, og derfor er fokus på de mekaniske egenskaber af mineraluld intensiveret. Forståelse af deformationsmekanismerne under kompression af højdensitets mineraluld er essentiel, da store besparelser kan opnås på transportomkostninger, hvis produkter kan komprimeres mere uden, at den endelige tykkelse reduseres. De mekaniske egenskaber af mineraluld har en tæt relation med konfiguration og karakteristika af fibrene i materialet. Grundet mineralulds komplekse mikrostruktur kræver karaterisering og forståelse af mekanismerne under deformation en tilpasset metode.

I denne PhD afhandling forelægges en metode baseret på digital billedanalyse, hvis formål er at karakterisere 3D strukturen af mineraluld, specifikt fiberorientering, fiberdiameter, kontaktpunkter og størrelse af porer. Metoden benytter sig af 3D billeddata erhvervet med computer tomografi. Billeddata fittes til statistiske fordelinger for at kunne sammenligne individuelle karakeristiska af forskellige mineraluldsmaterialer og for at finde simple deskriptorer af 3D strukturen. Alle metoder beskrevet i denne afhandling anvendes på glasuld og stenuld.

Ved at udvikle en FEM model, der inkluderer den sande karakteristik af fiberstrukturen i mineraluld, kan forbindelsen mellem fiberstrukturen og de mekaniske egenskaber udforskes. Størrelsen på det repræsentative rumelement (RVE), som benyttes til forudsigelse af de elastiske egenskaber, bestemmes for to typer af randbetingelser. For tilpas store voluminer er de forudsigede elastiske egenskaber konsistente med resultater fra litteraturen og bekræfter den transverse isotropi af mineraluld.

Afslutningsvis anvendes den overordnede metode til undersøgelse af kompression af mineraluldsprodukter. Computer tomografi og de udviklede billedanalyse-teknikker anvendes for at kvantificere ændringer på fiberstrukturen under kompression og for at bekræfte re-orienteringen af fibrene. En numerisk model af den cykliske kompression af mineraluld er udviklet og reproducerer den samme hysterese som observeret eksperimentelt. Resultaterne af modelleringen indikerer, at størrelsen på hysteresen er forbundet til friktionskoefficienten mellem fibrene. Elastiske og kompressive egenskaber af mineraluldsprodukter kan nu forudsiges og optimeres med henblik på fiberstrukturen, binder og fiberindhold vha. den mikro-mekaniske FEM model udviklet i denne PhD.

Table of Contents

1 Introduction

1.1 Background and motivation

Mineral wool is the general name attributed to fibre materials that are formed by spinning or drawing molten minerals. Typical applications include thermal insulation, soundproofing, filtration and hydroponic growth medium. Recently, composites materials where the mineral wool fibres act as a reinforcement have been developed [1–3]. Three main types of mineral wool are produced:

- Stone wool produced from volcanic rocks
- Glass wool whose raw materials include sand and recycled glass
- Slag wool obtained from the recycled products of blast furnaces.

The focus of this thesis is set on stone wool and glass wool. A summary of the production process is given here in order to better understand the origin of the fibre structure.

1.1.1 Production of stone wool

Stone wool fibres are obtained after melting volcanic rocks at high temperature (~1500°C) and pouring the melt through a cascade spinning process. Cascade spinning designates the assembly of several rotating wheels installed in series. The melt is drawn into fibres under the action of the high rotational field created by the spinning wheel. The diameter of the fibres is a function of the speed of the wheels and the viscosity of the melt. A typical value for the mean fibre diameter is 3 μm. During the fiberization process, droplets of melt of a few hundred micrometres are created. These melt inclusions are called shots in the stone wool production industry and they are an undesired defect inherent to the cascade spinning process. In the spinning chamber, a mixture of water, binder and silane is sprayed onto the fibres. The binder is the organic resin that creates the bonds in the stone wool product. The silane is a coupling agent added to improve the adhesive between the inorganic fibres and the organic binder. The fibres are then collected in a web, laid down by a pendulum onto a conveyor belt and brought to the curing oven where the binder is cured at approximately 200°C. The stone wool is then cut to shape and packed. An illustration of the overall process is given in Figure 1.1, left.

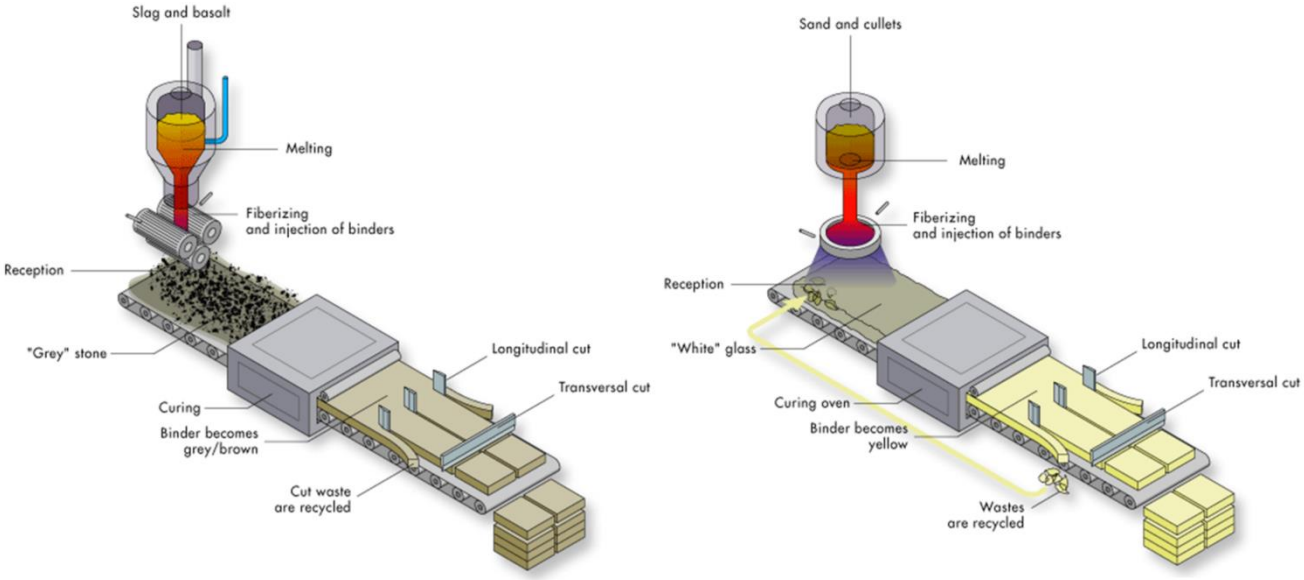

Figure 1.1: Left: Production of stone wool. Right: Production of glass wool (from [4]).

1.1.2 Production of glass wool

The production of glass wool shares some similarities with the production of stone wool. The main differences take place during the melting and fiberization process. The raw materials for glass wool fibres are melted at a temperature of 1300°C in an electric furnace. The melt is then propelled through thin holes of about 1 mm diameter each in a centrifugal cup spinner rotating around a vertical axis. The melt is centrifugally pushed through these holes and divided into several streams. A strong jet of hot gases parallel to the outer size of the cup realise then the final drawing of the melt into fibres. The fibres are sprayed with a binder and shaped into mats. The mats are then cured, cut and packaged. It should be noted that no shots are formed during the cup spinning process. The diameter of the glass wool fibres typically varies from 1µm to 10 µm. The overall process is illustrated in Figure 1.1, right.

1.1.3 Relations between the mineral wool structure and the mechanical properties

The properties of mineral wool relate closely to the individual properties of the constituents of the network (fibre and binder) but also to the structure of the fibres inside the products. For example, the orientation of the fibres is known to have a strong impact on the mechanical properties of the mineral wool products. Collection of the fibres during production results in a laminar structure of the mineral wool product and therefore a poor resistance to delamination especially for glass wool where a highly laminar structure is obtained. The mechanical performance of the product

can be tailored by reorienting the layers in the vertical direction by compressing the product in direction of the line and vertically.

In recent years, the focus on the mechanical properties of mineral wool products has intensified. This is partly due to the development of new concepts where mineral wool components act as a load bearing structure in a construction [5]. Gaining knowledge of the relationship between the fibre structure and the mechanical properties will enable the optimization of these new concepts and avoid over-dimensioning the mineral wool products and enable new applications. Another challenge dealing with the mechanical performance of mineral wool is the compression behaviour. When compressed, the mineral wool products do not regain their original thickness. The extent of the thickness recovery is more significant for stone wool products than for their glass wool counterparts. In order to understand the difference in the mechanical response of the two materials under compressive loads, the fibre structure of both materials should be investigated and characterized. Because of the stochastic nature of the material and the complex arrangement of the fibres, the quantification of the fibre structure requires the use of novel imaging techniques where data can be visualized in three dimensions. X-ray computed tomography is a technique providing sufficient resolution to visualize fibres which are only a few micrometres in diameter on an imaged volume large enough to obtain a representative view of the material. In order to fully investigate the link between the fibre structure and the mechanical properties, the outputs of the characterization can be converted into a set of statistical parameters and fed as inputs to a model describing the fibre structure accurately. Virtual testing of the material can then be conducted and valuable information about the role of each single input to the model can be extracted. For a specific application, one can optimize the mechanical performance of the mineral wool product by controlling the fibre structure inside the material. Such study would lead to a deeper understanding of the effect of the fibre structure and indirectly the impact of the factory production settings on the final product properties.

1.2 Scope

Products from two of the main manufacturer of mineral wool products, ROCKWOOL and Isover, are considered. The focus is set on the quantification of the fibre structure and the link to the elastic stiffness and compression properties of the products.

The fibre structure is quantified using mainly 3D imaging techniques in terms of:

- Fibre orientation

- Fibre and shot diameter distribution
- Pore size distribution
- Fibre volume fraction
- Fibre contact points

Elastic properties are investigated through 3D micromechanical modelling of virtual geometries representatives of the real fibre structure of mineral wool. The influence of several parameters on the elastic properties are evaluated:

- Fibre main orientation
- Fibre curvature
- Stiffness of the binder

The compression of mineral wool products is studied experimentally through dynamic cyclic loading and in-situ tests where static compression testing is combined with 3D imaging. Analytical models are fitted to the experimental data and a 3D micromechanical FEM model where a cyclic compression case can be simulated is developed.

1.3 Outline of the thesis

Chapter 2 focuses on the characterization of the fibre structure of mineral wool products using microscopy and X-ray computed tomography. The techniques employed for the investigation of the fibre structure are detailed and the data analysis developed for the extraction of the relevant characteristics of the fibre structure is given.

In Chapter 3, the algorithm for the generation of a random fibre network representative of the real fibre structure of a mineral wool product is developed.

Computing of the elastic properties of the generated fibre network in presented in Chapter 4 where the size of the volume representative of the real mineral wool product is evaluated and the influence of the fibre structure parameters on the elastic properties is studied.

Finally, Chapter 5 deals with the compressive behaviour of mineral wool. In this chapter, the elastic model of Chapter 4 is developed further to simulate the compressive behaviour of mineral wool products under large strains. Experimental results including in-situ compression tests in the X-ray computed tomography scanner are described and support the findings of the model.

2 Characterization of the mineral wool fibre structure

This chapter deals with the characterization of the fibre structure in mineral wool materials. The estimation of fibre orientation, fibre diameter and pore distribution is included and the determination of the number of contacts between the fibres is described. First a study with the scanning electron microscope (SEM) is conducted on a stone wool sample but this method does not result in a quantitative characterization of the fibre structure. Nevertheless the SEM appears to be a valuable tool to collect qualitative information on the condition of the fibre and the binder. To obtain a quantification of the mineral wool fibre structures, 3D data from X-ray computed tomography are analysed for a glass wool and a stone wool sample. The analysis of the 3D data reveals that the fibre structures of stone wool and of glass wool present some significant differences in terms of fibre orientation, diameter and pores distribution. Most of the methodology dealing with X-ray computed tomography available in this Chapter is also presented in paper [P1] where a similar study was conducted on a stone wool sample.

2.1 Scanning electron microscope study

Numerous studies of mineral wool fibres using an SEM are available in the literature [6–9]. The aim of these studies is to determine the dissolution rate of mineral wool fibres in different media and conditions. For such experiments, the imaged sample consists of a few fibres often cut in several pieces. In the present work, the aim is to characterize the mineral wool fibre structure inside a product. For that reason, the sample preparations adopted in this work are very different from the ones presented in the literature.

The microscope used is the environmental SEM Philips XL30. A sample can be examined in its natural state in a gaseous environment at partial pressure as high as 1330 Pa if necessary. Both partial pressure and high vacuum mode are used in this study. Typical values for the working distance are 10 mm in high vacuum mode and 5 mm for partial pressure mode. In high vacuum mode, images with BSE (backscattered electrons sensitive to chemical contrast) and SE (secondary electrons sensitive to topographic contrast) detectors are acquired. In partial pressure environment,

only the SE detector is available. In this work, the observation of mineral wool fibres with the SEM is limited to stone wool.

Samples are prepared by cutting a small volume from a stone wool product and fixing it onto a microscopy stub. The stub is gold coated in order to avoid the build-up of charges on the surface of the sample so that high acceleration voltages can be used (20 keV). The first observations in high vacuum mode confirm that the fibres have a high aspect ratio (as observed at the macroscopic scale) and are arranged in a complex manner. The image on the left of Figure 2.1 is representative of the fibre structure inside a stone wool product. It is almost impossible to follow one fibre from one end to another due to the high aspect ratio of the fibre and the degree of entanglement of the fibre network. It is also noticed that the fibre diameter is not constant and range from a few micrometres to a few dozen micrometres.

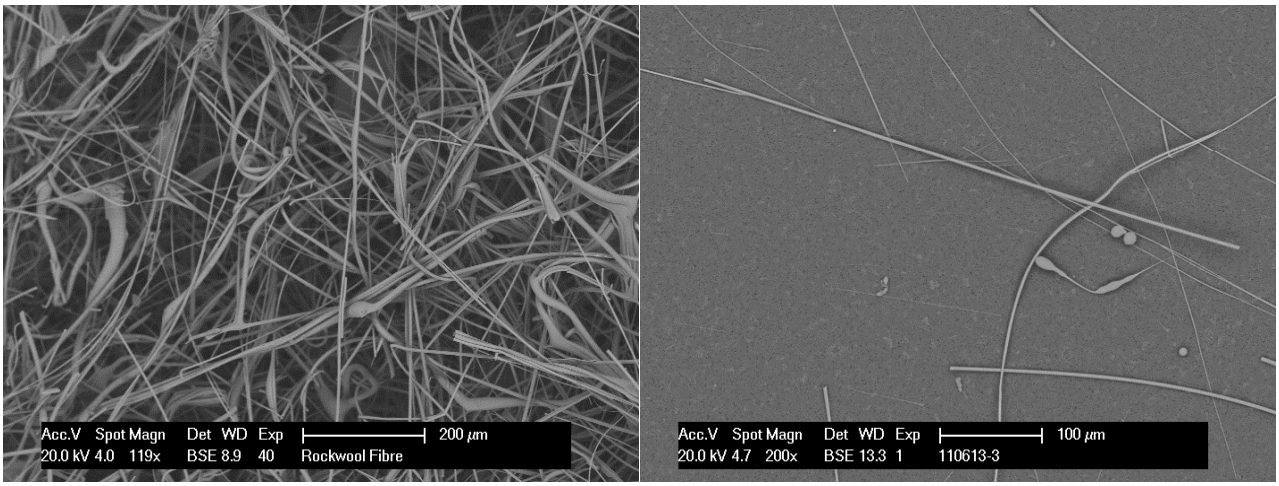

Figure 2.1: Observation of stone wool fibres in a SEM (high vacuum).

In a different sample preparation, tufts of fibres are carefully extracted from loose wool in which the binder had been burned off. The tuft is dispersed into a solution and filtered on a membrane. This ensures that the fibres are scattered onto the surface. The membrane with the fibres is placed on a stub, gold coated and placed in the SEM chamber. The images obtained by this sample preparation allow the observation of a fibre from end to end with very little entanglement (Figure 2.1, right). A quantification of the length and diameter is then possible. However, to limit the number of fibre crossings and to enable an automatic quantification of fibre diameter and length with image analysis, only a small volume of fibre is extracted and dispersed. The magnification is set to at least 200 times in order to visualize the thinnest fibres and several images need to be

acquired and stitched together to visualise the long thick fibre in their full length. This means that a large amount of samples would be required in order to have a representative population of fibres.

Charging effects are observed when a high magnification is used because the imperfect gold sputtering of the porous mineral wool. To solve this issue, t¨øufts of mineral wool fibres are also observed in partial pressure mode. No gold sputtering is applied but a partial water pressure is set in the SEM chamber to permit the evacuation of the charges building up at the sample surface. The acceleration voltage is reduced to 2 keV. The binder can be seen at the crossing between two fibres (Figure 2.2, left) and onto the fibre surface (Figure 2.2, left and right). The binder prints left on the surface of the fibre resemble a broken bond.

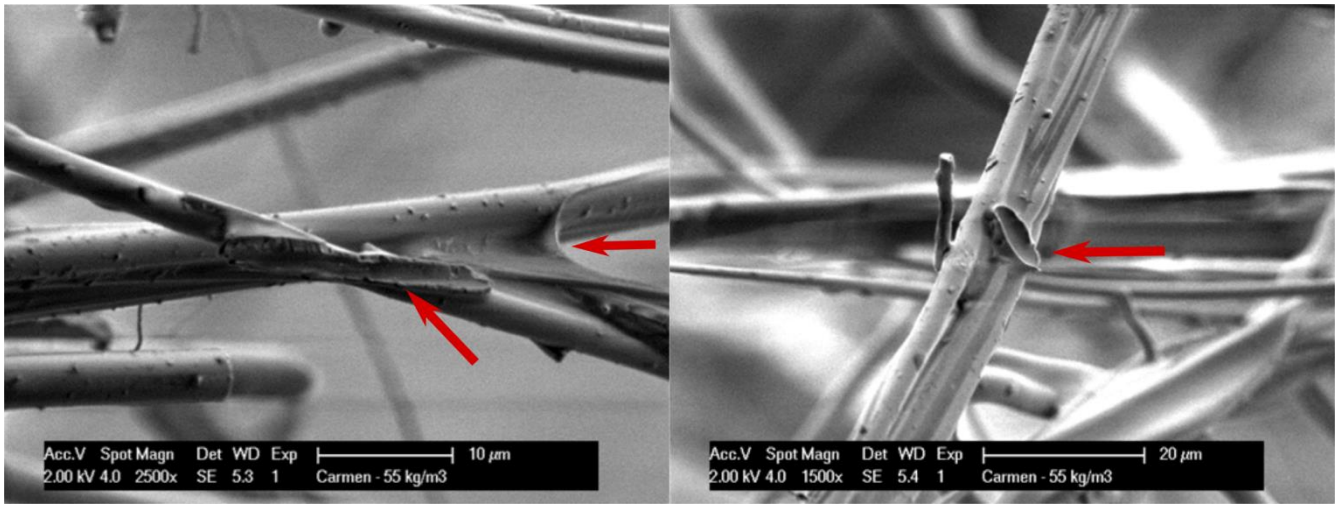

Figure 2.2: Observation of stone wool fibres in SEM (partial pressure). The red arrows indicate the presence of binder.

The conclusions of the SEM study are as following:

- Stone wool fibres have a high aspect ratio and a wide diameter and length distribution making it difficult to image them in their full length or select the appropriate magnification.
- The fibres arrangement in space and orientation distribution is complex and difficult to characterize based on 2D microscopy images.
- The binder can be visualized at high resolution and on a sample where no gold was sputtered. However, the microscopy images do not give any quantitative information about the distribution.

Based on the above points, it is concluded that in order to obtain a quantitative characterization of the structure of mineral wool fibres, acquisition of a third dimension is necessary and a different imaging technique is needed.

2.2 X-ray Computed Tomography (X-ray CT) study

3D structural data from a fibrous porous media can be obtained using X-ray CT. High resolution X-ray CT has gained considerable importance in the examination and 3D-characterization of materials and industrial specimens in the last decade [10–15]. Analysis of the X-ray CT data can provide important microstructural characteristics, for example, the orientation and the diameter distributions of the fibres [16]. For sub-micrometre resolution, an X-ray synchrotron setup is usually needed. In the recent years, however, the technology has evolved to the point where laboratory X-ray sources and optics are also able to produce data with sub-micrometre resolution. In section 2.2.1, a short survey on the use of X-ray CT to characterize random fibre network and composites is conducted and a presentation of the X-ray CT scanners and settings used to acquire the data in this work is given. The pre-processing step before the analysis of the data is also outlined.

2.2.1 Use of X-ray CT for the characterization of fibrous materials

In the field of textile research, where fibres are a part of the product, the yarn fibre direction has been estimated from the analysis of 3D X-ray micro CT data [17–21]. Eberhardt and Clarke introduced a technique to trace fibres in 3D datasets of composites and textile materials. The same technique is later implemented by Tausif et al. to measure the orientation of segments of fibres in nonwoven materials [22,23]. The complex structure of the fibre network in paper has also been investigated by X-ray CT where the fibre twist and aspect ratio were measured [24], and the anisotropy and the heterogeneity of paper materials have been studied using covariograms [25]. 3D X-ray micro CT of stone wool has been used for measuring the displacement field during deformation [26,27]. The deformation of the imaged sample of stone wool was correlated to its local density variations but no other quantifications were conducted.

2.2.2 Image acquisition and pre-processing

2.2.2.1 Laboratory scanner

The laboratory scanner used for the acquisition of 3D data is a ZEISS XRadia 410 Versa with a resolution of 1-50 µm in samples of size 1-50 mm. Typical power and energy values for the scanning of mineral wool were 80 keV and 10W.

2.2.2.2 Synchrotron beamline

Data are also acquired at the TOMCAT beamline for TOmographic Microscopy and Coherent rAdiology experimenTs of the Paul Scherrer Institute, Switzerland. High energy X-ray synchrotron micro-tomography provides high quality data in terms of signal to noise ratio and a high spatial resolution compared to laboratory equipment. Typical range for the photon beam energy is 12-18 keV.

2.2.3 Pre-processing

Every image contains some noise according to the imaging technique and the instrument set-up. When the amount of noise is significant, it is necessary to reduce the noise before further analysis of the microstructure. Linear filters, e.g. Gaussian filters, will blur the edges, which might lead to an overestimation of the size of the objects. Perona and Malik [28] proposed a local and adaptive smoothing method, called anisotropic diffusion filtering based on a nonlinear diffusion filter with reduced diffusion at locations which have a larger likelihood to be edges. It uses nonlinear evolution partial differential equations and seeks to improve images by removing noise while preserving details and even enhancing edges. The result of the application of an anisotropic diffusion filter on a reconstructed slice of a scan of a glass wool sample is illustrated in Figure 2.3.
By comparing the slice of a dataset before and after the anisotropic diffusion process, it is observed that the grayscale values of the background are more homogeneous and the noise is reduced significantly. The filtered image gives sharper peaks for the background and the fibre when the histogram of the grey values is computed.
In the next section, techniques for the characterization of the acquired and pre-processed dataset are discussed.

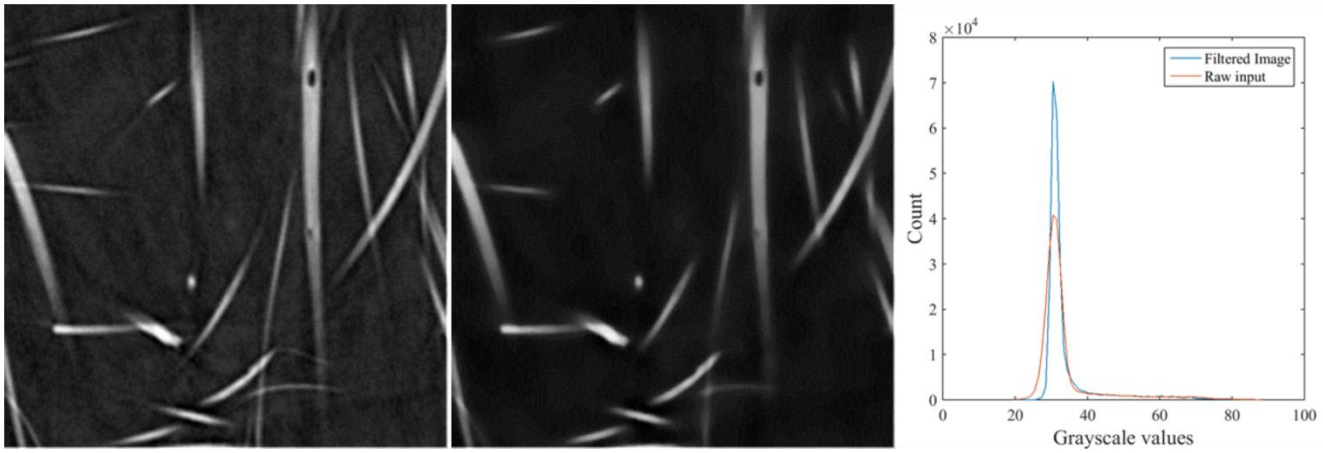

Figure 2.3: Left: Raw slice of a 3D dataset. Middle: Same slice denoised using an anisotropic diffusion filter. Right: Histograms of the gray values before and after the anisotropic diffusion.

2.3 Method to determine the fibre orientation

Another important characteristic of mineral wool materials is the fibre orientation. Mineral wool fibres are not necessarily straight and can present different degree of curvature. For that reason, the image analysis presented here aims to characterize the local orientation of a fibre as the orientation along the fibre centreline is susceptible to change.

The changes of orientation in an image are indicated by the patterns of intensity variations. The first order intensity variation is the gradient. To obtain the main orientation, one must average the local orientation and ensure that gradient vectors pointing in opposite directions do not cancel out but enhance each other. The gradient structure tensor, first introduced by Bigun and Granlund [29], overcomes this problem by computing the local gradient in a quadratic form. The gradient structure tensor has successfully been used for object tracking, texture segmentation, flow estimation as well as orientation of complex patterns such as fingerprints [30–33].

2.3.1 Definition of the gradient structure tensor

The gradient structure tensor is a tensor representation of the inner product of the partial derivatives of the image. The image partial derivatives can be obtained by convolving the input image with a discrete approximation of Gaussian derivative filters where the width of the Gaussian window defines the inner or local scale. Using Scharr kernel [34] is an alternative approach. Scharr operators are recognized as more accurate than other common derivative operators. The gradient structure tensor is defined as:

$$J(x,y,z) = \begin{bmatrix} \langle f_x, f_x \rangle_\rho & \langle f_x, f_y \rangle_\rho & \langle f_x, f_z \rangle_\rho \\ \langle f_x, f_y \rangle_\rho & \langle f_y, f_y \rangle_\rho & \langle f_y, f_z \rangle_\rho \\ \langle f_x, f_z \rangle_\rho & \langle f_y, f_z \rangle_\rho & \langle f_z, f_z \rangle_\rho \end{bmatrix} \tag{2.1}$$

where f_i is the derivative of the image f in the direction i and the weighted inner product between two images g and h is defined as:

$$\langle g, h \rangle_\rho = K_\rho * (g \cdot h) \tag{2.2}$$

where $*$ denotes the convolution operator, $\cdot$ the inner product and K_ρ is the Gaussian weighting function that averages the orientation within a neighbourhood. The integration scale ρ reflects the characteristic size of the texture considered. Once the structure tensor has been obtained for each voxel over a neighbourhood defined by the scale ρ, the eigenvalues and eigenvectors are determined. The eigenvalues are ordered, i.e. $\lambda_i \geq \lambda_{i+1}$. The eigenvector e_3 corresponds to the smallest eigenvalue λ_3 and hereby corresponds to the orientation with the lowest fluctuations. For voxels belonging to a fibre, this will give the orientation of the fibre locally.
The orientation of each eigenvector e_i can be described by two angles, the elevation angle θ and the azimuth angle ϕ as follows:

$$e_i = \begin{Bmatrix} e_x \\ e_y \\ z \end{Bmatrix} = \begin{Bmatrix} \cos\theta \cos\phi \\ \cos\theta \sin\phi \\ \sin\theta \end{Bmatrix}, \qquad \theta \in [0, \pi], \qquad \phi \in \left[-\frac{\pi}{2}, \frac{\pi}{2}\right] \tag{2.3}$$

2.3.2 Scale dependency

A simple system of two straight fibres perpendicular to each other was generated in order to study the dependency of the scale parameter ρ of the structure tensor on the orientation determination. For each voxel of the generated straight fibres, the true orientation is known. The error between the measured and true orientation is estimated for different scales by calculating the mean deviation angle between the real direction and the measured one and finding the minimum for the interval considered. It is observed that the scale parameter of the Gaussian filter ρ scaled up with the radius of the fibre r and the minimal error between the true and the measured orientation was obtained when $\rho = r$.

2.3.3 Test on a large number of fibres

In order to validate the methods for the orientation, artificial data with known fibre orientation are generated using a fibre volume fraction and an aspect ratio close to the expected value for a mineral wool fibre network and three different orientation distributions: preferentially unidirectional, 3D random and 2D random (Figure 2.4). More details on the generation of such networks are given in Chapter 3.

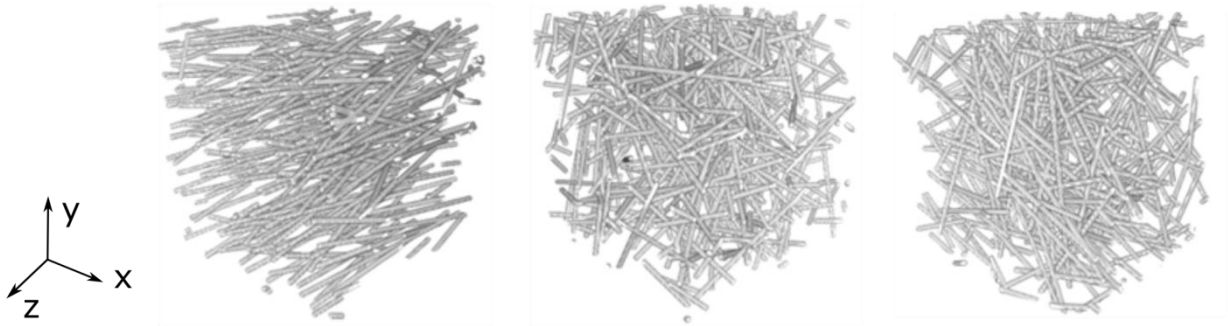

Figure 2.4: Generated fibre networks. Left: unidirectional, middle: 3D random and right: 2D random.

The structure tensor is computed for grayscale dataset and from this the azimuth and elevation angles are extracted. The value of each angle is correlated to a colour. The results of the mapping are given in Figure 2.5 for the three fibre networks.

The orientation information can also be visualized in a histogram projected onto the unit sphere. The number of occurrences of each discrete orientation (θ, φ) is calculated and interpolated onto a uniform grid. The grid is then projected onto the sphere using the expression of the surface element on a spherical surface dS_r at constant radius r spanning from θ to $\theta + d\theta$ and φ to $\varphi + d\varphi$:

$$dS_r = r^2 \sin(\theta) d\theta d\varphi \tag{2.4}$$

In Figure 2.6, the histograms using the orientation vectors entered as inputs and returned by the eigenvalues analysis of the structure tensor are given. It is observed that the two orientation distributions corroborates well for each type of generated fibre networks.

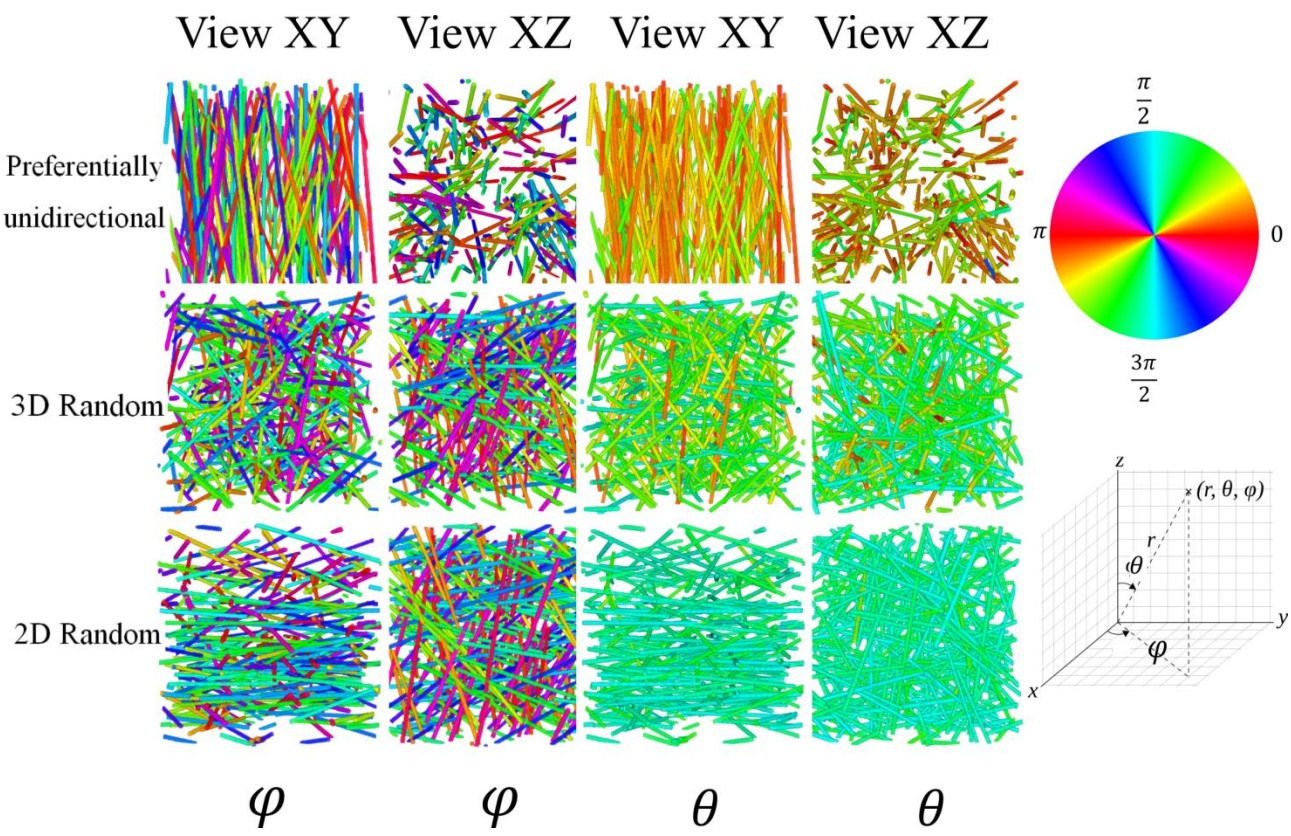

Figure 2.5: Local orientation map of the elevation and azimuthal angles of the virtual data.

To confirm these observations, the mean angle of deviation between the generated orientation vectors and the estimated orientation vectors are calculated. The results are given in Table 2.1 and confirm that the method is suitable for the estimation of the orientation of real mineral wool fibres networks.

Table 2.1: Deviation between the real generated and the estimated orientation vectors.

Fibre orientation	**Mean angular deviation [rad]**
Preferentially unidirectional	0.16
3D random	0.08
2D random	0.04

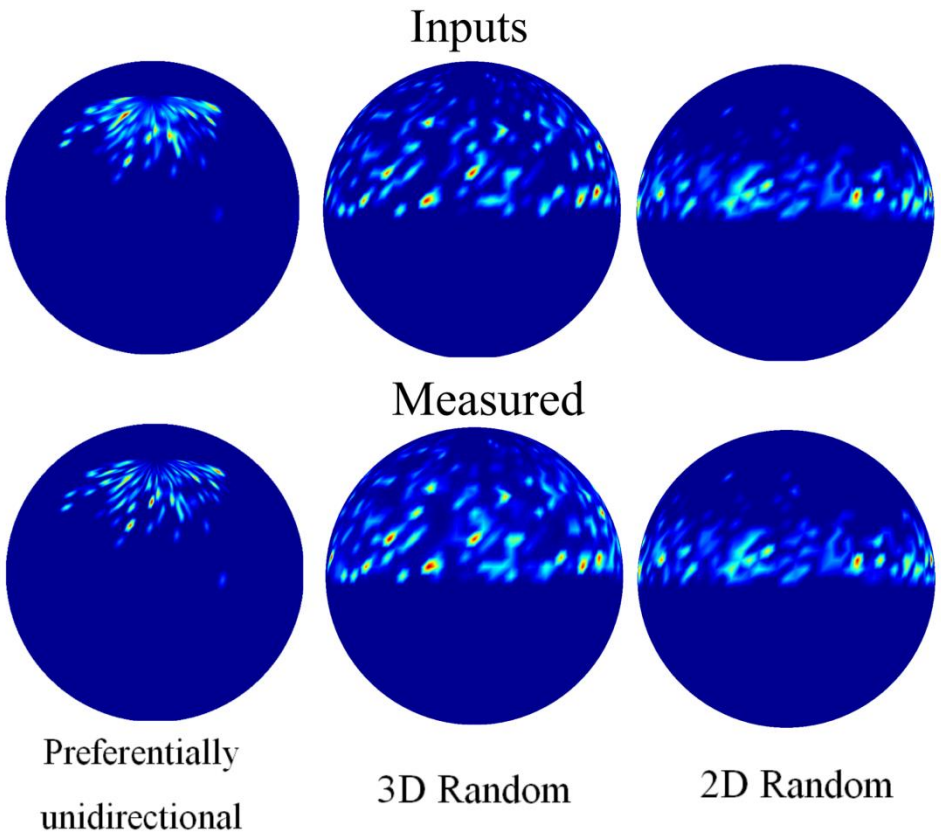

Figure 2.6: Histograms of the distribution of orientations visualized onto a unit sphere.

2.4 Method to determine the fibre diameter

The fibre diameter is an important characteristic of mineral wool and can be linked to various physical properties. Manual measurement of the fibre diameter is a long and tedious work and often unreliable. This is why the automatic characterization of the fibre diameter via image analysis is worth pursuing. The image analysis for the fibre diameter estimation that is presented below is based on morphological operations.

The diameter distribution of the fibres is estimated using grey level morphological granulometry, which has several advantages compared to the binary granulometry. A granulometry is a sequence of openings with convex structuring elements of increasing size that simulates a sieving procedure with increasing mesh width. Distribution of dimensions in an image can be obtained by granulometry. The majority of the granulometry methods in the literature requires the conversion of the greyscale image into binary [14,35–37] which yields a loss of information. The principle of a binary granulometry is described below before moving to its implementation for greyscale images.

Size distribution analysis for a binary image can be carried out in the following way. For a binary image after an erosion operation, the voxels belonging to the foreground (in this case, the fibres) shrink in size. If the size of the shrinkage (determined by the size of the structuring element n) is superior to the size of an object belonging to the foreground, this object disappears completely. If the size of the object is larger than the size of the structuring element, the eroded object remains and a subsequent dilation operation of size n restores the object to its initial shape and size. By measuring the number of voxels remaining after each erosion and dilation (i.e. measuring how many objects "disappears" after each step) as a function of the size of the structuring element n, a histogram can be obtained describing the volume fraction for each scale considered. Binary granulometry was successfully applied to medium density fibreboard (MDF) to determine the size distribution of fibres and of pores [36,38–40].

During the conversion from grayscale to binary images, some of the information is lost. For example, the voxels corresponding to the edge of the fibre are either set to the background or to the fibre and this will lead to errors in the estimation of the fibre diameter. It is therefore advantageous to work on grayscale images rather than binary when determining the fibre diameter in images with a low resolution. The method presented here is an implementation of the algorithm developed in [41] where the granulometry is modified to work on greyscale images.
For each voxel p of a greyscale image I, the pattern spectrum of a granulometry $PS_n(p)$ can be defined as:

$$\forall\, n > 0,\ \ PS_n(p) = \psi_n\big(I(p)\big) - \psi_{n-1}(I(p)) \tag{2.5}$$

where ψ_n is an opening with a structuring element of size n.
If the structuring element is a ball of radius n, the pattern spectrum carries information about the distribution of the diameter of the fibres. Commonly, the size of the object at a voxel $d(p)$ is expressed as the scale at which the pattern spectrum reaches its maximal value:

$$d(p) = 2\arg\max_n\left(PS_{\gamma_n}(p)\right) \tag{2.6}$$

However, for grayscale granulometry different maximum values can be reached at different scales. To take this effect into account, the methodology presented in [41] by Moreno et al. is adopted: the

size of an object is computed as a combination of the values of the pattern spectrum at different scales. Moreno et al. also include a parameter to correct the bias induced by the edge effect in the expression for the size of an object: the intensity of the voxels at the fibre edges reflects the fact that the edges are a mixture of the fibre and the background. Therefore, the voxels at the edges should contribute less to the measure of the diameter. The resulting expression for the size of an object at a voxel p belonging to I, $d(p)$ is:

$$d(p) = 2\frac{\sum n\, PS_{\gamma_n}(p)}{\sum PS_{\gamma_n}(p)} - \frac{M - I(p)}{M - m} \tag{2.7}$$

with M and m being the maximum and minimum intensities of the image I respectively. In the present work, the diameter of the fibre will be estimated using Eq. (2.7).

2.5 Method to determine the pore size

If interpreted correctly, the size of the pores can provide information about the distribution and arrangement of the fibres in the material. To investigate the pores size, image analysis of 3D data is employed.

By considering dark features over a bright background, one can apply the same granulometry technique described in section 2.4 to obtain information of the size distribution of the pore structure in stone wool materials. This has been applied successfully to determine pore size of cellular ceramics [14], of random fibrous networks [36] and of gas diffusion layers [42].

The pore size being quite large, neglecting the information contained in the edges contrast would not lead to a wrong estimation of the size of the pores. In this work, the binary granulometry is first attempted to obtain the size distribution of the pores and proved to be accurate but slow. This can be explained by two reasons. First, the morphological opening operation speed decreases with increasing structuring element size. Secondly, a larger range of values for the structuring element size was needed to be investigated when exploring the size distribution of the pores. Other methods were thus sought in the literature. Dougherty [43] has implemented in the open source image analysis software ImageJ a plug-in estimating the local thickness of an object in a 2D or 3D image. The algorithm uses the Euclidean distance transform. As it is significantly faster than the

granulometry, this plugin is a more suitable tool to estimate the pore size distribution of mineral wool materials.

2.6 Method for the fibre segmentation

To extract characteristics such as the number of contacts in the fibre network or the main orientation of the fibres from the 3D data, an additional step is needed. Indeed, the fibre should be isolated from the background and from each other in order to be further analysed. This process is known as segmentation. The background can be distinguished from the fibres using a simple thresholding method providing that the noise level has been reduced during the pre-processing of the data. To differentiate every individual fibre in the network, the skeleton of the fibres is obtained. In this section, the process to obtain the individual segmentation of the fibres from the skeleton is explained.

2.6.1 Skeletonization

The skeletonization process requires a binary image. During the application of the skeletonization process, a foreground voxel, i.e., a voxel belonging to a fibre is changed to a background voxel unless it belongs to the centreline of the fibre. At the end of the skeletonization, only paths with a thickness of one voxel should remain. In this work, the skeleton is obtained using the plugin developed by Beat Münch for ImageJ. The plugin is an implementation of the 3D thinning algorithm from Palagyi et al. [44].

2.6.2 Connectivity of the skeleton and voxels classification

The connectivity of a voxel belonging to the skeleton is defined as the number of voxels belonging to the 26 immediate neighbours which are non-zeros.

A voxel is classified to the following categories depending on its connectivity:

- End voxel (connectivity 1): the voxel has only one neighbour with a non-zero value.
- Branch voxel (connectivity 2): the voxel has exactly two neighbours with a non-zero value.
- Node voxel (connectivity 3 or larger): the voxel has at least three neighbours with a non-zero value.

The end voxels are often the voxel at the ends of the skeleton of a fibre but they can also be isolated voxels. The branch voxels belong to the centreline of the fibre and the nodes often represent the bond between two fibres. In reality, the node voxels also appear along a fibre centreline as a result

of noise or a fault in the skeletonization process. At the end of this step, three matrices E, B and N of the same size as the 3D data are generated. A voxel in E, B or N takes the value of one whenever it belongs to the skeleton and when it reaches the criteria for being respectively an end point, a branch voxel or a node voxel.

2.6.3 Skeleton segmentation

Noise present in the image and irregularities in the shape of the fibre can create spurious branches and nodes in the skeleton. In order to assign each branch of the skeleton to the centreline of a fibre, it is needed to clean the skeleton and remove the spurious branches and nodes. The first step of the skeleton segmentation is to assign a unique label to the voxels belonging to a same branch of a fibre and a unique label to all voxels belonging to the same node. This was carried out by applying the function "*bwconncomp"* in Matlab to matrices E, B and N. The function "*bwconncomp"* gives a unique label to the group of voxels which are connected. For each group of nodes, the closest groups of branches are identified and recombined if the branches belong to a same fibre. The criteria to recombine the branches rest on the determination of the alignment of the branches. The algorithm developed here is given in Table 2.2. When a recombination of two branches is performed, voxels are created to fill the gap between the two branches.

Table 2.2: Algorithm for the segmentation of the skeleton.

FOR i in NodeSet
    Find Neighbours within a 5 voxel radius
    Identify the labels of all branches in neighbourhood
    FOR j in BranchNeighSet
        Evaluate the dot product of the vector direction for each combination of branches in the neighbourhood
        Evaluate the dot product of the vector direction of a branch with the vector direction of the intersection
        IF product of dot products > 0.9
            Branches have same direction and can be reconnected
        ELSE
            No reconnection

2.6.4 Contact detection

A contact is detected whenever a node is linking at least two branches of two different labels. This step is carried out after the reconnection of branches.

2.6.5 Validation on a virtual fibre network

A virtual fibre network is generated with random fibre orientation and diameter distributions to test the method for the segmentation of the fibres. The fibres are modelled as cylinders. Figure 2.7 illustrates all the steps leading to the segmentation of individual fibres.

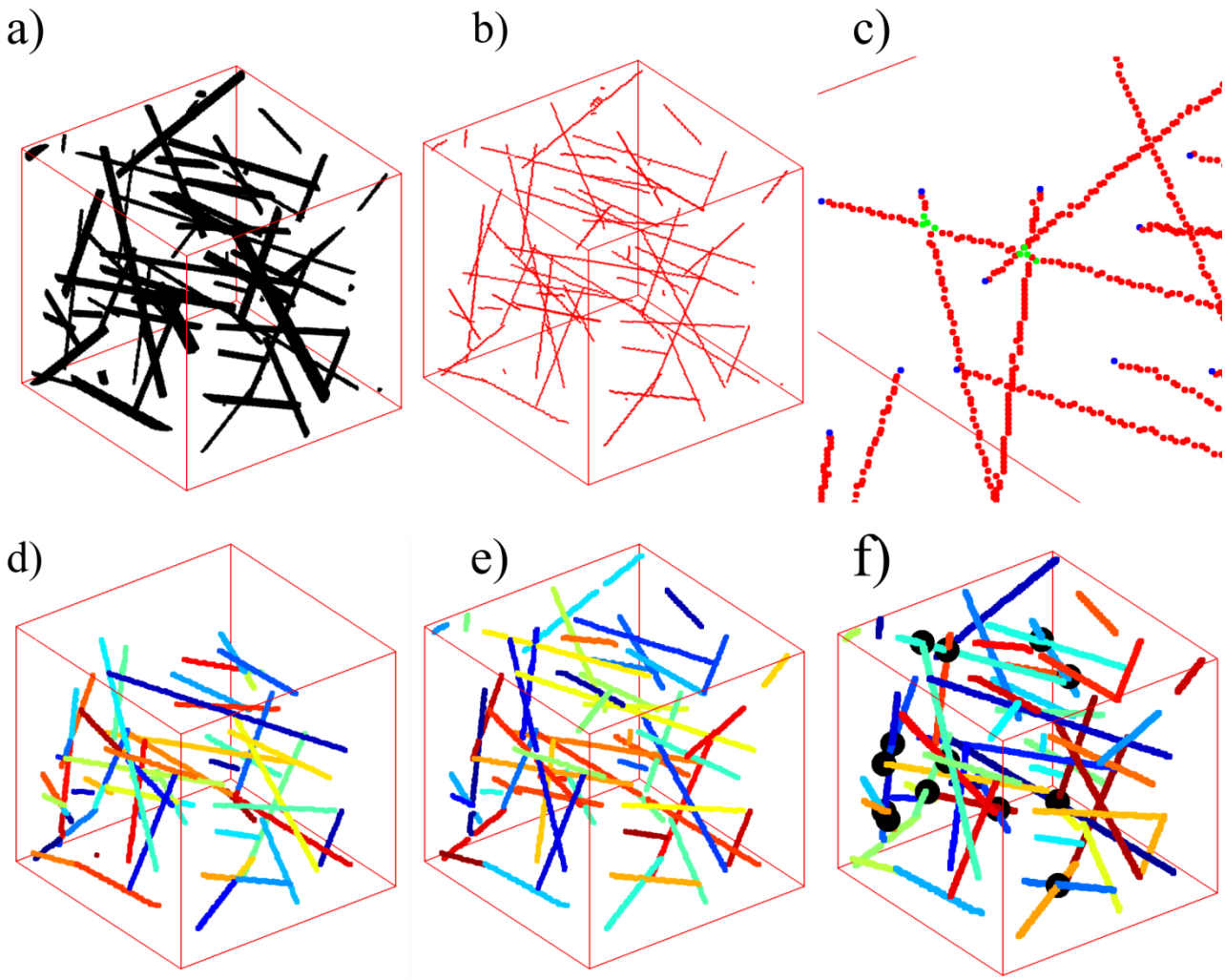

Figure 2.7: Illustration of the steps leading to the individual fibre segmentation. Details of the steps are given in the section 2.6.

Step a) is obtained after applying a global thresholding method to separate the background from the fibres. After step b), the skeleton can be obtained from the binary image. The step c) represents the same skeleton but the voxels have different values depending on their connectivity. In the Figure 2.7, image c) where the skeleton of the fibres is seen as smaller scale, the red voxels correspond to branch, blue to end points and green to nodes. Afterwards a labelling of the branches of the skeleton is performed in step d) using the function *"bwconncomp"* on the branch data. It should be noted that the fibres in the bottom corner of the cube have been disconnected and they become reconnected in step e) as they satisfied the alignment criteria. The final step f) shows the contacts in black dots.

2.7 Applications to mineral wool data

In this section, the aforementioned methods for the extraction of the relevant characteristics of the fibre network are applied to four real sets of data obtained by X-ray CT (Table 2.3).

Table 2.3: Characteristics of the scanned mineral wool samples.

Sample	Data identification	Density [kg/m^3]	Scanner	Voxel size [µm]
Glass wool	GW-A	15	Laboratory source	4.28
Glass wool	GW-B	15	Synchrotron source	0.33
Stone wool	SW-A	34	Synchrotron source	1.63
Stone wool	SW-B	34	Synchrotron source	0.33

2.7.1 Determination of the fibre orientation distribution of mineral wool

The structure tensor is computed for the dataset GW-A on a volume of [992 x 1014 x 1000] voxels or [4.25 x 4.34 x 4.28] mm^3 and for the dataset SW-A on two volumes of [1000 x 1000 x 1000] voxels or [1.63 x 1.63 x 1.63] mm^3. The two volumes from the dataset SW-A share the same x and y coordinate and successive z coordinate. The z-axis is parallel to the thickness of the product.

3D renderings of the datasets where the colours represent the variations of the azimuthal φ and elevation angles θ of the glass wool fibres and stone wool fibres are shown in Figure 2.8. It can be observed that the glass wool fibres present a more laminar structure than the stone wool fibre. Stone wool fibres arranged in tufts and sharing the same local preferential orientation can also be

distinguished. Individual histograms of the elevation angles and of the azimuth angles and a joint histogram of both angles on the unit sphere are shown in Figure 2.9. The histograms confirms that the fibres in glass wool and stone wool are preferentially oriented parallel to the x-y plane as described by the peak around $\pi/2$ in the distribution of the elevation angles in Figure 2.9.

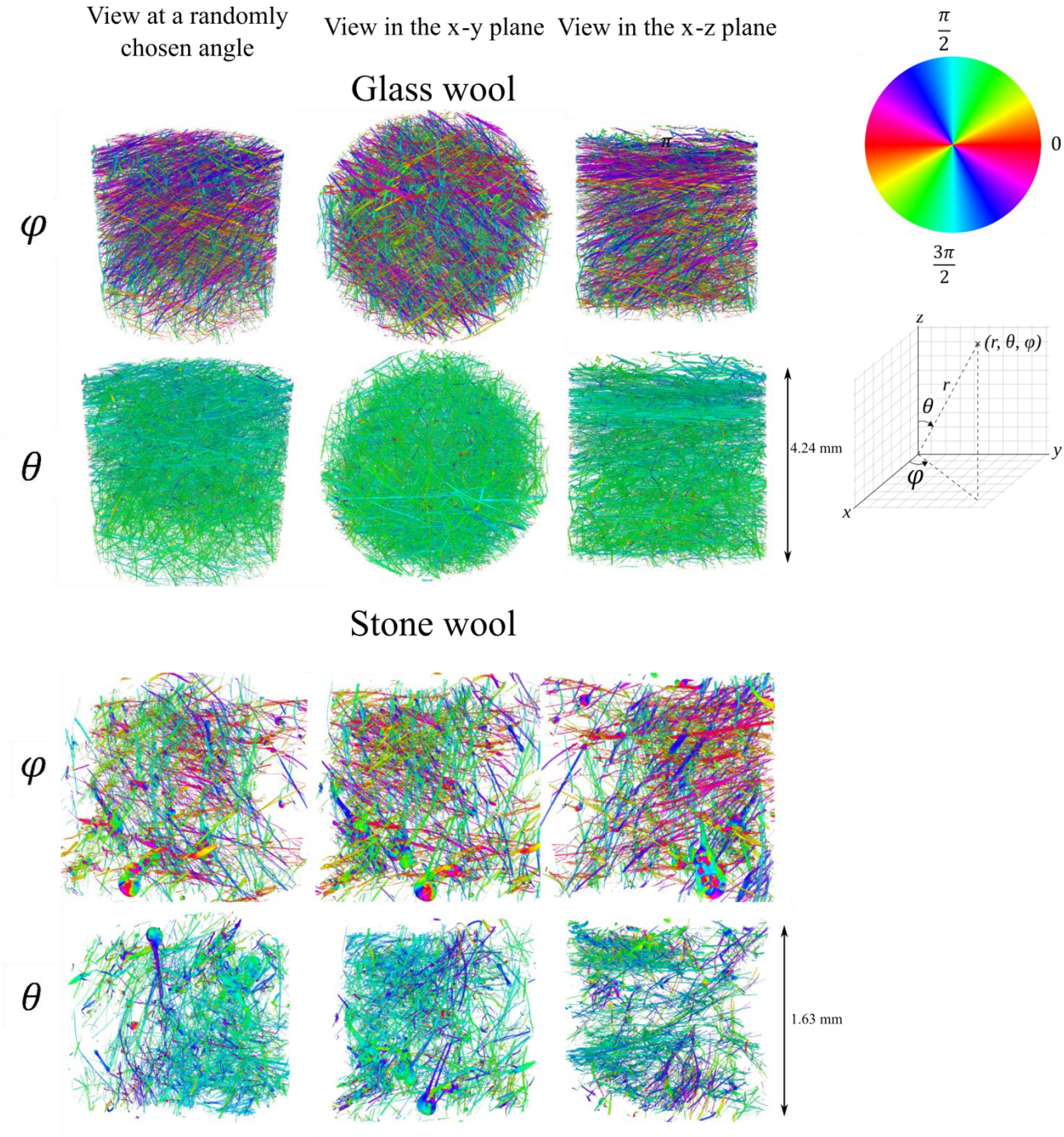

Figure 2.8: Local orientation map of the elevation and azimuthal angles of a glass wool sample (top) and a stone wool sample (bottom).

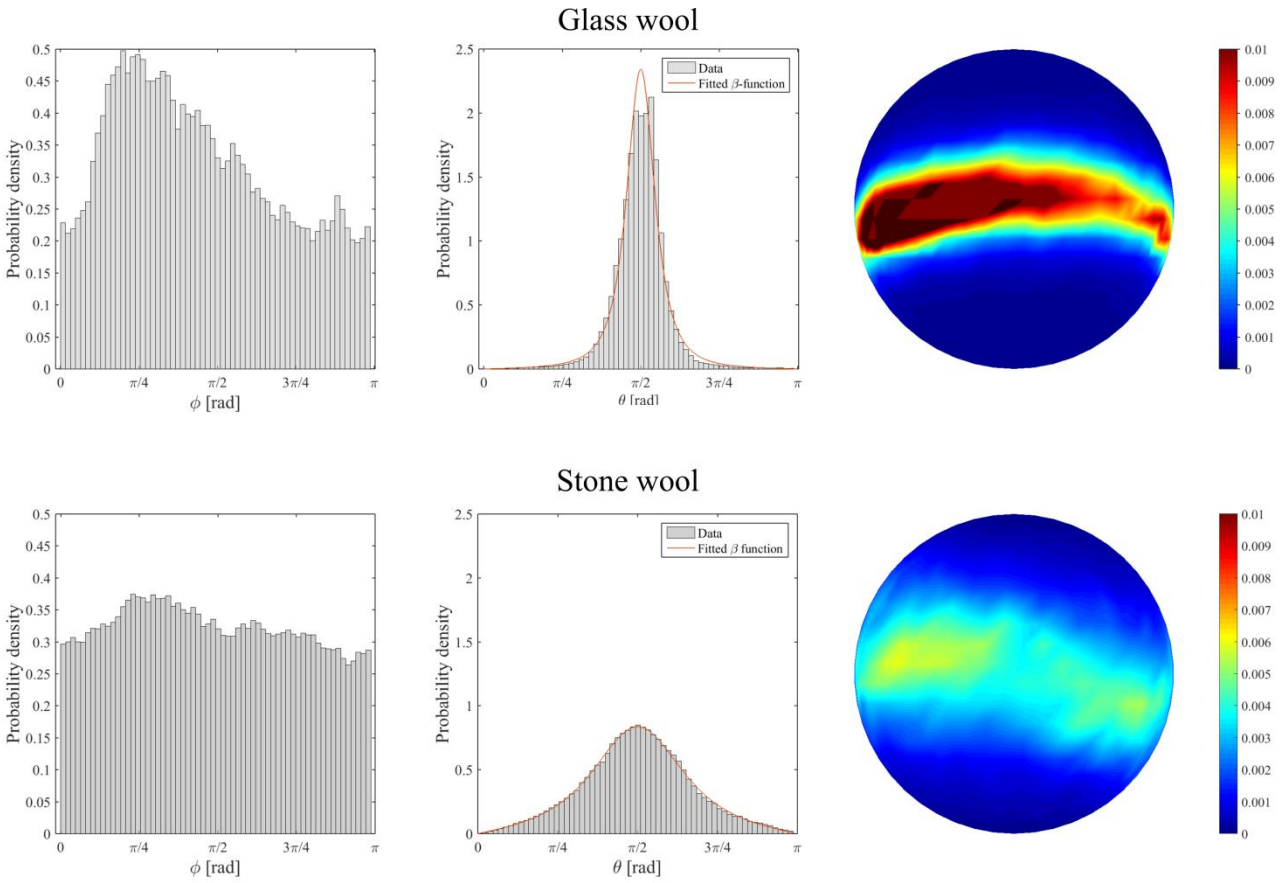

Figure 2.9: Histograms of the angular values of the azimuth (left) and elevation (middle) and joint histogram on a sphere of the azimuth and elevation angles (right) of glass wool (top) and stone wool (bottom).

The distribution of the fibre orientations can be described by the probability density function $p_\beta(\theta, \varphi)$ of elevation angle $\theta \in [0, \pi[$ and azimuth angle $\varphi \in [0, 2\pi[$. The function was first introduced in [45] and used in [40,46,47] for modelling the distribution of orientations of different fibrous materials. β is the anisotropy parameter and a real positive scalar.

$$p_\beta(\theta, \varphi) = \frac{1}{4\pi} \frac{\beta \sin\theta}{(1 + (\beta^2 - 1)\cos\theta)^{3/2}} \tag{2.8}$$

To fit the distribution of the elevation angles, the following marginal density function is considered:

$$p_\beta(\theta) = \frac{1}{2} \frac{\beta \sin\theta}{(1 + (\beta^2 - 1)\cos\theta)^{3/2}} \tag{2.9}$$

The parameter β represents the anisotropy of the fibres. High values leads to fibres parallel to the x-y plane while a value closer to 0 reflects a vertical orientation of the fibre, parallel to the z-axis. The fitted function of Equation (2.9) is included in the histogram of the distribution of the elevation angles of Figure 2.9. The β values are given in Table 2.4.

Table 2.4: Estimated parameter β for the distribution of the elevation angles.

	Glass wool	**Stone wool**
β	4.7	1.7

The respective values of β of the two materials indicate that the preferential horizontal orientation in the x-y plane is stronger for the glass wool fibres than for the stone wool fibres. This is confirmed as well by the width of the peak of the elevation angles distribution centred on $\pi/2$ which is wider for the stone wool distribution than for glass wool distribution. In the x-y plane, a preferential orientation centred about $\pi/4$ is observed on the histogram of the distribution of the azimuth angles for the glass wool specimen in Figure 2.9, top, left. The distribution of the azimuth angles of the stone wool fibres in Figure 2.9 does not suggest that the stone wool fibres possess a preferential orientation in the x-y plane.

The joint histograms on a unit sphere agree well with the interpretation of the histograms of the angle distributions. The orientation of the glass wool fibres is highly concentrated as indicated by the dark red colour of the histogram on the unit sphere in Figure 2.9 while the orientation of the stone wool fibres seem to be more uniformly distributed.

The variations of the β parameter are investigated for increasing volume size and as a function of the distance along the z-axis. The results are presented in Figure 2.10. The orientation of the fibres with respect to the distance along the z-axis does not vary significantly as a function of the volume especially for the stone wool sample as reflected by the small variations of β for increasingly large volumes. A cubic volume of a few micrometres gives a representative image of the real glass wool and stone wool materials in terms of the orientation with respect to the z-axis.

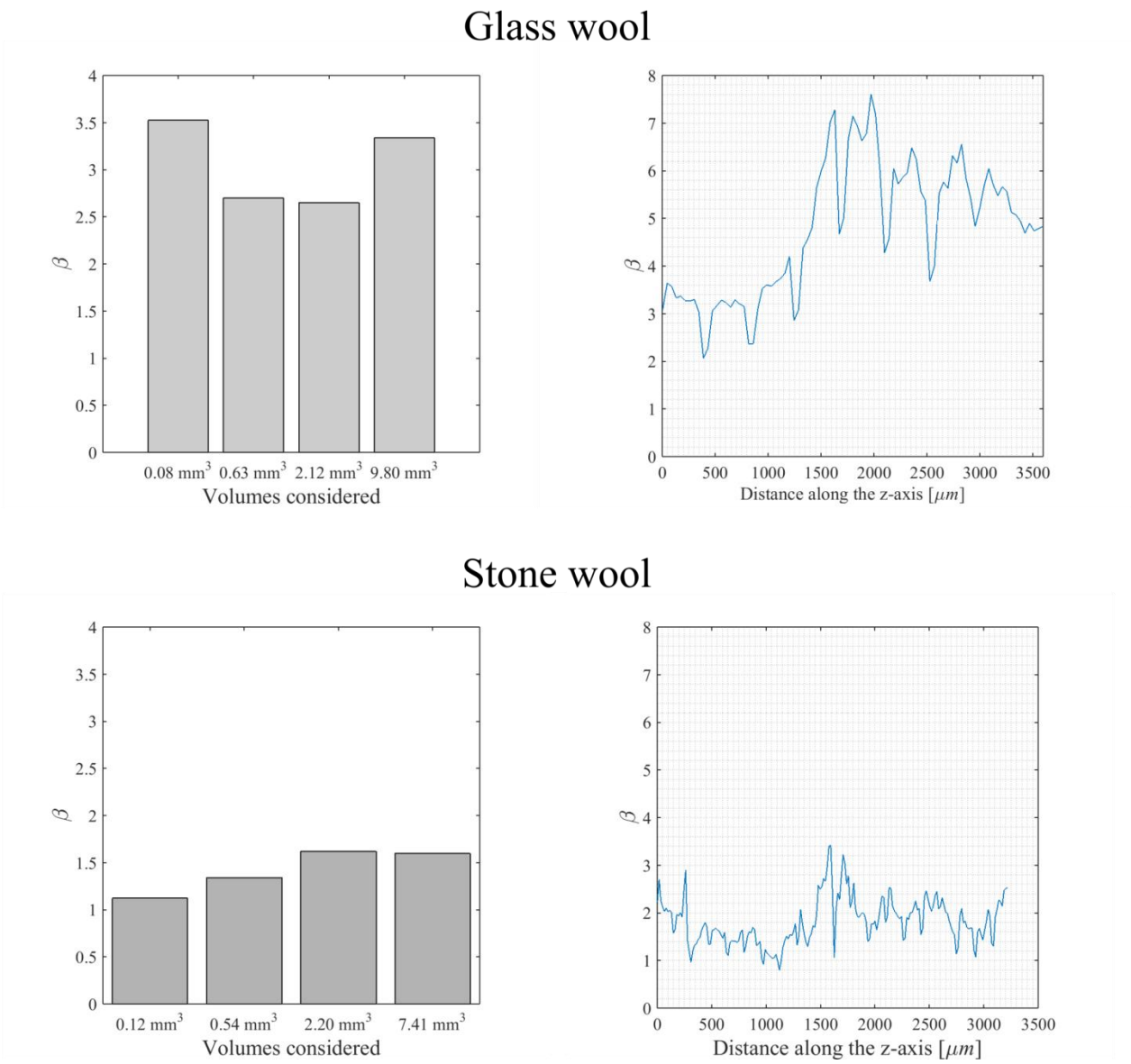

Figure 2.10: Left: Variations of the parameter β over an increasing volume size. Right: Variations of the parameter β as a function of the distance along the z-axis.

The orientation of the glass wool fibres varies significantly throughout the thickness of the sample. The value of β oscillates between high and low values as if the glass wool fibres were organized in a succession of horizontally and vertically oriented fibres layers. The glass wool fibres present significant but regular variations of orientation along the z-axis. The parameter β of the stone wool fibres varies as well but not as drastically as it was observed in the case of the glass wool specimen.

2.7.2 Determination of the fibre diameter distribution of mineral wool

The fibre diameter distribution is estimated using the grayscale granulometry method on the datasets identified as GW-B and SW-B in Table 2.3. The total volume analysed is [2560 x 2560 x 1000] voxels or [832 x 832 x 325] μm^3 for each dataset. A histogram of the distribution of the fibre diameter is given in Figure 2.11, top.

A lognormal distribution has been fitted to the measured data. The probability density function of the lognormal distribution is the following:

$$p_{\mu,\sigma}(x) = \frac{1}{x\sigma\sqrt{2\pi}} \exp \frac{-(lnx - \mu)^2}{2\sigma^2} \tag{2.10}$$

The parameters of the lognormal distribution μ and σ obtained by fitting and the mean m_f and standard deviation s_f of the fibre diameter for both types of material are given in Table 2.5.

Table 2.5: Parameters of the diameter distribution of glass wool and stone wool fibres.

	$\boldsymbol{\mu}$	$\boldsymbol{\sigma}$	$\boldsymbol{m_f}$ **[μm]**	$\boldsymbol{s_f}$ **[μm]**
Glass wool	1.10	1.05	4.43	3.97
Stone wool	1.30	0.83	4.51	4.36

A 3D rendering of a quarter of the dataset (1280x1280x1000) is given in Figure 2.11, bottom. The dark blue colour represents the thinnest fibres while the yellow/green colours indicate the presence of the thickest fibres.

The mean and standard deviation are similar to the values for both samples but the maximal diameter for the glass wool fibres is about 15 μm while the stone wool fibres can be as thick as 25 μm. In reality, a lot of the thick particles measured in the stone wool sample are not fibres but shots (melt inclusions described in Chapter 1). While the glass wool and stone wool fibres have a similar mean fibre diameter and standard deviation, the histograms of their respective diameter distribution is different: the glass wool has two populations of fibres: the first below 1 μm and the second around 10 μm. On the contrary, the stone wool fibre diameters distribution presents the characteristic of the lognormal distribution with one peak and a right skew.

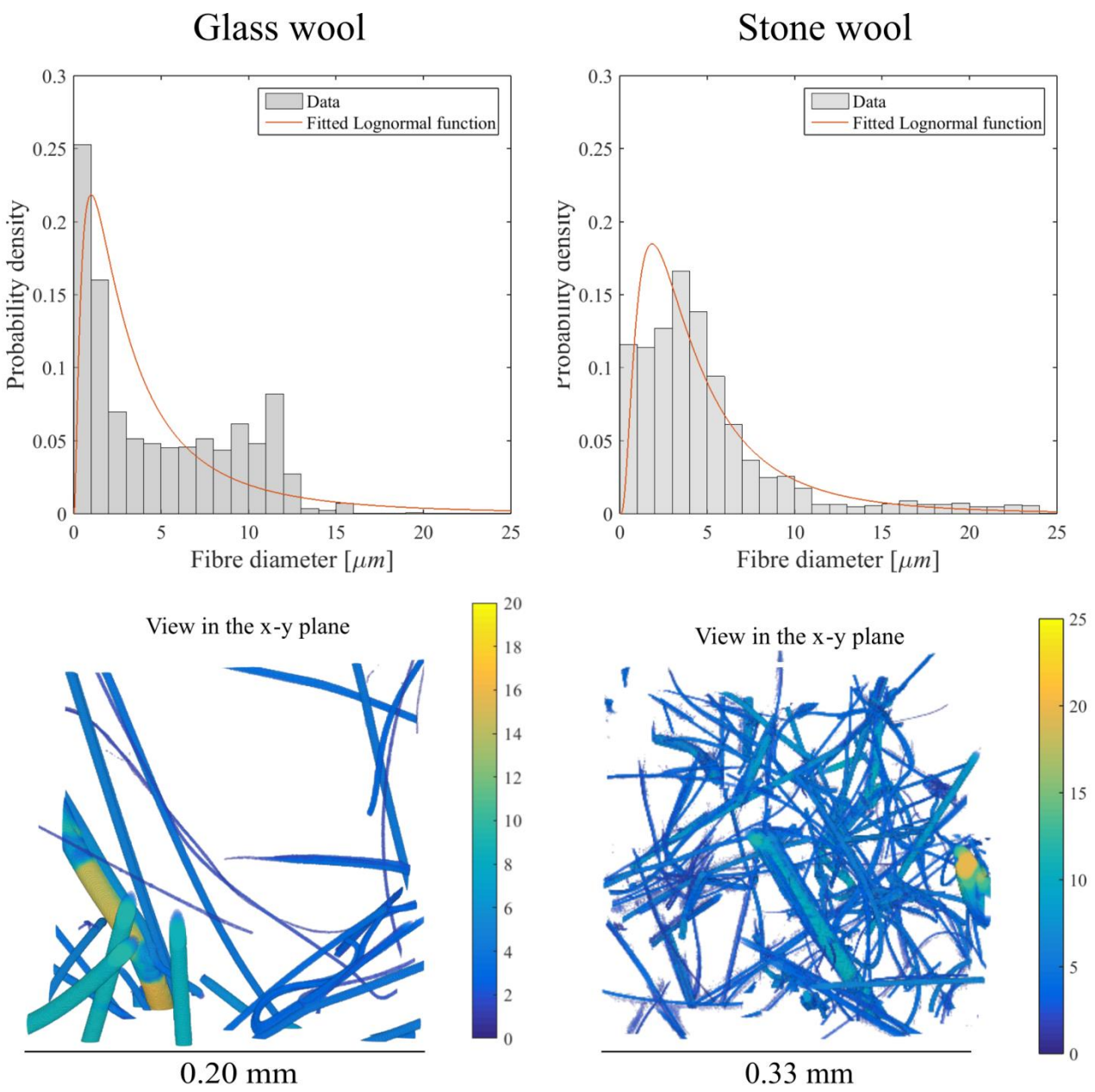

Figure 2.11: Top: Histograms of the fibre diameter distribution. Bottom: 3D rendering of the local variations of the fibre diameter. Left: Glass wool. Right: Stone wool.

Typically, the mineral wool fibre diameter distribution is determined using a SEM and the methodology developed by Koenig et al. [48]. The diameter distribution obtained with this method is length weighted. The mean and the standard deviation of equivalent glass wool and stone wool fibre determined with this method are respectively: 3.49 ± 2.22 and 4.22 ± 2.11 µm. The discrepancy between these and the values obtained with the granulometry method and X-ray CT data can be explained by two factors:

- The size considered in this study is too small to be representative (more than 1000 pieces of fibres are measured in the SEM-based method).
- The data are not comparable as the X-ray CT method returns a volume weighted distribution (each voxel contribute to the estimation of the fibre diameter).

2.7.3 Determination of the pore size distribution

The pore size distribution is evaluated using the plugin developed by Dougherty. The datasets are the same ones that are used in the orientation estimation (GW-A and SW-A from Table 2.3) but cropped to a smaller volume size of [500 x 500 x 1000] voxels or [2.14 x 2.14 x 4.28] mm^3 for the glass wool sample and [500 x 500 x 1000] voxels or [0.82 x 0.82 x 1.64] mm^3 for the stone wool sample because the determination of the pore size is relatively slow for large datasets. The mean pore size m_p and the associated standard deviation s_p for each type of wool are given in Table 2.6.

Table 2.6: Parameters of the pore size distributions inside a glass wool and a stone wool sample.

	m_p [µm]	s_p [µm]
Glass wool	174	77
Stone wool	174	101

The histograms of the distributions of the pore size of the glass wool and stone wool samples are plotted in Figure 2.12 together with the variations of the mean pore size for increasing volumes and for increasing distances along the z-axis. The mean pore size is the same value for glass wool and stone wool but the pore size distribution in glass wool is centred about one peak and presents a narrower distribution than the pore size distribution in stone wool.

Looking at the variations of the mean pore size as a function of the volume, it is noticed that the mean pore size shows less variations for the stone wool material. For both glass wool and stone wool, a volume of a few mm^3 gives a representative estimation of the mean pore size.
The mean pore size in glass wool remains relatively stable for varying distances along the z-axis. This indicates that the glass wool fibres are arranged at regular and uniform intervals. On the other hand, the mean pore size in stone wool varies significantly with respect to the distance along the z-axis. The local minima represents the presence of slices where the fibre volume fraction is locally high and where the fibres are tightly packed. This result agrees with the observations made in

section 2.7.1 where it was suggested that some fibres were arranged in tufts as they shared the same local orientation.

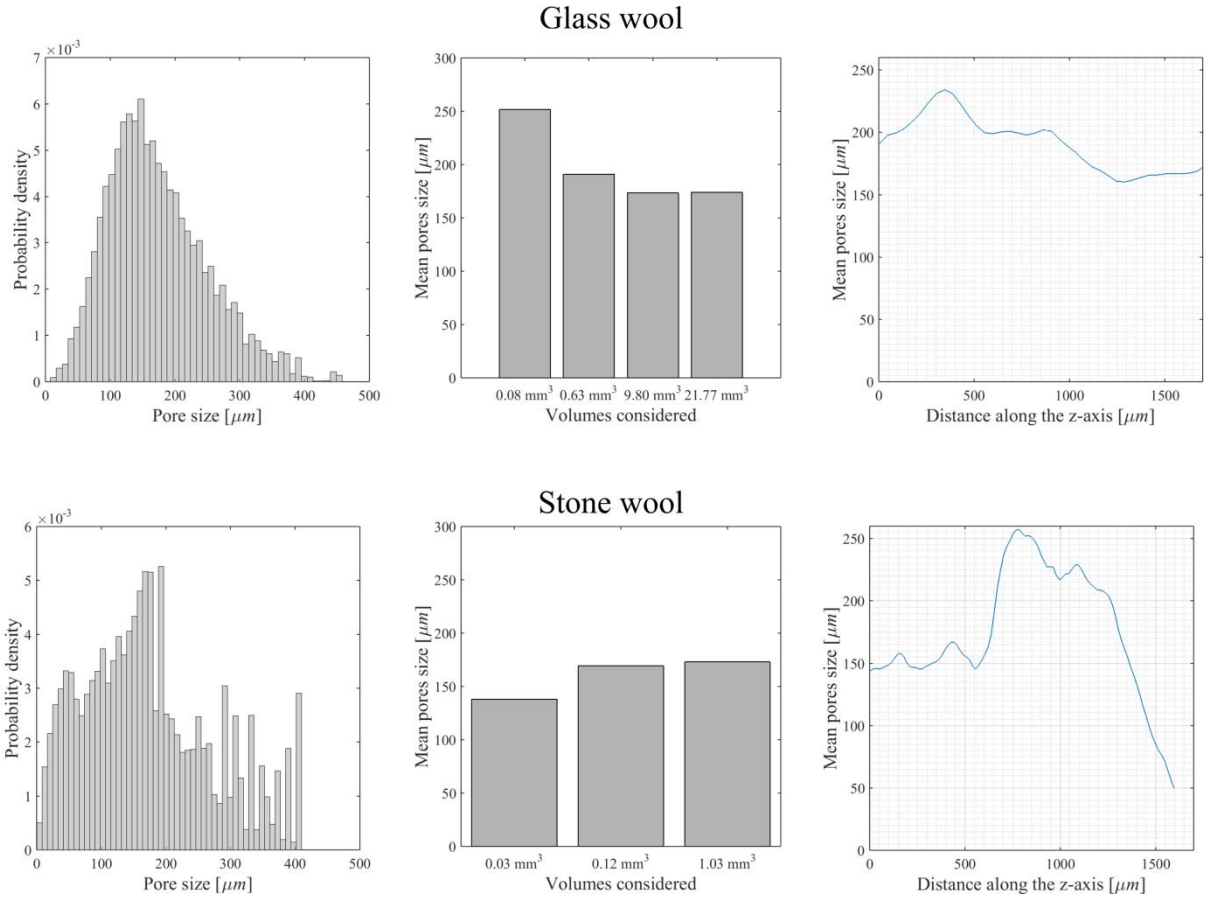

Figure 2.12: Histograms of the pore size distribution (left), variations of the mean pores size for increasing volumes (middle) and increasing distance along the z-axis (right). Top: Glass wool. Bottom: Stone wool.

2.7.4 Determination of the number of contacts

To estimate the number of contacts, the datasets GW-A and SW-A are first converted to binary using a Otsu thresholding method [49] and then transformed into a skeleton using the plugin developed by Beat Müncher for ImageJ. The volume considered for this analysis is limited to [500 x 500 x 500] voxels because the processing of the candidates for the reconnection of skeleton can be slow for large datasets. All the steps detailed in section 2.6 are applied on the skeleton of the glass wool and stone wool datasets. The result of the segmentation is displayed in Figure 2.13 where different colours are attributed to each individual fibre and black dots mark the contacts.

Visually, it is observed that a few of the broken fibres are not recombined or recombined with the wrong fibre. This happens mostly on very curvy fibres. Besides these few errors, the skeleton segmentation seems to perform reasonably well on the dataset. 7035 fibres are counted and 5548 contacts are found in glass wool and 3108 fibres and 1083 contacts are counted in stone wool. This means that the fibres in both samples present on average more than one contact with another fibre. To be able to compare the number of contacts in glass wool and stone wool, the number of contacts is converted into a density of contacts per volume. The value for the density of contacts obtained is 570 mm^{-3} for glass wool and 2020 mm^{-3} for stone wool. As it has been established that the stone wool fibres are ordered in a less layered fashion than the glass wool fibres (cf. 2.7.1) and closely packed in tufts (cf. 2.7.3), a high density of contacts is expected for the stone wool material compared to glass wool.

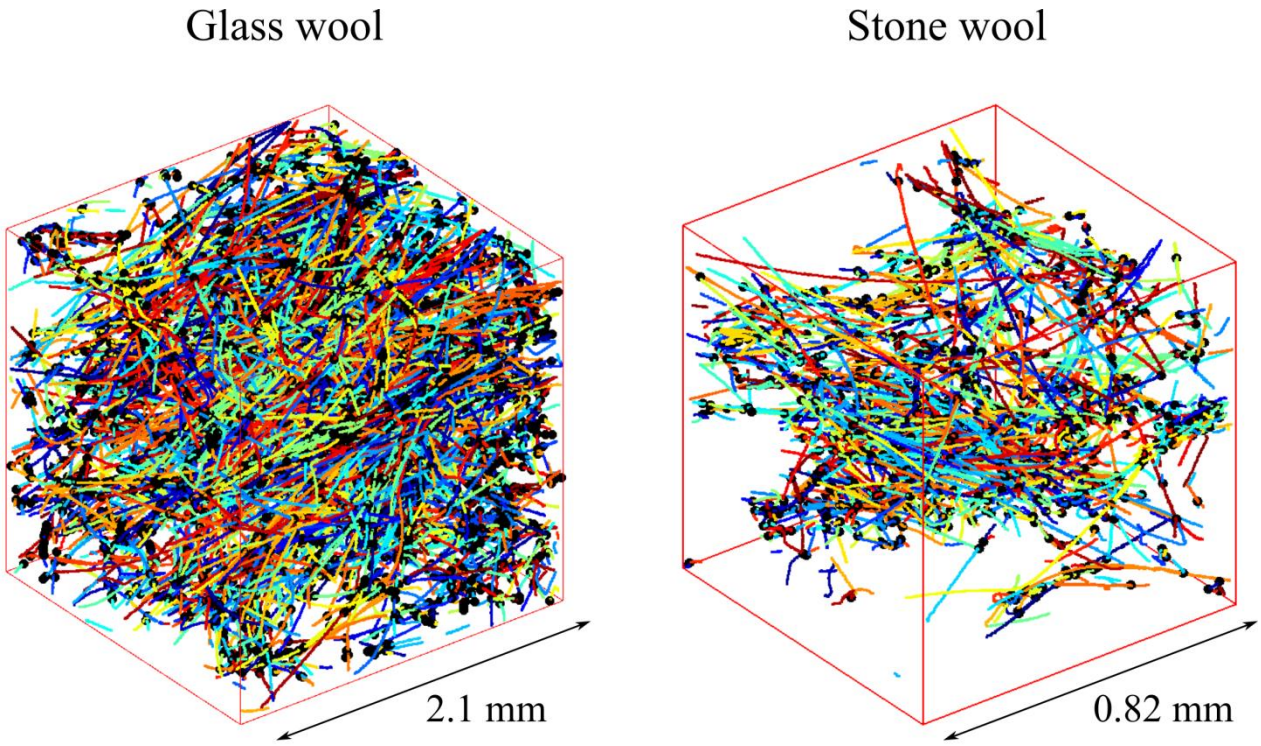

Figure 2.13: Representation of the fibre centrelines where individual fibres are assigned different colours.

2.8 Discussion and summary

It has been demonstrated that SEM is not the suitable tool for the quantification of the fibre structure of mineral wool samples. It is however capable of imaging the binder in the mineral wool and can provide important qualitative information (for example damage of the fibre, binder etc.),

X-ray CT is used to investigate the fibre structure of a glass wool and stone wool sample. Various image analysis tools are employed. Some are developed by the author (Matlab codes for the fibre orientation estimation with the structure tensor and for the diameter estimation via grayscale granulometry) and others are used in the open source software ImageJ (local size for the pores distribution and skeleton for the fibre segmentation). The analysis of the skeleton is implemented in a Matlab code developed by the author.

Data obtained with the laboratory X-ray CT are suitable for the estimation of the fibre orientation distribution and of the pore size distribution.

The smaller voxel size attainable with the synchrotron X-ray CT scanner makes it a more obvious choice than the laboratory scanner for the estimation of the fibre diameter distribution since most of the fibres are only a few micrometres thick.

The estimation of the fibre length distribution is not included in this investigation since the volumes obtained by X-ray CT are not sufficiently large to visualize the fibres in their full length.

The results of the image analysis indicate that both glass wool and stone wool present similarities and differences in their fibre structure. The following main differences are noted:

- The fibres present a more laminar structure in a glass wool sample than in a stone wool sample as reflected by the value β of their respective elevation angle distribution.
- A preferred orientation in the x-y plane exists in a glass wool sample while this was not observed in a stone wool sample which is closer to 2D random.
- The mean fibre diameter in the stone wool sample is similar to the mean fibre diameter of the glass wool sample. However, the presence of shots in the stone wool material affects considerably the distribution. For a fair comparison of the diameter distribution, the shots should be removed from the quantification.
- The fibre diameter distribution of the glass wool materials indicates that both thin and thick fibres are present while the fibre diameter distribution of the stone wool is more homogeneous.
- The pores size distribution presents a narrower peak for the glass wool sample than for the distribution of the stone wool sample. This could indicate that the fibres in a stone wool

material have a short range order (for example assembled in tufts) and a long range order (distance between the bundles/tufts).

- Based on the variations of the fibre orientation and pore size along the thickness and for increasing volumes, it is concluded that the glass wool presents a layered structure where fibres are oriented horizontally and the stone wool fibres are organized in tufts.

- The contact density is higher in the stone wool sample. This can be explained by the fact that stone wool is less laminar and more closely packed than glass wool.
-

The fibre structure of the glass wool and stone wool reflects their production process. Indeed, the preferred orientation in the x-y plane present in glass wool and absent in stone wool can be correlated to the difference in spinning process (the reader can refer to the Chapter 1 where the production processes of glass wool and stone wool are given in details). The cascade spinning and the collection method used in the stone wool production seems to redistribute the fibre in the x-y plane so that a 2D random material is obtained while it is easier with the cup spinning to align the fibres in one direction.

3 Generation of virtual fibre networks

The current chapter deals with the generation of a virtual volume representing accurately the real architecture of the fibre network of mineral wool. The automatic generation of a representative volume is a crucial step in the numerical modelling of mineral wool. The current status of the automatic generation of virtual volumes in the literature is outlined. The approach adopted in this work generates non-overlapping fibre networks where the fibre aspect ratio, orientation and curvature can be controlled. The parameters describing the morphology and arrangement of the fibres are obtained by fitting to statistic distributions the data obtained in Chapter 2. The papers relevant to this chapter are [P2] and partly [P3].

3.1 Existing algorithms for the generation of virtual volumes

The first step in the prediction of the effective properties of a material using numerical homogenization is the automatic generation of the architecture of said material. The methods reported in the literature can be differentiated in two types: the generation can be based on a soft-core process where the modelled inclusions (e.g. fibres) are free to overlap with each other or a hard-core process where the overlap of inclusions is forbidden. From a physical point of view, the overlap of inclusions is not very realistic. However the simplicity of implementation of those soft-core processes has made them a quite popular tool for the microstructure generation of complex materials.

3.1.1 Soft-core methods

One of the first soft-core processes was introduced by Matheron [50] using dilated Poisson lines to create straight infinite cylinders. Later, lines generated by a Poisson process were used to model respectively the microstructure of a fibre non-woven [51], a gas diffusion layer of proton exchange membrane fuel cells [52] and thermal and acoustic fibre materials [47]. In [53], fibres were created by drawing the coordinates of the fibre centrelines. All fibres were assumed to have the same diameter and length. Soft-core models were developed further to consider fibres with a more complex geometry. For example, to model curved fibre systems, several soft-core processes include bending of the fibres through random walks and controlled by a von Mises-Fischer distribution [54,55] or by representing the fibres by B-splines [56,57].

3.1.2 Hard-core methods

The random sequential adsorption (RSA) model is one of the most commonly used methods to construct hard-core systems because its principle is relatively simple even though its implementation can be a bit tedious for inclusions with a complex geometry. The RSA algorithm iteratively generates an inclusion and tries to place it in such a way that it does not intersect another inclusion. Initially created for the packing of spheres, the process was then applied on cylinders by Feder [58]. Recently, Naddeo et al. used an RSA based microstructure generation method with fibres shaped as cylinders but very little details on the overlap detection was provided [59]. A similar approach was adopted in [60] and here the implementation of the contact detection of two cylinders was detailed. For fibres with an isotropic orientation distribution and high aspect ratio, only low volume fractions can be achieved with the RSA algorithm as a jamming limit is reached when no new positions can be found. Modifications of the RSA algorithm can be made so that when a fibre position is rejected because it overlaps another fibre, the fibre is translated to another position [61].

Another type of model based on the deposition of straight fibres can achieve hard-core configurations [62]. This approach gives high fibre volume fraction, but the fibre orientation is limited to the plane. The deposition technique is actually widely used for paper-like materials where the assumption of an in-plane fibre orientation distribution is realistic [63–65]. Bending of the fibre was also included in [66]. When an overlap is detected, fibres are bent to avoid the intersection with other fibres. Straight fibres are modelled as convex prisms with two dodecagon end-faces while several convex irregular polyhedral are used in case of curved fibres. Wang et al. modelled non-woven fibre-webs by a similar deposition algorithm where the orientation was limited to the plane [67].

Recent works on the generation of hard-core volumes are inspired by molecular dynamics simulations. Bezrukov and Stoyan proposed an algorithm for the generation of random packing of ellipsoids of revolution [68]. Contacts between ellipsoids are detected and a force biased algorithm is applied to translate and rotate the particles that overlap. Both approaches achieve a relatively low volume fraction of inclusions (10 – 15 % for isotropic orientation with an inclusion aspect ratio of 10). Ghossein used the principles of molecular dynamics to generate spheres and ellipsoids with a very high aspect ratio (i.e.>10) in a hard-core packing configuration [69]. Altendorf et al.

presented a model combining some of the ideas discussed previously [46]. Firstly, bended fibres are modelled as a chain of spheres by a random walk (also referred as bead-springs model in polymer physics [70]). Secondly, similarly to Wirjadi [54] and Karkkainen et al. [55] the orientation distribution can be controlled in spite of the bending. Thirdly, the use of the force-biased approach on sphere packing [71] and [68] and fourthly, the design of energies in molecular dynamics defines the forces [71]. The outcome is a random hard-core fibre model with a controllable bending and high volume fraction. The level of bending is controlled by two parameters in the multivariate von Mises Fisher distribution. As mentioned earlier, the fibres are represented as a chain of spheres with defined centres and radii. This first step gives a soft-core system of bending fibres. To produce a hard-core configuration, a force biased approach is used. Two kinds of forces are applied to the sphere centres: repulsion and recover forces. The repulsion force prevents the overlap of fibres and the recover force maintains the sphere chain structure. Gaiselmann et al. also represented the fibres by a chain of spheres but where the fibres midpoints are generated with a Poisson point process and the fibres by random 3D polygonal tracks [72]. The system is then transformed into a non-overlapping method using the force-biased algorithm.

The algorithm for the generation of mineral wool fibre structures should fulfil the following requirements:

a) Overlaps between fibres are reduced.
b) High aspect ratio can be achieved.
c) Fibre main orientation, aspect ratio and curvature can be controlled.

The requirement a) eliminates obviously all the soft-core approaches. RSA algorithms are also discarded because they do not satisfy requirement b) since the algorithm jams at high aspect ratio. Deposition techniques and the molecular dynamics approaches of Ghossein et al. are also not considered because the control of the fibre main orientation and curvature is not possible in these techniques (requirement c)).

The most promising algorithm for the generation of mineral wool fibre structure is thus the one proposed by Altendorf and Jeulin.

3.2 Generation algorithm developed by Altendorf and Jeulin

For the generation of a virtual periodic fibre network, the approach from Altendorf and Jeulin presented in details in [46] was implemented in MATLAB [73]. Thereby, a fibre is modelled as a chain of overlapping spheres where the main direction of the chain is controlled by an orientation distribution depending on a parameter β. This orientation distribution was first introduced in [45]. The density associated to this distribution is the function $p_\beta(\theta, \varphi)$ introduced in Chapter 2, section 2.3.3 (Eq. (2.8)). Figure 3.1 shows different realization of an overlapping fibre network with different values of β.

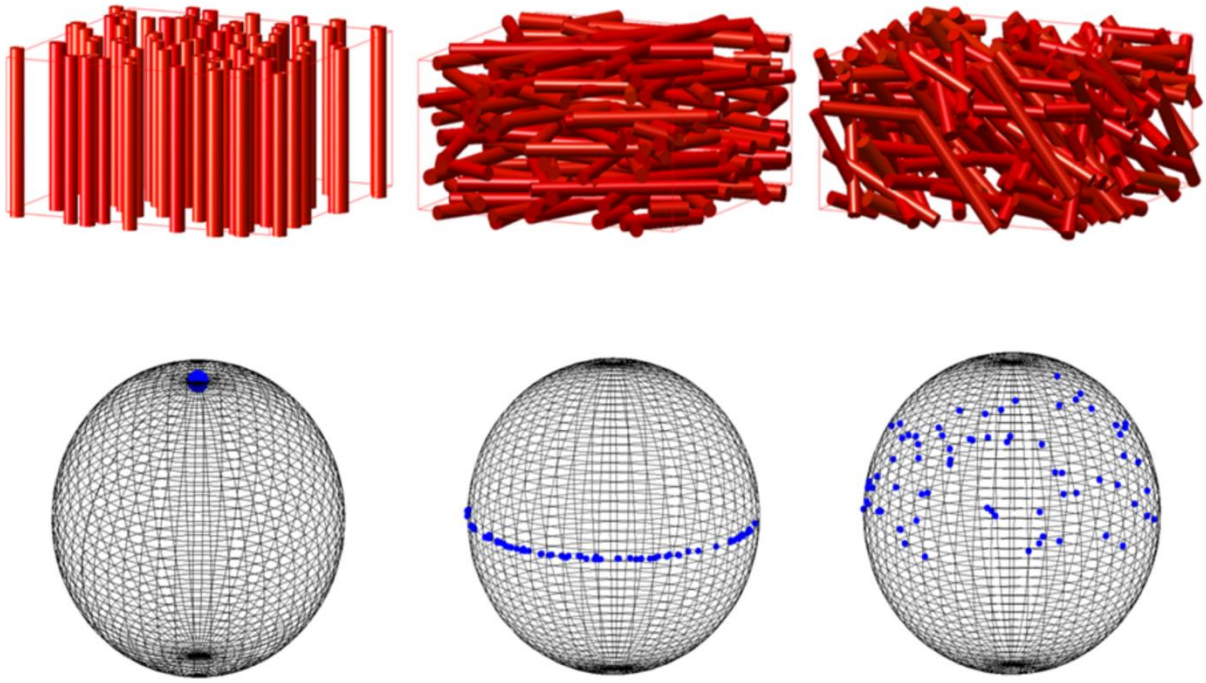

Figure 3.1: Top: Realization with $\beta = 0$ (left), $\beta = 100$ (middle) and $\beta = 1$ (right). Bottom: Corresponding directions on the unit sphere.

The direction of each individual spheres of the chain depends on the main direction and the direction of its previous neighbour in the chain. Practically, this is achieved by using a multivariate von Mises-Fisher distribution with two preferred directions. The probability density element of a multivariate von Mises-Fisher distribution f for a vector $\boldsymbol{u}$ with two preferred direction vectors $\boldsymbol{\mu_1}$ and $\boldsymbol{\mu_2}$ and two concentration parameters κ_1 and κ_2 is given here:

$$f(u|\boldsymbol{\mu_1}, \kappa_1, \boldsymbol{\mu_2}, \kappa_2) = \frac{|\kappa_1\boldsymbol{\mu_1} + \kappa_2\boldsymbol{\mu_2}|}{2\pi(e^{|\kappa_1\boldsymbol{\mu_1}+\kappa_2\boldsymbol{\mu_2}|} - e^{-|\kappa_1\boldsymbol{\mu_1}+\kappa_2\boldsymbol{\mu_2}|})} e^{(\kappa_1\boldsymbol{\mu_1}^T\boldsymbol{u}+\kappa_2\boldsymbol{\mu_2}^T\boldsymbol{u})^T\boldsymbol{u}} \quad (3.1)$$

This approach is particularly attractive for mineral wool fibres which present a certain degree of curvature. However, the implementation for the generation of a virtual volume of mineral wool fibres does not succeed in depicting in a realistic manner the curvature observed in mineral wool fibres. Some modifications were thus brought to the algorithm to best adapt to the case of a mineral wool material and as a result, an alternative fibre model is proposed in this thesis.

3.3 The spherocylinder fibre model

In the present work, a fibre is discretized as a chain of overlapping spherocylinders. A representation of the fibre model is given in Figure 3.2, a). To create a fibre, the position of a point, which corresponds to a centre of a sphere contained in one end of the spherocylinder, is drawn from a uniform distribution over the intervals $[0; L_x]$, $[0; L_y]$ and $[0; L_z]$. From there the position of the second point, which corresponds to a centre of another sphere, contained in the other end of the first spherocylinder, is computed using the orientation unit vector $\boldsymbol{\mu}$. The next spherocylinder overlaps with the spherical part of the previous spherocylinder.

The walk that builds the centreline of the fibre can be expressed as a function of the local unit vector $\boldsymbol{\mu_A}$ which defines a direction of a sphero-cylinder, the height of the cylinder l_{AB} and the position of the point $\boldsymbol{x_B}$ and of its previous neighbour $\boldsymbol{x_A}$:

$$\boldsymbol{x_B} = \boldsymbol{x_A} + \boldsymbol{\mu_{AB}} \cdot l_{AB} \quad (3.2)$$

In Figure 3.2 b-f), several realizations generated using the spherocylinder fibre model and different values for the parameters κ_1 and κ_2 of eq. (3.1) are represented. When κ_1 and κ_2 are equalled to 100, almost straight fibres are obtained (Figure 3.2 f)). A value of 1 for κ_1 and κ_2 gives very wavy and curled up fibres as shown in Figure 3.2 d). Figure 3.2 a) and Figure 3.2 b) indicate that relatively smooth curves are obtained when at least one value of κ_1 or κ_2 is high. To represent the mineral wool fibres which can be described by smooth curves as observed in 2.1 and control accurately the main fibre orientation, a low value of κ_1 and a high value of κ_2 should be selected.

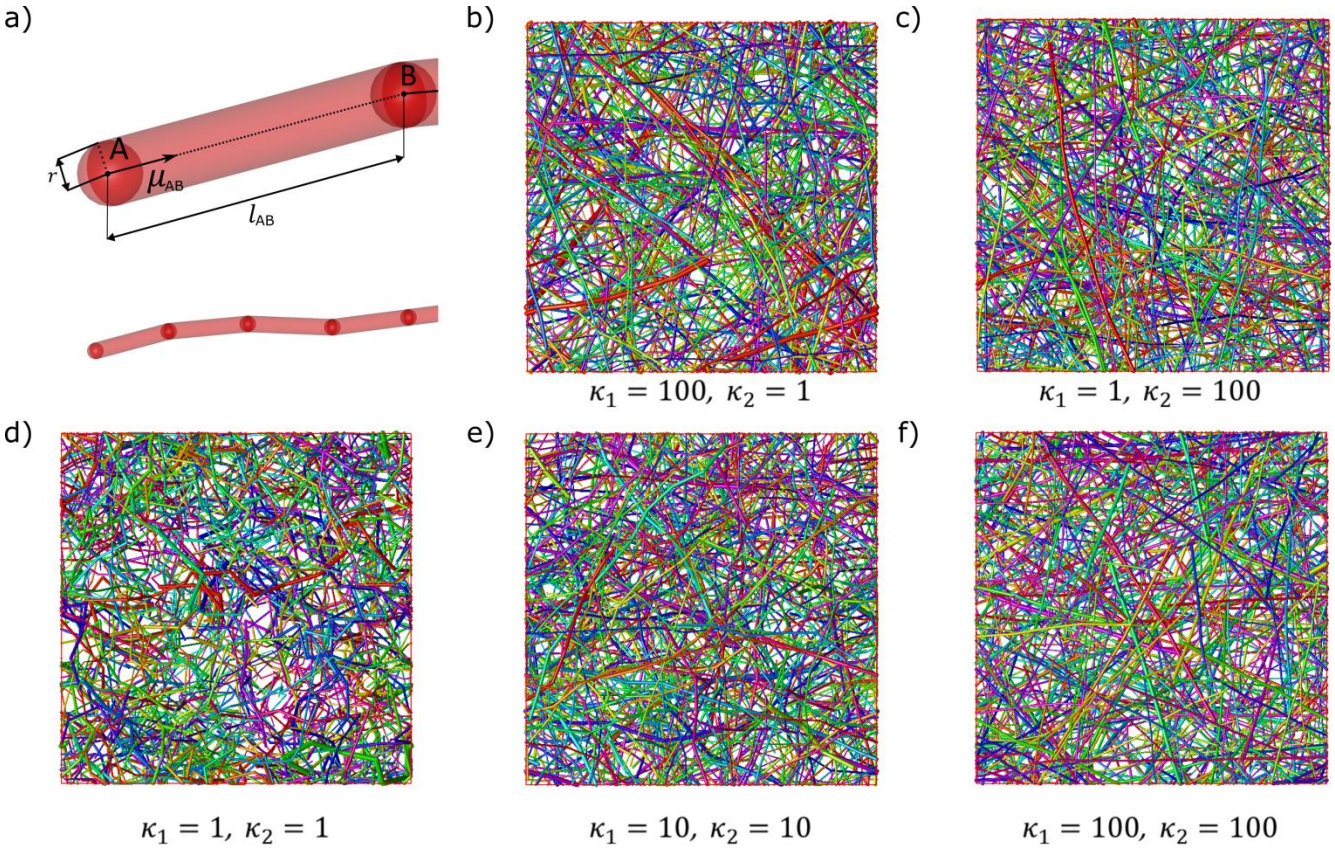

Figure 3.2: a) Spherocylinders chain model. b), c), d), e), f) Generated fibre networks – view xy.

3.4 Reduction of the overlaps in the spherocylinders fibre model

To transform the fibre network into a non-overlapping system, translations are applied as described in [46]. In the present work, the translation required to reduce the overlap is implemented differently than in [46] as the model for a fibre was changed from a chain of overlapping sphere to a chain of overlapping spherocylinders. To determine if two fibres overlap with each other, the minimal distance between the centreline of two neighbouring spherocylinders is determined. If the minimal distance is less than the sum of the radii of the spherocylinders, an overlap is detected. To reduce the overlap, a translation proportional to the overlap is applied to the points of the spherocylinders corresponding to the minimal distance. The main challenge with this implementation is the search of the points leading to the minimal distance between two spherocylinders. The algorithm for finding the minimal distance is derived below:

Let L_1 and L_2 be two lines passing respectively through the pair of points (P_1, P_2) and (Q_1, Q_2). Let $\boldsymbol{u} = P_2 - P_1$ and $\boldsymbol{v} = Q_2 - Q_1$. The equations for the lines can be expressed as a function of the vectors $\boldsymbol{u}$ and $\boldsymbol{v}$, the points P_1 and P_2 and the parameters s and t:

$$\begin{aligned} P(s) &= P_1 + s\boldsymbol{u} \\ Q(t) &= Q_1 + t\boldsymbol{v} \end{aligned} \tag{3.3}$$

The introduced variables are shown in Figure 3.3.

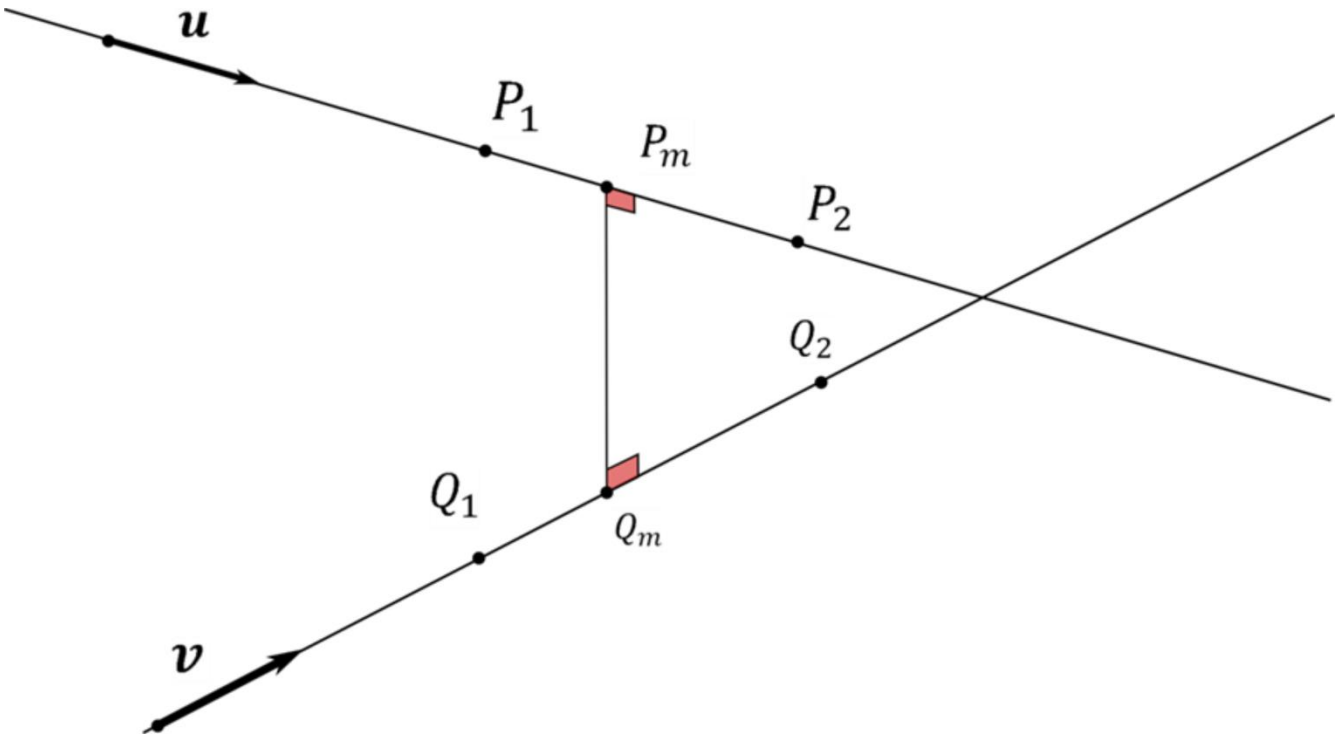

Figure 3.3: Definition of the variables used for the determination of the minimal distance between two segments.

The minimal distance between two lines L_1 and L_2, is defined by two points, P_m and Q_m, belonging respectively to L_1 and L_2.
The segment $[P_m Q_m]$with direction vector $\boldsymbol{w} = Q_m - P_m$ is orthogonal to both lines L_1 and L_2.

This condition can be translated into the system of two equations:

$$\begin{cases} \boldsymbol{u}.\boldsymbol{w} = 0 \\ \boldsymbol{v}.\boldsymbol{w} = 0 \end{cases} \tag{3.4}$$

w can also be expressed as:

$$\boldsymbol{w} = Q_m - P_m = P_0 + s_m\boldsymbol{u} - Q_0 - t_m\boldsymbol{v} = \boldsymbol{w_1} + s_m\boldsymbol{u} - t_m\boldsymbol{v} \tag{3.5}$$

where $\boldsymbol{w_1}$ is defined as**:**

$$\boldsymbol{w_1} = P_1 - Q_1 \tag{3.6}$$

Replacing $\boldsymbol{w}$ by the expression of Eq. (3.5), the system of equations becomes:

$$\begin{cases} s_m(\boldsymbol{u}.\boldsymbol{u}) - t_m(\boldsymbol{u}.\boldsymbol{v}) = -\boldsymbol{u}.\boldsymbol{w_1} \\ s_m(\boldsymbol{v}.\boldsymbol{u}) - t_m(\boldsymbol{v}.\boldsymbol{v}) = -\boldsymbol{v}.\boldsymbol{w_1} \end{cases} \tag{3.7}$$

If $(\boldsymbol{u}.\boldsymbol{u})(\boldsymbol{v}.\boldsymbol{v}) - (\boldsymbol{u}.\boldsymbol{v})(\boldsymbol{u}.\boldsymbol{v}) \neq 0$, the solutions of the systems are:

$$\begin{aligned} s_m &= \frac{(\boldsymbol{u}.\boldsymbol{v})(\boldsymbol{v}.\boldsymbol{w_1}) - (\boldsymbol{v}.\boldsymbol{v})(\boldsymbol{u}.\boldsymbol{w_1})}{(\boldsymbol{u}.\boldsymbol{u})(\boldsymbol{v}.\boldsymbol{v}) - (\boldsymbol{u}.\boldsymbol{v})(\boldsymbol{u}.\boldsymbol{v})} \\ t_m &= \frac{(\boldsymbol{u}.\boldsymbol{u})(\boldsymbol{v}.\boldsymbol{w_1}) - (\boldsymbol{u}.\boldsymbol{v})(\boldsymbol{u}.\boldsymbol{w_1})}{(\boldsymbol{u}.\boldsymbol{u})(\boldsymbol{v}.\boldsymbol{v}) - (\boldsymbol{u}.\boldsymbol{v})(\boldsymbol{u}.\boldsymbol{v})} \end{aligned} \tag{3.8}$$

The minimal distance between the two lines is then:

$$d_m = \left| w_0 + \frac{(\boldsymbol{u}.\boldsymbol{v})(\boldsymbol{v}.\boldsymbol{w_1}) - (\boldsymbol{v}.\boldsymbol{v})(\boldsymbol{u}.\boldsymbol{w_1})}{(\boldsymbol{u}.\boldsymbol{u})(\boldsymbol{v}.\boldsymbol{v}) - (\boldsymbol{u}.\boldsymbol{v})(\boldsymbol{u}.\boldsymbol{v})}\boldsymbol{u} - \frac{(\boldsymbol{u}.\boldsymbol{u})(\boldsymbol{v}.\boldsymbol{w_1}) - (\boldsymbol{u}.\boldsymbol{v})(\boldsymbol{u}.\boldsymbol{w_1})}{(\boldsymbol{u}.\boldsymbol{u})(\boldsymbol{v}.\boldsymbol{v}) - (\boldsymbol{u}.\boldsymbol{v})(\boldsymbol{u}.\boldsymbol{v})}\boldsymbol{v} \right| \tag{3.9}$$

If $(\boldsymbol{u}.\boldsymbol{u})(\boldsymbol{v}.\boldsymbol{v}) - (\boldsymbol{u}.\boldsymbol{v})(\boldsymbol{u}.\boldsymbol{v}) = 0$, the lines are parallel and the distance separating the lines is constant. The distance can be evaluated by setting one of the parameters and solving for the other.
The shortest distance between two segments is defined by R_m and S_m. The points R_m and S_m are equivalent respectively to P_m and Q_m except when one of the following conditions is fulfilled:

- If $s_m < 0$, the poinP_mt lies outside of the segment: the point S_m corresponding to the shortest distance between the two segments is P_1.
- If $s_m > 1$, the point P_m lies outside of the segment: the point S_m corresponding to the shortest distance between the two segments is P_2.
- If $t_m < 0$, the point Q_m lies outside of the segment: the point S_m corresponding to the shortest distance between the two segments is Q_1.

- If $t_m > 1$, the point Q_m lies outside of the segment: the point S_m corresponding to the shortest distance between the two segments is Q_2.

The spherocylinders are also given an axial and rotational stiffness. Therefore when they move to suppress the overlaps, they are subjected together with their close neighbours to translations and rotations as defined in [46] to limit the bending and the stretching of a spherocylinder with respect to the other spherocylinders of a fibre. To reduce the speed of the search of overlapping spherocylinders, the candidates for the search are built using a near-neighbour list.

3.5 Summary

An algorithm for the generation of a non-overlapping complex fibre network has been developed. The generation process can be adapted to create fibre structures with a random main fibre orientation, a random fibre bending and different aspect ratios with different size of the simulated network. Periodicity of the generated volumes can be enforced which becomes relevant when solving for the volume effective properties using homogenization. The volumes generated with the presented algorithm can be fitted to the real characteristics of the mineral wool material under investigation and used in a numerical homogenization solver (for example, FEM) to derive its representative volume element and effective properties. This will be the topic of the next chapter.

4 Prediction of the elastic properties of mineral wool using the Finite-Element Method

The next step after the characterization of the fibre structure of a mineral wool product (Chapter 2) and the generation of a virtual fibre network (Chapter 3) is the computation of the mechanical properties. This chapter focuses on the prediction of the elastic stiffness of the random fibre network using the Finite-Element Method (FEM). The geometries imported in the FEM software, Abaqus [74] have been generated using the algorithm presented in the previous chapter. The evaluation of the effective properties of a material requires that a generated volume is a representative volume element (RVE). The RVE is defined as the volume large enough to represent the geometry of the sample and small enough to limit the computational costs. The size of the RVE for a mineral wool material will be examined here for two types of boundary conditions. A study of the effect of the fibre structure parameters (orientation and curvature) and binder stiffness is included and highlights their contribution to the elastic properties. The findings regarding the determination of the RVE and the boundary conditions are also presented in the paper [P3]in appendix.

4.1 Literature on the modelling of fibre material properties using FEM

FEM is a powerful tool to gain insight in the mechanical properties of complex fibrous materials. It has been intensively used for the determination of the elastic properties of fibre composites using 2D planar models and 1D beam elements in [75,76] or 3D models with fibres modelled with beam elements [77] or solid elements [59,66,78].

In the field of random fibre network where the matrix phase is air and where the fibres are either bonded (e.g. mineral wool), sintered (e.g. metallic fibre network) or simply entangled (e.g. cotton), numerous works dealt with the simulation of the elastic properties. For example, 2D models including material damage and failure behaviour have been developed to study the mechanical properties of bonded nonwoven materials [79–83].

Recently, Berhan et al. explored the role of nanorope waviness on the effect moduli of nanotube sheets [84] in a 2D model. Their results suggest that reducing waviness would improve Young´s

moduli in these materials. Few other models in the literature have focussed on the shape of the fibre: most approaches represent a fibre as a straight line. In some cases, a 3D model is needed since the mechanics of random fibre networks cannot be described accurately by planar models. For example, 3D models of random fibrous networks gave insights on the mechanics of sintered metallic fibre networks [85], the negative Poisson´s ratio of compressed fused network [53] and on the tensile behaviour of bonded inorganic fibres [86].

In this work, beam elements are adopted as it was reported in many of the aforementioned studies that beam elements describe accurately the mechanical behaviour of fibre materials [75,79,82,85,86].

4.2 Numerical homogenization method

Numerical homogenization can be used to relate overall properties to those of local constituents. It can lead to an accurate estimation of a specific material property if the volume considered is an RVE. Following the terminology of Huet [87], the estimated properties are defined as *effective properties* when the volume qualifies as an RVE. If the volume is smaller than the RVE, the properties are instead referred as *apparent properties*. When the volume is large enough, Sab [88] proved that the apparent properties become equivalent to the effective properties under any set of boundary conditions. The convergence towards the effective properties can however vary depending on the types of boundary conditions. In this section, several boundary conditions for the simulation of the effective properties of mineral wool are reviewed. The implementation of the numerical homogenization into the finite-element software Abaqus is outlined as well.

4.2.1 Boundary conditions

In this work, three types of boundary conditions are considered: kinematic uniform boundary conditions (KUBC), periodic boundary conditions (PBC), periodic uniform mixed boundary conditions (PUMBC).

4.2.1.1 Kinematic uniform boundary conditions (KUBC)

Kinematic uniform boundary conditions (KUBC) also referred to in the literature as uniform displacement conditions are given by:

$$\boldsymbol{u}(\boldsymbol{x}) = \boldsymbol{\varepsilon}\boldsymbol{x} \qquad \forall \boldsymbol{x} \in V \tag{4.1}$$

where $\boldsymbol{u}(\boldsymbol{x})$ is the vector displacement, $\boldsymbol{\varepsilon}$ is the applied strain and V designates the faces of the simulation cell.

They are however known to overestimate the effective properties of the volume element [87]. Because of this, KUBC is often considered as an upper bound. An illustration of the boundary conditions used for the application of a uniaxial strain in the direction of the x-axis is given in Figure 4.1, right.

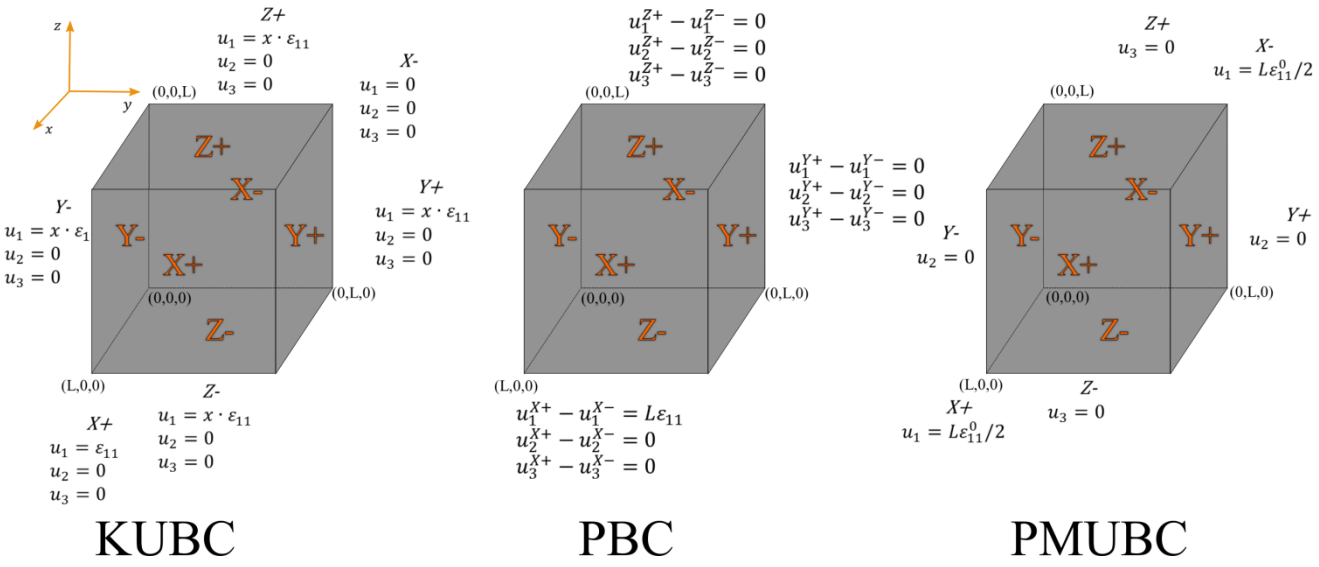

Figure 4.1: Boundary conditions for the case of an uniaxial normal strain in the direction of the x-axis.

4.2.1.2 Periodic boundary conditions (PBC)

Kanit et al. [89] established that the mean apparent properties obtained with periodic boundary conditions converge faster towards the effective properties than the KUBC. In the PBC the volume is considered as a periodic array of a repeated unit cell. In a periodic array, the displacements must be continuous since adjacent cells cannot be separated nor be intruded into each other after deformations.

Similarly, in a periodic array, the traction distribution at the opposite parallel boundaries must be the same. Thus to enforce the PBC, the following conditions on the displacements must be applied:

$$\boldsymbol{u_i^{k+} - u_i^{k-}} = \varepsilon_{ij}^0 \left(\boldsymbol{x_j^{k+} - x_j^{k-}} \right) \tag{4.2}$$

where $\boldsymbol{u_i^{k+}}$ and $\boldsymbol{u_i^{k-}}$ are the displacements on two opposite boundary surfaces$(i = 1,2,3)$, ε_{ij}^0 is a component of the applied strain field ε^0 and $\boldsymbol{x_j^{k+}}$ and $\boldsymbol{x_j^{k-}}$ are the coordinates of two points on opposite boundary surfaces. Figure 4.1 (middle) shows the application of PBC in the case of a uniaxial tensile strain in the x-axis direction.

4.2.1.3 Periodic mixed uniform boundary conditions (PMUBC)

The PMUBC developed by Pahr et al. [90] combine strain and stress constraints. Pahr et al. reported that the PMUBC gave equivalent results to the PBC while requiring less computational cost. Table 4.1 details the sets of boundary conditions for a normal and shear strain case. u_i and t_i for $i = 1,2,3$ are respectively the displacements and tractions on the boundary. The other loading cases are defined in a similar fashion. The definitions of the faces are given in Figure 4.1, left where the PMUBC are represented for the application of a uniaxial strain in the direction of the x-axis.

Table 4.1: PMUBC for a normal case and a shear case.

Load case	**Z-**	**Z+**	**X-**	**X+**	**Y-**	**Y+**
x-tension	$t_1 = 0$ $t_2 = 0$ $u_3 = 0$	$t_1 = 0$ $t_2 = 0$ $u_3 = 0$	$u_1 = -L\varepsilon_{11}^0/2$ $t_2 = 0$ $t_3 = 0$	$u_1 = L\varepsilon_{11}^0/2$ $t_2 = 0$ $t_3 = 0$	$t_1 = 0$ $u_2 = 0$ $t_3 = 0$	$t_1 = 0$ $u_2 = 0$ $t_3 = 0$
xy-shear	$t_1 = 0$ $t_2 = 0$ $u_3 = 0$	$t_1 = 0$ $t_2 = 0$ $u_3 = 0$	$t_1 = 0$ $u_2 = -L\varepsilon_{12}^0/2$ $t_3 = 0$	$t_1 = 0$ $u_2 = L\varepsilon_{12}^0/2$ $t_3 = 0$	$u_1 = -L\varepsilon_{12}^0/2$ $t_2 = 0$ $t_3 = 0$	$u_1 = L\varepsilon_{12}^0/2$ $t_2 = 0$ $t_3 = 0$

4.2.2 Determination of the components of the stiffness tensor

The stiffness tensor $\boldsymbol{C}$ of a volume element is computed through:

$$\boldsymbol{\Sigma = CE} \tag{4.3}$$

where $\boldsymbol{\Sigma}$ and $\boldsymbol{E}$ are the macroscopic stress and strain tensors. $\boldsymbol{C}$ can also be expressed as:

$$\boldsymbol{C} = \begin{pmatrix} C_{11} & C_{21} & C_{31} & C_{41} & C_{51} & C_{61} \\ C_{12} & C_{22} & C_{32} & C_{42} & C_{52} & C_{62} \\ C_{13} & C_{23} & C_{33} & C_{43} & C_{53} & C_{63} \\ C_{14} & C_{24} & C_{34} & C_{44} & C_{54} & C_{64} \\ C_{15} & C_{25} & C_{35} & C_{45} & C_{55} & C_{65} \\ C_{16} & C_{26} & C_{36} & C_{46} & C_{56} & C_{66} \end{pmatrix} \tag{4.4}$$

In order to obtain all the components of the apparent elasticity tensor C, each generated fibre network is solved using 6 deformation states:

$$\boldsymbol{E}^1 = \begin{bmatrix} \varepsilon_{11}^0 \\ 0 \\ 0 \\ 0 \\ 0 \\ 0 \end{bmatrix} \quad \boldsymbol{E}^2 = \begin{bmatrix} 0 \\ \varepsilon_{22}^0 \\ 0 \\ 0 \\ 0 \\ 0 \end{bmatrix} \quad \boldsymbol{E}^3 = \begin{bmatrix} 0 \\ 0 \\ \varepsilon_{33}^0 \\ 0 \\ 0 \\ 0 \end{bmatrix} \quad \boldsymbol{E}^4 = \begin{bmatrix} 0 \\ 0 \\ 0 \\ \varepsilon_{13}^0 \\ 0 \\ 0 \end{bmatrix} \quad \boldsymbol{E}^5 = \begin{bmatrix} 0 \\ 0 \\ 0 \\ 0 \\ \varepsilon_{23}^0 \\ 0 \end{bmatrix} \quad \boldsymbol{E}^6 = \begin{bmatrix} 0 \\ 0 \\ 0 \\ 0 \\ 0 \\ \varepsilon_{12}^0 \end{bmatrix} \tag{4.5}$$

Each deformation state gives a column of the apparent elastic tensor. To obtain the average of the stress over the volume considered, the reaction forces at the reference points where the displacement is imposed are extracted and the stresses are derived by dividing the resulting reaction force by the area of the face of the volume at the boundary considered.

Symmetrical constraints of the material can reduce the variety of the components. For example, a system with a 3D random fibre orientation is considered as isotropic and the resulting elasticity tensor is invariant to rotations of the coordinate system. The tensor simplifies then to two independent constants C_{11} and C_{44} and can be described by three engineering constants: the Young´s modulus E, the shear modulus G and the Poisson´s ratio υ.

A material will be transverse isotropic if its properties remain unchanged with respect to rotations around the z-axis. A material with a fibre distribution that can be described by a β function as introduced in Eq. (2.8) will be transverse isotropic. The elastic tensor of a transverse isotropic material simplifies to 5 independent values:

$$\boldsymbol{C} = \begin{pmatrix} C_{11} & C_{12} & C_{13} & 0 & 0 & 0 \\ C_{12} & C_{11} & C_{13} & 0 & 0 & 0 \\ C_{13} & C_{13} & C_{33} & 0 & 0 & 0 \\ 0 & 0 & 0 & C_{44} & 0 & 0 \\ 0 & 0 & 0 & 0 & C_{44} & 0 \\ 0 & 0 & 0 & 0 & 0 & C_{11} - C_{12} \end{pmatrix} \tag{4.6}$$

4.2.3 Implementation

4.2.3.1 Parameters for the generation of the fibre network

The parameters presented in Table 4.2 are used for the generation of fibre networks representative of a light density stone wool product. The inputs β and V_F are selected based on the findings of Chapter 2. It was not possible to include the fibre length determination in the analysis of the X-ray data. For this study, it is decided that the fibre length will be kept constant and 250 times higher than the mean fibre diameter. Similarly, the curvature parameters introduced in section 3.2, Eq. (3.1), are determined based on the visual comparison of the generated and real volumes as the fibre segmentation method has not been validated yet.

Table 4.2: Parameters used in the generation of virtual fibre networks.

Fibre Young´s modulus [MPa]	**Spring stiffness [N/mm]**	**Fibre volume fraction (V_F)**	**Fibre aspect ratio**	**Main fibre orientation (β)**	**Fibre curvature**	
					κ_1	κ_2
90000	1	1 %	250	1.7	100	1

A comparison of the fibre structure as observed in the SEM, in a 3D rendering from the X-ray CT and generated according to the algorithm of Chapter 3 is shown in Figure 4.2.

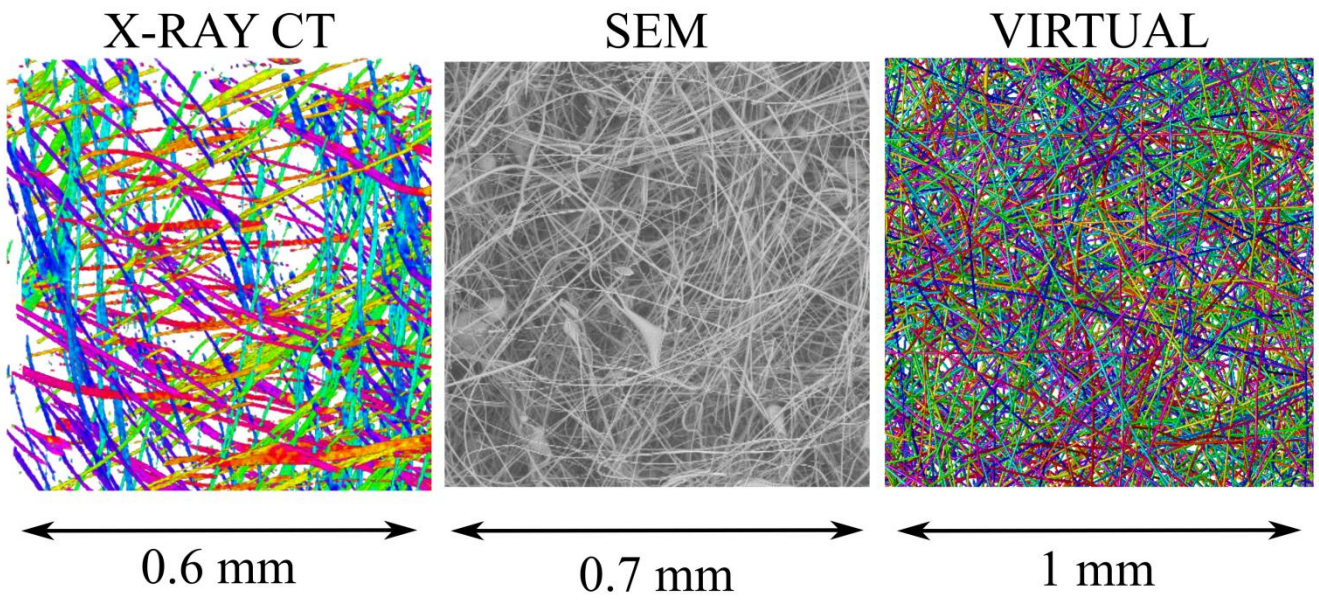

Figure 4.2: Mineral wool fibre network: 3D rendering from X-ray CT (left), micrograph from SEM (middle) and generated fibre network (right).

4.2.3.2 Analysis type

A quasi-static analysis is run using an explicit procedure. In the explicit dynamics procedure, out-of-balance forces are propagated as stress waves between neighbouring elements. The time increment Δt of the simulation is a function of the smallest characteristic element length L_e and the dilatational wave speed c_d:

$$\Delta t = \frac{L_e}{c_d} \tag{4.7}$$

For a linear elastic material, the dilatational wave speed is given by:

$$c_d = \sqrt{\frac{E}{\rho}} \tag{4.8}$$

Where E is the material Young's modulus and ρ is the material density.

By increasing the material density and the element size, the time increment can be reduced and an economical solution of the quasi-static simulation can be obtained. The energy balance between the kinetic energy and the strain energy is computed in order to evaluate if the solution represents a quasi-static response.

4.2.3.3 Boundary conditions

The periodic constraints on nodal displacements at the boundaries are implemented by defining equation constraints and using dummy nodes. The dummy nodes are introduced through reference points which are not directly linked to the model. A displacement $\boldsymbol{u_i^{dummy}}$ is imposed to the dummy node to represent the quantity $\varepsilon_{ij}^0\left(\boldsymbol{x_j^{k+}} - \boldsymbol{x_j^{k-}}\right)$ from Eq. (4.2) results in:

$$\boldsymbol{u_i^{k+}} - \boldsymbol{u_i^{k-}} = \boldsymbol{u_i^{dummy}} \tag{4.9}$$

A Python script is written to pair the nodes of a face with their periodic nodes on the opposite face and impose periodic displacement using the equation option in Abaqus and dummy nodes.
PMUBC and KUBC are simpler to implement: the displacements of the nodes at the different boundaries of the cell are linked respectively to six different dummy nodes $\boldsymbol{u'^{dummy}_i}$ (one for each face) via equation constraints. The external strain ε_{ij}^0 is applied through the six dummy nodes:

$$\begin{aligned} \boldsymbol{u_i^{k+}} &= \boldsymbol{u'^{dummy}_i} \\ \boldsymbol{u_i^{k-}} &= \boldsymbol{u'^{dummy}_i} \end{aligned} \tag{4.10}$$

4.2.3.4 Bonds between the fibres

In the real material, mineral wool fibres are held together by an organic binder. In the finite-element simulation, spring elements characterized by an axial and rotational stiffness are used to represent the bonds between the fibres. The connectors can have an axial stiffness value as well as rotational stiffness values. The connectors can also be defined as a rigid body. In the latter case, it does not deform. The creation of a bond between two fibres depends on the distance between these two fibres. When the distance between two fibre surfaces is below an adjustable threshold (in this study 0.05 mm), a bond is created. The bonds can be seen as red segments in Figure 4.3.

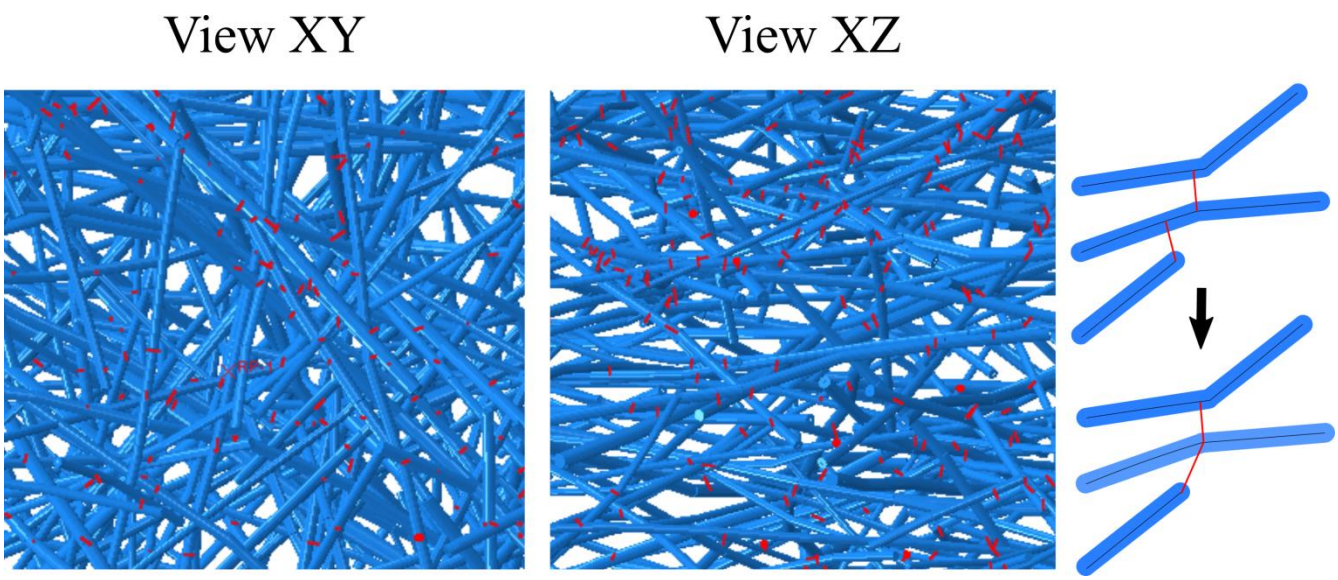

Figure 4.3: 3D view of a fibre network where the red segments represent the connector element between the beam elements.

Because of the high value of β chosen for this network, the fibres are mostly oriented in the x-y plane and most of the connectors are oriented in the vertical direction. To avoid small elements that would slow down the analysis considerably, the nodes created by the connectors along the fibre axis are merged to any other nodes within a distance of 0.02 mm (Figure 4.3 right). In the mineral wool material, fibres in close contacts may or may not be bonded by the binder. By creating a bond based on the distance threshold only, the elastic stiffness of the bonded fibre network might be overestimated.

4.3 Meshing study

In this section, the effect of the element size on the results of the modelling is addressed. The fibres are modelled as 1D beam elements. Timoshenko beam elements were selected to represent each spherocylinder element of a fibre, considering thus that the cross-section may not necessarily remain normal to the beam axis (by opposition to Euler-Bernoulli beam element). By taking the shear flexibility of the elements of the fibre into account, it is expected that the mechanical response of the fibre network can be accurately represented. Different mesh densities are considered. Two types of elements were tested: quadratic and linear Timoshenko beam elements and as no noticeable difference was observed for the C_{11} modulus between the two types of element, the less computational expensive linear elements were chosen for the rest of the analysis. The seed size in Abaqus was varied over a range from 0.02 to 0.1 (approximately 50 to 10 elements per fibre) in

order to study the effect of the element size on the C_{11} modulus. The maximal size of 0.1 was selected since it corresponds to the length of each element used for the discretization of a fibre during the network generation phase.

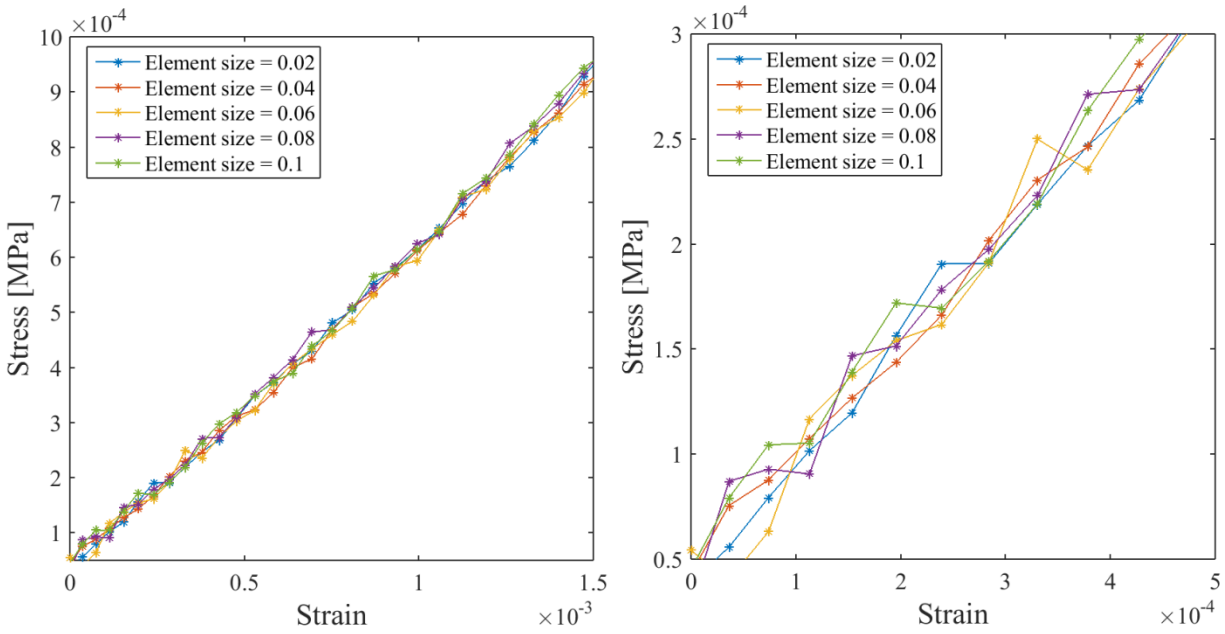

Figure 4.4: Variation of the stresses with the strain for models with different element sizes. The plot on the right is a zoomed inset of the plot of the left.

Figure 4.4 displays the variations of the strain with the stress for different element sizes. It can be observed that the element size has little effect on the stiffness component C_{11} as the slopes remain the same. This is in agreement with [86] where convergence of the mesh sensitivity was observed when at least 3 elements were used per beam. For the rest of the study, the maximal value for the element size, 0.1 is selected in order to obtain a reasonable value for the time increment (and decrease the computational time).

4.4 Determination of size of the RVE

To determine the size of the RVE, one should examine the convergence of the effective properties with respect to the size of the simulation cell and to the type of boundary conditions can influence the rate of convergence.

4.4.1 Convergence towards effective properties as a function of the volume size and type of boundary conditions

KUBC, PMUBC and PBC are studied over an increasing size of volume elements. The ratio of the cell size length over the fibre length is used as an indicator of the volume considered. This ratio varies from 1 to 2 with an increment of 0.2. For each type of boundary conditions, volume sizes and loading cases, 5 cubic volumes generated are solved.

Initial results of the simulations using KUBC indicate that the component C_{11} of the stiffness tensor is significantly overestimated under these conditions. Average values of 25 MPa and 12 MPa are found for C_{11} with volumes with a respective aspect ratio of 1 and 2. A slow convergence towards the effective value of the component C_{11} is also observed. Experimental results have shown that typical values of the elastic modulus of a mineral wool sample are a few hundred kPa for a sample with a fibre volume fraction, orientation and diameter similar to the inputs considered in this study [91]. Based on this initial finding, it is decided to focus the rest of the study solely on the difference between the PMUBC and PBC whose results were found to be in the expected ranges of values for the effective component C_{11}. The values of the different components of models where PMUBC and PBC have been applied are plotted as a function of δ in Figure 4.5.

When the simulation volume is small compared to the length of the fibre (i.e. $\delta < 1.4$), the apparent values of the stiffness components are overestimated. The overestimation of the stiffness components values is greater for PMUBC than PBC for small volumes. As the size of the volume increases, the influence of the boundary type diminishes and the two boundary conditions converges from above towards the same effective values for the components C_{11}, C_{22} and C_{33}, (respectively 242 MPa, 254 MPa and 20 MPa).

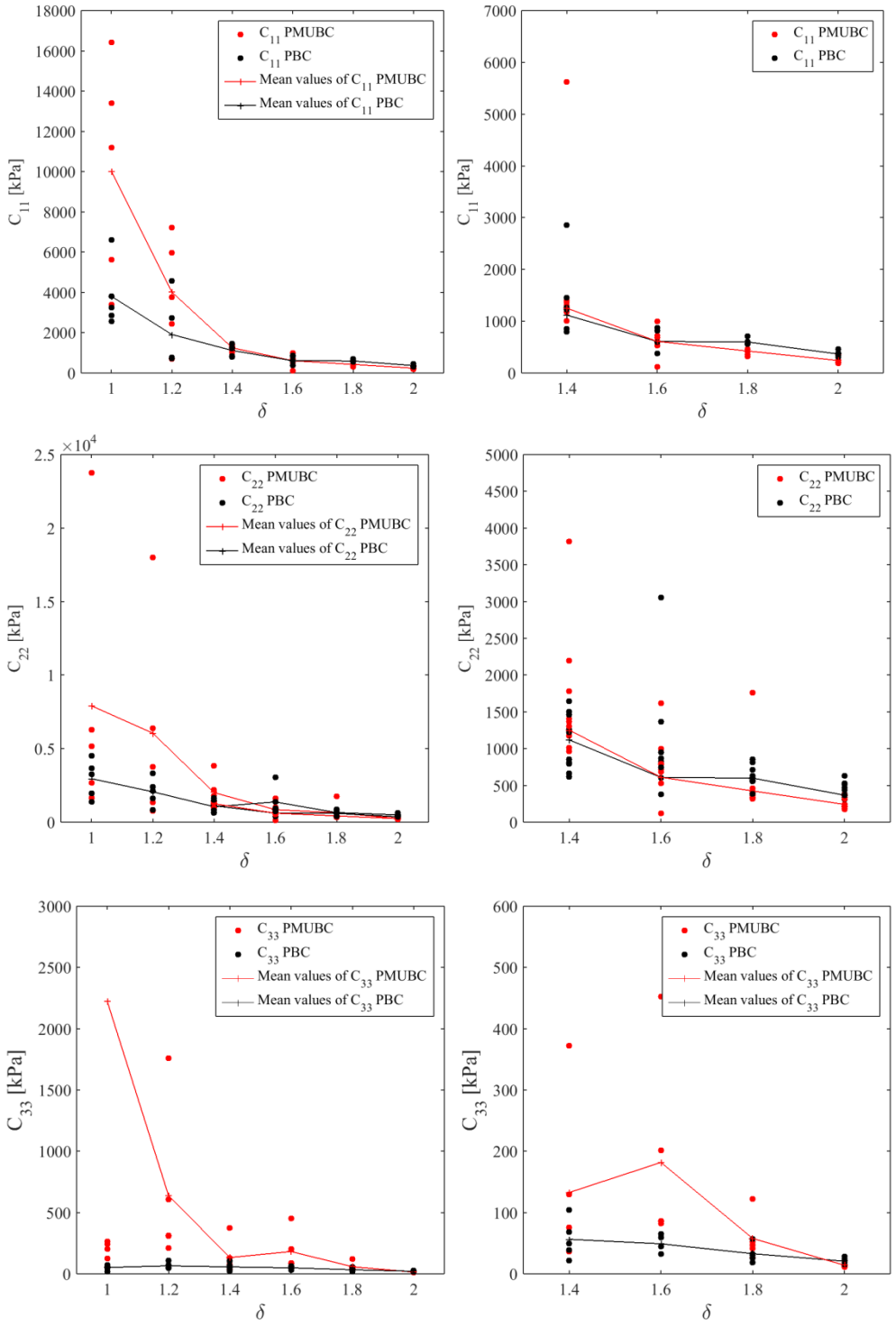

Figure 4.5: Convergence of C_{11} (top), C_{22} (middle) and C_{33} (bottom) as a function of δ, the ratio of the cell size over the fibre length.

Even though the convergence towards the effective properties of the PMUBC is slower than the convergence of the PBC, the PMUBC will be adopted for the rest of the study as they are faster to

implement. The results of this section indicate that the boundary conditions do not affect the values of the stiffness tensor for large volumes.

4.4.2 Convergence of the mean and standard deviation with the number of realizations

Because of the stochastic nature of the generated fibre networks, the values of the stiffness components vary from one realization to another. In this section, the variability of the stiffness components as a function of the number of realizations is studied by computing the standard deviation D_Z and the relative error ε_{rel} of the different values obtained for the component C_{11}. The relative error ε_{rel} for the component C_{11} is defined as follows [89]:

$$\varepsilon_{rel} = \frac{2D_Z}{C_{11}\sqrt{n}} \tag{4.11}$$

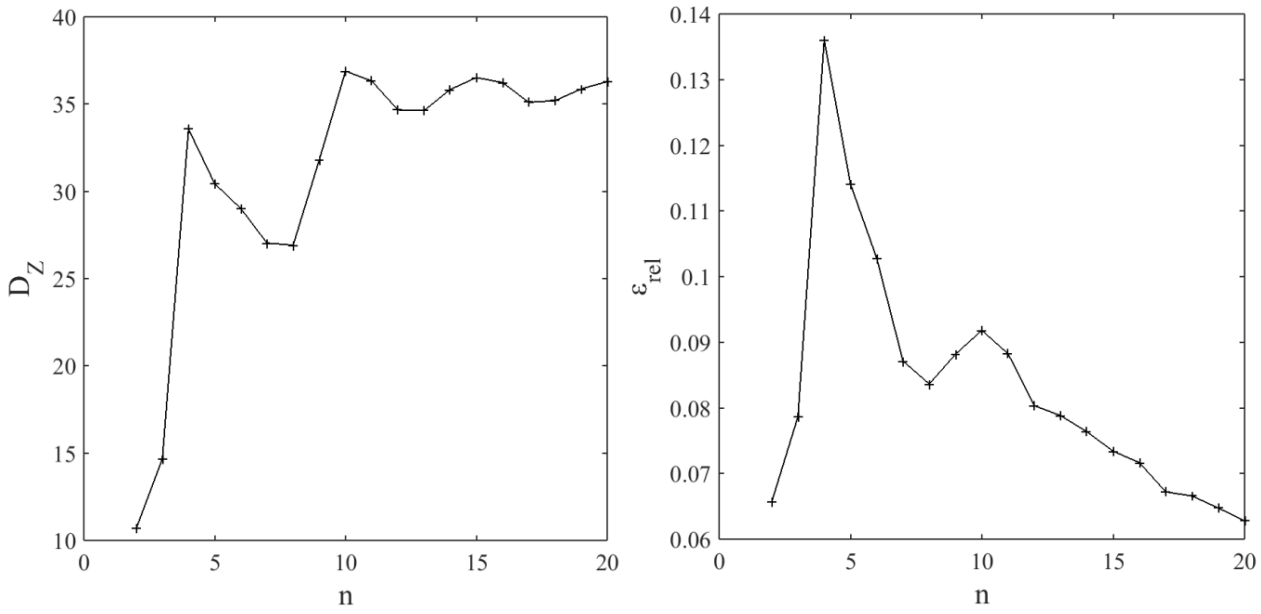

Figure 4.6: Convergence of the standard deviation (left) and the relative error (right) of C_{11} as a function of the number of realizations.

All simulations are performed on a cubic volume element with a side length twice as long as the fibre length ($\delta = 2.0$). The results are presented in Figure 4.6.

The standard deviation varies drastically from 2 to 10 realizations due to the variability of the material but start converging towards 36 kPa after 10 realizations. After 10 realizations, the relative error is below 10% and after 20, below 7.5%. Using the value of the standard deviation at convergence and Eq. (4.11), it is estimated that approximately 35 realizations are required to obtain a relative error less than 5 %.

4.4.3 Deviation from transverse isotropy

The orientation of the fibres drawn from the probability density function of Equation (2.4) should create symmetry around the z-axis. It is therefore expected that the generated mineral wool network is transverse isotropic. In the transverse isotropic case, the following relationships between the components are obtained:

$$\begin{aligned} C_{11} &= C_{22} \\ C_{13} &= C_{23} \\ C_{44} &= C_{55} \\ C_{66} &= \frac{C_{11} - C_{12}}{2} \end{aligned} \tag{4.12}$$

The aforementioned components are computed for 5 simulations with PMUBC for the 6 different sizes as shown in Figure 4.7. It is observed that C_{11} and C_{22} starts converging towards the same value when δ reaches 1.6. The C_{13} and C_{23} components exhibit a similar behaviour. C_{44} and C_{55} are also almost equal to each other. The components of the transverse isotropic stiffness tensor are computed by calculating the mean and standard deviation for the 5 volumes where δ is equal to 2:

$$\boldsymbol{C} = \begin{pmatrix} 241.5 \pm 66.9 & 16.4 \pm 9.36 & 1.6 \pm 1.9 & 0 & 0 & 0 \\ 20.0 \pm 20.9 & 254.6 \pm 86.5 & 1.7 \pm 1.0 & 0 & 0 & 0 \\ 2.1 \pm 0.7 & 2.2 \pm 1.1 & 13.9 \pm 3.0 & 0 & 0 & 0 \\ 0 & 0 & 0 & 50.5 \pm 4.9 & 0 & 0 \\ 0 & 0 & 0 & 0 & 51.1 \pm 6.8 & 0 \\ 0 & 0 & 0 & 0 & 0 & 74.3 \pm 4.7 \end{pmatrix} \text{kPa} \tag{4.13}$$

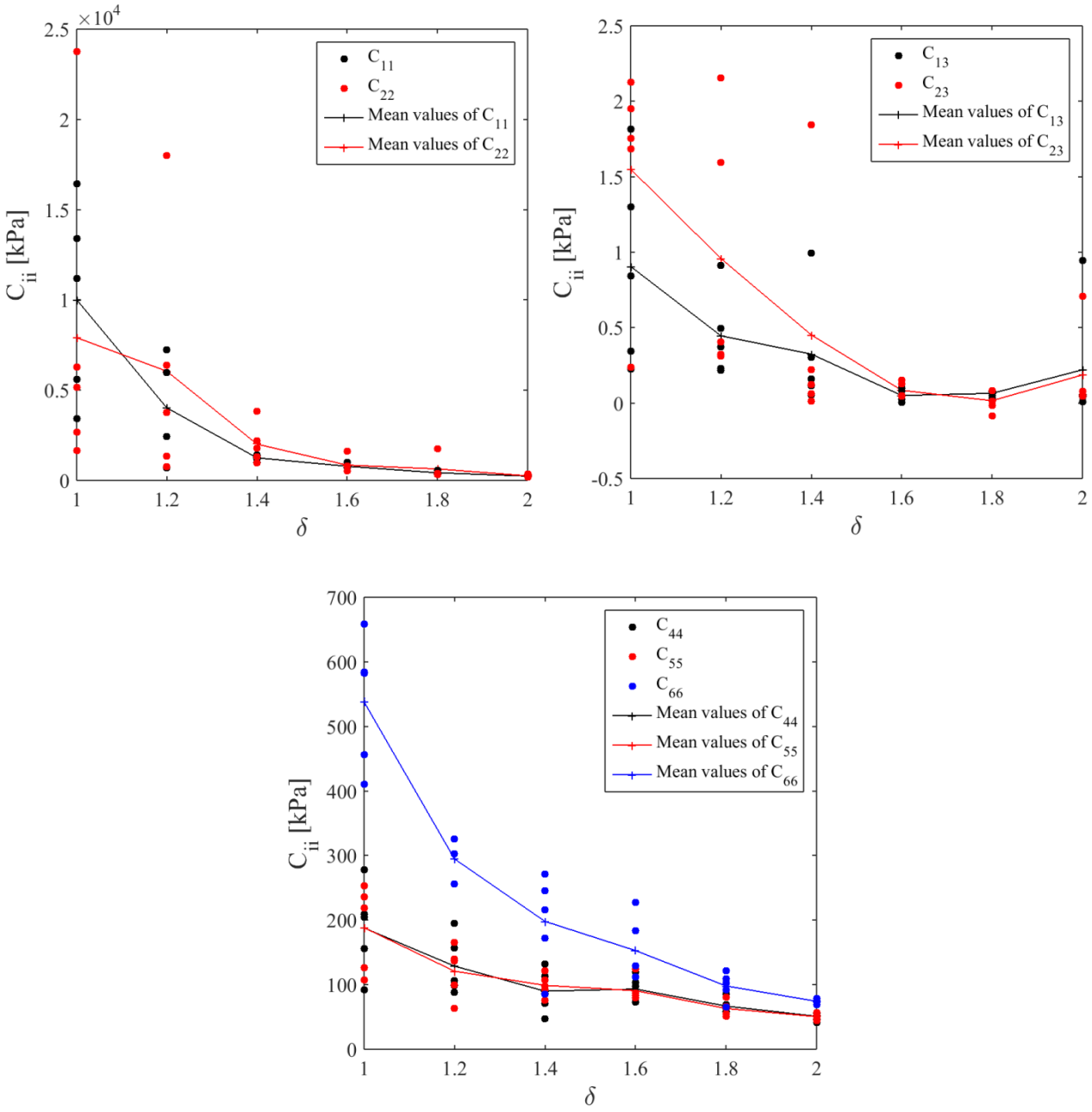

Figure 4.7: Convergence of different components of the stiffness as a function of δ, the ratio of the cell size over the fibre length for PMUBC.

There exist only a few papers dealing with the characterization of the stiffness component of mineral wool and most of them deal with glass wool materials. Tarnow [92] reported values of 390 kPa and 16 kPa respectively for the C_{11} and C_{33} components for a glass wool sample with a fibre volume fraction of 2%. Witz et al. obtained a similar value for the same components C_{11} = 353 kPa and a lower value for $C_{33} = 1.53$ kPa [93]. The discrepancy between the values of C_{11} reported in

the literature and the one computed in this work could be explained by the fact that the fibre networks generated in our study have a less lamellar structure than the glass wool fibre network. Indeed, the parameters were obtained from the characterization of a stone wool sample where the orientation of the fibres is not as lamellar as the orientation of the glass wool fibres.

4.5 Effect of the fibre structure and bond stiffness on the elastic properties

To investigate the effect of the fibre main orientation, curvature and bond stiffness, 5 volumes with a volume size parameter $\delta = 1.6$ are generated since the findings of section 4.4 indicate that the volumes with a size parameter δ of 1.6 converged towards the effective properties. Using volumes with a size parameter δ of 2.0 would lead to a more accurate estimation of the elastic properties for the same number of realizations but it would also double the computation time compared to volumes with a size parameter δ of 1.6.

4.5.1 Main fibre orientation

The main fibre orientation parameter β is varied over the range $[0;\ 20]$ in order to represent the different cases: uniaxial, 2D random and 3D random fibre orientation. The other parameters are kept constant. Six realizations with a volume of aspect ratio 1.6 are simulated. The components C_{11}, C_{22} and C_{33} of the stiffness tensor are calculated for several realizations over the range $\beta \in [0;\ 20]$. The results of the simulations can be visualized in Figure 4.8, left where the values of the components are given with respect to the value of β. In Figure 4.8, UniD, 3DR and 2DR stand respectively for unidirectional, 3D random and 2D random. Lines are drawn between the points to highlight the trends of the curves. The fibre network with the smallest β exhibits the expected behaviour of a unidirectional fibre network: the component of the modulus C_{33} is very high while the two other components C_{11} and C_{22} are close to zero. The 3D random fibre network ($\beta = 1$) behaves like an isostropic material $C_{11} \approx C_{22} \approx C_{33}$ for which the properties remain the same along all directions. Finally, the simulated fibre networks with a 2D random fibre orientation adopt a transverse isotropic behaviour as soon as the β reaches 5 ($C_{11} \approx C_{22} \gg C_{33}$). This study demonstrates that the orientation of the fibre in a sample has a significant importance in the stiffness of a fibre network.

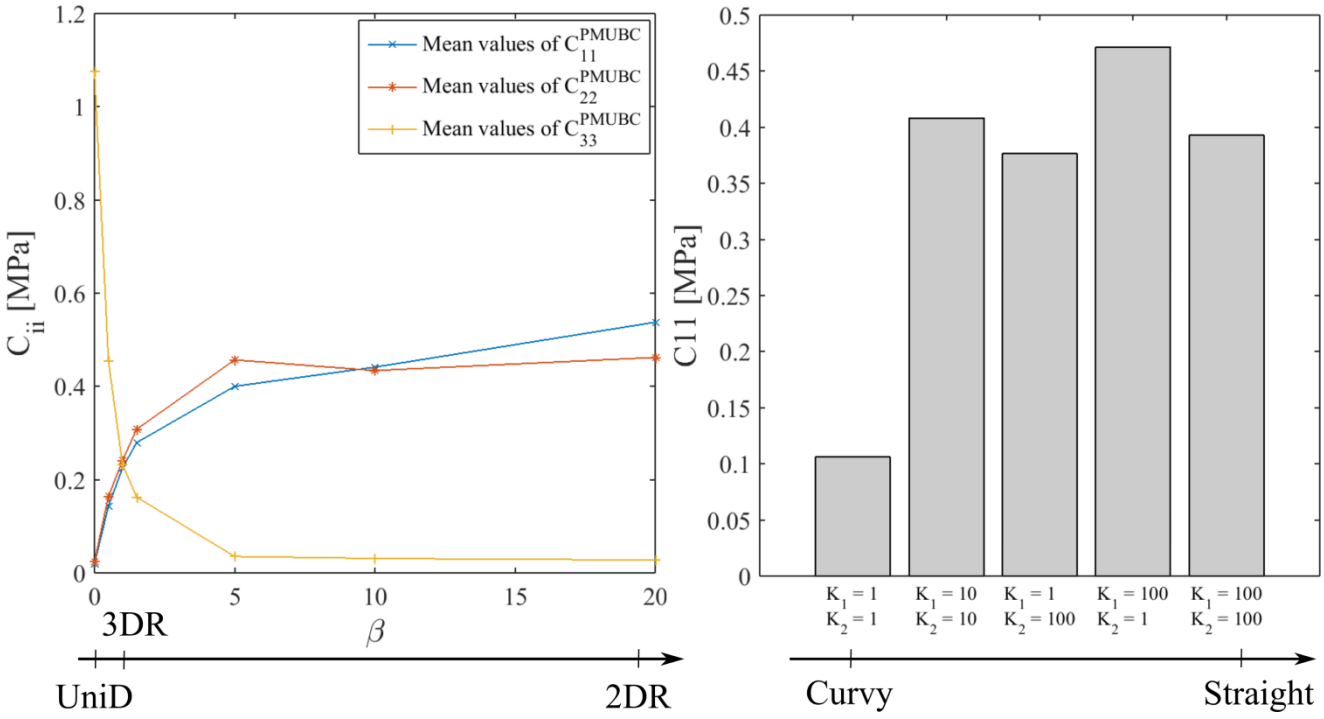

Figure 4.8: Left: Variations of the diagonal stiffness components as a function of the parameter β. Right: Variations of the stiffness component C_{11} as a function of the curvature of the fibres.

4.5.2 Fibre curvature

The curvature of the fibre can be controlled by the parameters κ_1 and κ_2 of the multivariate von Mises-Fischer function from Eq. (3.1) described in Chapter 3. The values chosen for this study ranges from 0 to 100 so that the generated fibre networks present different degree of curvature. Fibre networks generated with the same κ_1 and κ_2 are represented in Chapter 3, in Figure 3.2, b-f). Six realizations with a volume of aspect ratio 1.6 are simulated. The results are given in Figure 4.8, right.

High values of κ_1 and κ_2 mean that the local orientation of the fibre does not deviate significantly from the main fibre orientation and that the fibre does not present a sudden change of orientation. The case where both κ_1 and κ_2 are equaled to 100 corresponds a system with straight fibres while when κ_1 and κ_2 tends to small values, the fibres are curled up on themselves and extremely curvy. The first parameter κ_1 determines how much the fibre deviates from the main fibre orientation locally while κ_2 determines the local deviation of fibre segment with respect to its neighbours.

The general conclusion of the study is that a generated fibre network where the fibres bend significantly (low κ_1 and κ_2) will present a softer response than a generated network with straight fibres (high κ_1 and κ_2). When comparing the influence of κ_1 and κ_2, the study demonstrates that a high value of the parameter κ_1 and a low value of the parameter κ_2 yield a higher stiffness than the stiffness obtained in the opposite situation. This means that the critical parameter in terms of fibre curvature is the deviation from the main fibre orientation.

4.5.3 Binder stiffness

The axial and rotational stiffness of the connector elements are set to the following values: $[10^0, 10^1, 10^2, 10^3, 10^4]$ MPa. The convergence of the C_{11}component of the stiffness tensor of the fibre network with respect to the connector stiffness s is studied. The case of rigid connector is examined as well. The obtained values for the C_{11} component of the stiffness tensor are plotted in Figure 4.9. The solid line represents the curve obtained by fitting the data.

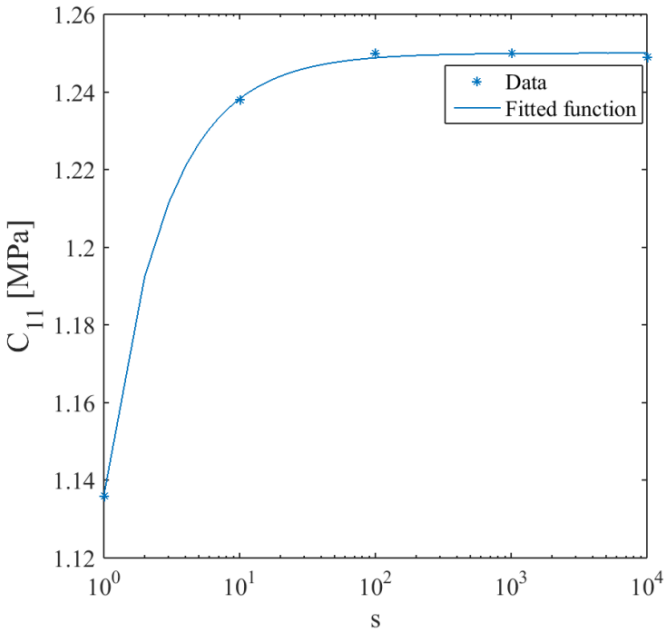

Figure 4.9: Variations of the component C_{11} of the stiffness tensor as a function of the connector stiffness.

Convergence of the C_{11} component of the fibre network is observed at a connector stiffness s of a value of 10 MPa). The value of the C_{11}component at convergence is the same as the one obtained with rigid connectors (~1.25 MPa). These findings imply that the influence of the stiffness of the connector (or in the case of the real material, the binder) on the fibre network stiffness becomes negligible when the stiffness of the connector is superior to 10 MPa.

4.6 Summary

In this chapter, fibre networks representative of mineral wool products are imported into an FEM model and solved for their elastic properties. In order to obtain realistic values for the elastic properties, the variations of some of the components of the stiffness tensor with respect to the size of the volume considered and the type of boundary conditions are investigated. The values of the components are found to converge to similar values as the size of the volume increases and the two types of boundary conditions studied (PMUBC and PBC) give similar values when the volumes have a size parameter δ equal to or larger than 1.6. The effect of the number of realizations is studied as well: after 10 realizations, the relative error is less than 10%. The computation of the additional components of the stiffness tensor reveals that large fibre networks ($\delta \geq 1.6$) exhibit a transverse isotropic like behaviour showing good agreement with the literature.

The influence of the fibre structure on the stiffness of the mineral wool fibre network is studied:

- As soon as β, the parameter that describes the main orientation of the fibres, reaches a value of 5, the fibre network behaves as a transverse isotropic material ($C_{11} \approx C_{22} \gg C_{33}$).
- When β is close to zero, a strong anisotropic behaviour is observed ($C_{33} \gg C_{11} \approx C_{22}$).
- When β is one, isotropic properties are obtained ($C_{11} \approx C_{22} \approx C_{33}$).

The curvature of a fibre affects the component C_{11} of the stiffness tensor as fibre networks with a strong curvature are up to 5 times less stiff than their straight fibres counterpart.

Finally the bonds between the fibres are varied from soft to stiff. An initial increase is observed for the transition of soft bonds to slightly stiffer but after this any further increase of the stiffness of the bond does not change the resulting stiffness of the fibre network.

5 Compressive behaviour of mineral wool

The compressive behaviour of a fibre network presents some singularities: because of the rearrangement of the fibres during loading and thus modification of the internal structure, load transfer occurs by creating new fibre contacts. The main consequence of this is the non-linearity of the stress-strain curve as a result of the creation and removal of contacts. In this chapter, existing models describing the compression of a random fibre network are reviewed. Results from experimental testing of a glass wool and a stone wool samples are presented and fitted to some of the models presented in the first section. The interpretation of the curves is supported by in-situ X-ray tomography compression testing where the fibre structure is observed at different compressive strains. Finally, the FEM model presented in Chapter 4 is developed further to simulate the compressive behaviour of mineral wool under cyclic loads. Several criteria related to the contacts between the fibres are introduced and explored in the model.

5.1 Analytical models describing the compression of random fibre networks

Several analytical models have been developed to describe the compressive behaviour of fibre networks. One of the earliest models presented in the literature was developed by van Wyk [94]. In the van Wyk model, a three dimensional random network of straight fibres with a Young´s modulus E is considered. The bending of the fibres is assumed to the predominant deformation in comparison to extension, compression and torsion of the fibres. Each fibre is supported by two adjacent fibres. With these assumptions, van Wyk established a power relation between the pressure applied P and the volume fraction of the fibres Φ:

$$P = kE\left(\Phi^3 - {\Phi_0}^3\right) \tag{5.1}$$

where k is a constant that accounts for the direction and location of contact force, the deformation direction and the crimp of fibres and Φ_0 is the volume fraction when the stress σ tends to 0.
Toll [95] demonstrated that all fibre entanglements, regardless of their specific fibre arrangement, follow a power law of exponent n. Toll showed that the exponent n is equal to 5 in the case of a 2D random structure and to 3 for a 3D random structure. He also found out experimentally that fibre

structures aligned with the direction of the compression gave values of n in the interval 7 and 15.5. The generalized expression for the van Wyk model is then:

$$P = kE(\Phi^n - {\Phi_0}^n) \tag{5.2}$$

When large strains are applied, Neckář et al. [96] assumed that the material has a minimal incompressible volume and thus has a maximal fibre volume fraction. This notion is introduced in the generalized expression of the van Wyk model developed by Toll [95] from Eq. (5.2) with the variable Φ_{MAX}:

$$P = kE\left(\frac{\Phi^n}{\left(1-\frac{\Phi}{\Phi_{MAX}}\right)^n} - \frac{\Phi_0^n}{\left(1-\frac{\Phi_0}{\Phi_{MAX}}\right)^n}\right) \tag{5.3}$$

The current fibre volume fraction Φ of the stone wool sample can be expressed as a function of the applied strain ε:

$$\Phi = \frac{\Phi_0}{1-\varepsilon} \tag{5.4}$$

where Φ_0 the initial fibre volume fraction can be expressed as:

$$\Phi_0 = \frac{\rho_s}{\rho_f} \tag{5.5}$$

where ρ_s is the density of the mineral wool product and ρ_f the density of fibre.

5.2 Compression cycles

Cyclic compression tests are carried out on stone wool and glass wool samples. The deformation speed and sample size are decided according to the standard EN 826. The first part of this section focuses on the compressive behaviour of a stone wool sample. Thereafter, the compression behabiour of stone wool and glass wool are compared with respect to thickness recovery and change in volume fraction after a cycle. The generalized van Wyk model from Eq.

(5.3) is fitted to the loading curves for each cycle and materials. The density of the samples used in this section is given in Table 5.1.

Table 5.1: Density of the mineral wool samples.

Sample	Density [kg/m^3]
Glass wool	15
Stone wool	34

5.2.1 Loading/unloading cycles of stone wool

The stress-strain curves are given in Figure 5.1. The curves are obtained after subjecting the sample to increasing loads and subsequent unloading steps until the load is back to 0.

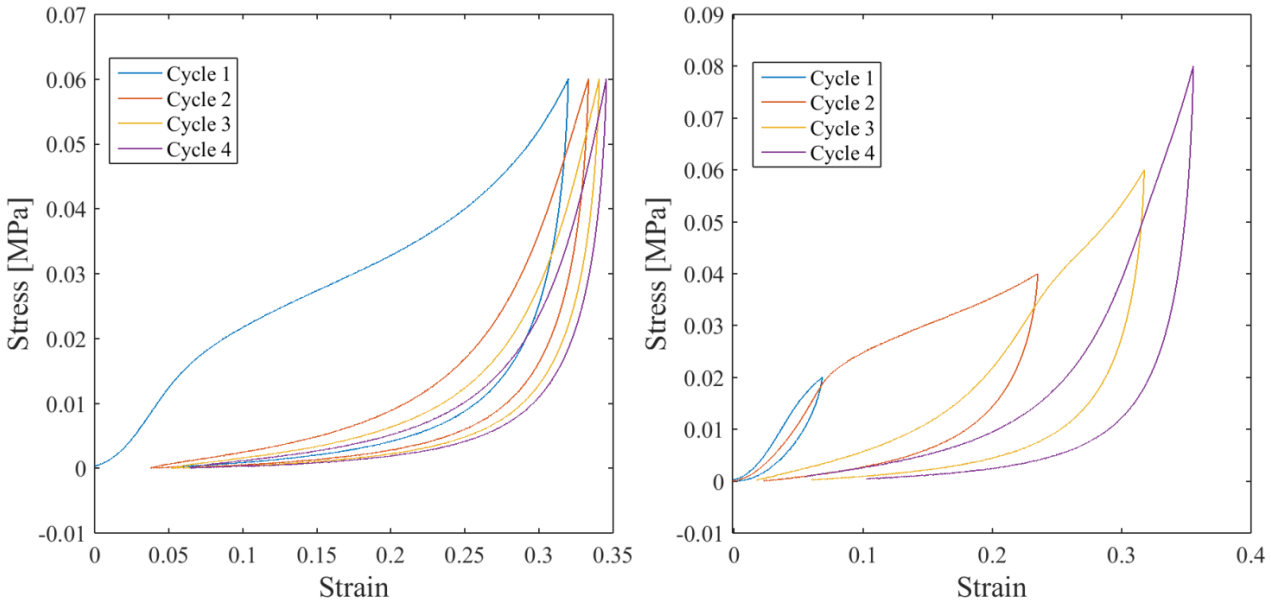

Figure 5.1: Left: Repeated loading/unloading cycles up to 0.06 MPa. Right: Loading/unloading cycles with increasing pressure.

In the plot of Figure 5.1, left, a linear part of the curve corresponding to the initial elastic deformation of the sample can be distinguished in the first cycle. This linear part is absent in the subsequent cycles which indicates that some irreversible damages are caused during the loading. Pocquillon et al. [97] reported the presence of the same linear elastic part in cross-linked fibres networks while the same behaviour was not observed in fibres networks with no bonds. It is then

concluded that the absence of the linear elastic part of the curve after application of a high pressure is due to the destruction of the bonds.

To determine at which stress level the linear elastic part of the curve disappears, the maximal stress applied to the sample is increased for 4 different cycles as shown in Figure 5.1, right. It is noticed that after an applied pressure of 60 kPa, the linear elastic part disappears.
The observed hysteresis is a consequence of the sliding and reorganization of the fibres. After the first loading, when the pressure is decreased until it becomes zero again, a residual strain exists. This indicates that the sample has not recovered its full thickness. The measured residual strain given in Table 5.2 is zero after the first cycle. In reality, since a hysteresis is observed, the residual strain is not exactly zero. For the subsequent cycles, the residual stain increases with the applied pressure. This behaviour indicates that some irreversible damages happen to the fibre structure either due to the destruction of the bonds, the breakage of the fibres or the interlocking of the fibres.

Table 5.2: Residual strains and fibre volume fraction Φ_f after each compression cycle of a stone wool sample.

Cycles	**Applied pressure [kPa]**	**Residual strain [%]**	$\boldsymbol{\Phi_f}$ **[%]**
1	20	0.0	1.33
2	40	2.4	1.36
3	60	6.0	1.41
4	80	10.3	1.48

5.2.2 Comparison between glass wool and stone wool

A glass wool and a stone wool sample are subjected to several load/unload cycles of maximal stress of 100 kPa. They have different initial density (respectively 15 kg/m3 and 34 kg/m3) and thus different fibre volume fractions. To compare the two materials, the relative variation of the fibre volume is used:

$$\Delta\Phi = \frac{\Phi_c - \Phi_0}{\Phi_c} \tag{5.6}$$

where Φ_c is the fibre volume fraction at the end of the loading part of the cycle and Φ_0 is the fibre volume fraction at the beginning of each cycle.

The first loading cycle is discarded as the van Wyk model does not apply on the first steep part of the curves. The pressure P is plotted as a function of the relative variations of the fibre volume fraction $\Delta\Phi$ for the cycles 2 and 3 in Figure 5.2.

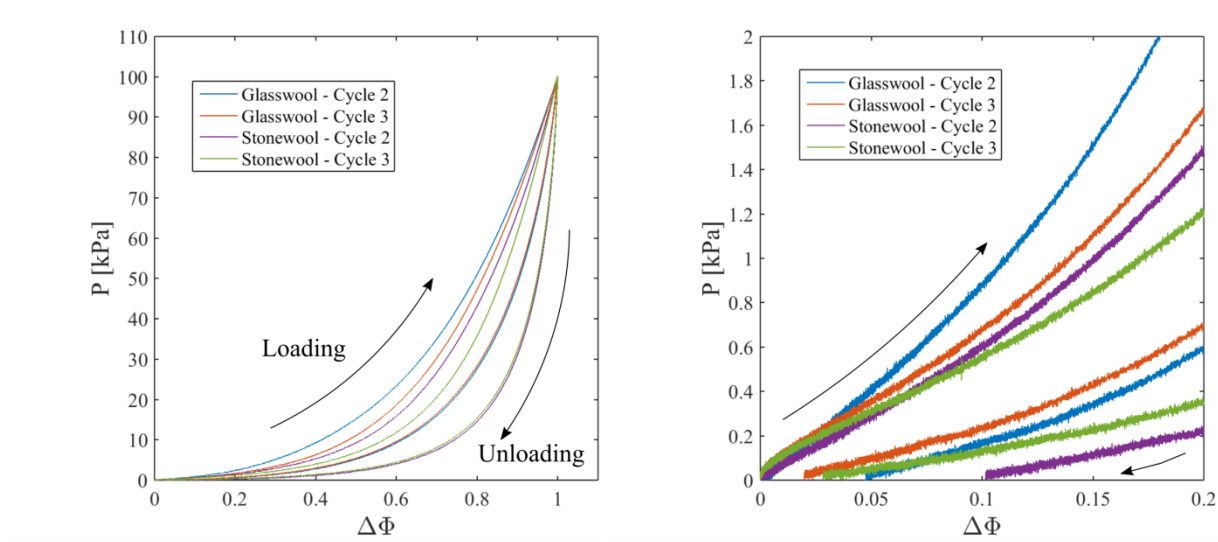

Figure 5.2: Pressure – Fibre volume fraction plots. The plot on the right is an inset obtained by zooming on the plot on the left in the range [0-0.2] for $\Delta\Phi$ and [0-2] kPa for P.

The relative variation in fibre volume fraction after each cycle is given in Table 5.3.

Table 5.3: Relative variations in fibre volume fraction after each compression cycle.

	$\Delta\Phi$ (Glass wool)	**$\Delta\Phi$ (Stone wool)**
Cycle 1	4.8 %	10.2 %
Cycle 2	2.0 %	2.8 %

The relative change of fibre volume fraction decreases with the number of cycles. This means that less and less irreversible changes take place after each cycle. In addition as indicated by the lower variations of the fibre volume fraction for the glass wool sample than for the stone wool specimen, the thickness recovery is higher for the glass wool sample.

The pressure P of two samples, one of glass wool and the other one of stone wool is plotted with respect to the current fibre volume fraction calculated using Eq. (5.4) for two subsequent loading cycles in Figure 5.3.

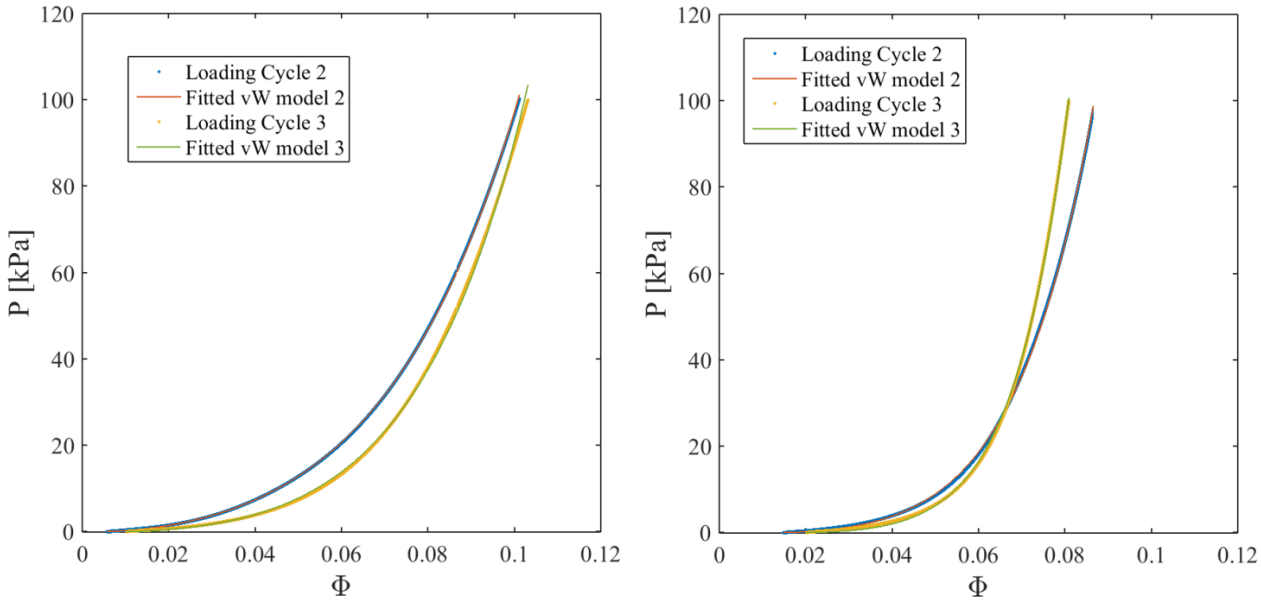

Figure 5.3: Plots of the compressive stress P as a function of the fibre volume fraction Φ (Left: Glass wool sample. Right: Stone wool sample).

The values of the exponent n are listed in Table 5.4. Previous work reported similar values for glass wool [98,99]. On the other hand, no corresponding data has been published for stone wool. The observed increase of the exponent n as a function of the number of cycles indicates that the number of contacts increases after each cycle due to a rearrangement of the fibres. After 3 cycles, it is observed that the exponent n of glass wool varies less than the exponent n of stone wool. This could indicate that fewer fibre arrangements takes place inside the glass wool material compared to the stone wool material. The values of the maximal volume fraction obtained by fitting are reported in Table 5.4.

Table 5.4: Exponent n for different cycles and samples and maximal fibre volume fraction Φ_{MAX}.

	Glass wool	**Stone wool**
n - Cycle 2	1.96	2.94
n - Cycle 3	2.37	3.72
Φ_{MAX}[%]	22.5	18.4

The maximal fibre volume fraction is higher for the glass wool than for the stone wool. This finding is expected considering that the stone wool presents a less layered structure than the glass wool (cf. results of the section 2.7.1).

The values obtained by fitting do not correspond to the values expected from the theory presented by Toll where the exponent n was found to reflect the orientation. Indeed, it was shown in Chapter 2 that the glass wool presents a lamellar structure and to a lesser extent so does the stone wool material. According to Toll, an exponent n of 5 should be obtained for 2D random material while lower exponents are obtained in these experiments. Reasons for discrepancy between the analytical model and the experimental results could be due to the fact that some of the hypothesis from the generalized van Wyk model does not apply to the material under consideration. For example, the model supposes that the fibres are cylinders with uniform diameter and length. Based on the findings of Chapter 2, this is not an accurate description of the mineral wool fibres. Similarly, the effect of the initial fibre volume fraction could also have an influence. Indeed Mezeix et al. [100] reported that the exponent n varies as a function of the initial fibre volume fraction for the same material. As the glass wool and the stone wool considered have different fibre volume fraction (respectively 0.6 % and 1.3 %), a fair comparison of the compressive behaviour of the glass wool and stone wool samples by fitting to the modified van Wyk model is not possible.

5.3 In-situ compression (X-ray CT study)

To investigate further the differences between glass wool and stone wool under compressive load and characterize the change in the fibre structure during compression, an in-situ test is conducted. In this test, the sample is compressed at three different strain levels and scanned at the end of each step with X-ray.

5.3.1 Experimental set-up

The sample is placed inside a thin polyimide tube with a diameter of 6 mm between two PMMA rods. Compressive loads are introduced through a screw in contact with the upper PMMA rod. The materials for the tube and the rods have been selected because they are invisible to the X-rays at the energy level considered. The X-ray tomography experiment is conducted on the same laboratory scanner as described in Chapter 2 with similar settings. The experimental step-up is described in Figure 5.4.

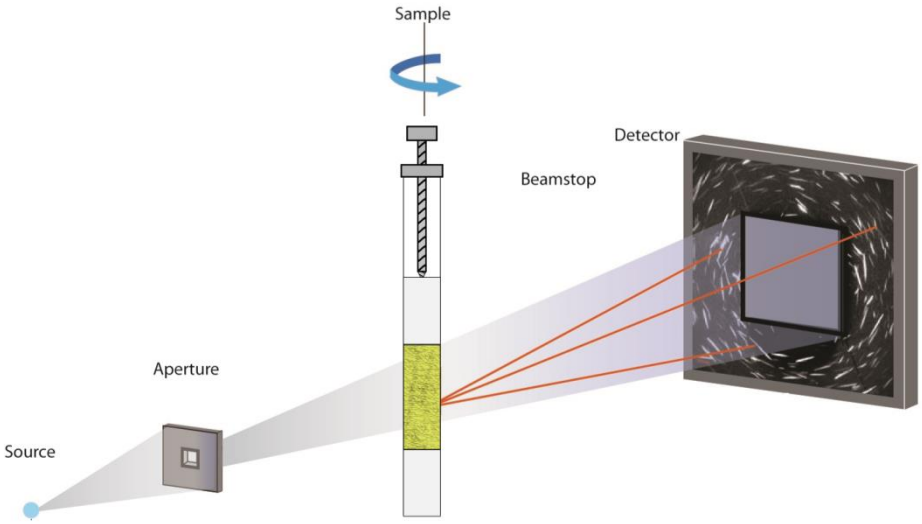

Figure 5.4: In-situ compression set-up in the laboratory scanner (modified from [101]).

Three loading steps are considered. Because of the way the load is introduced, it is not possible to adjust precisely the level of strain applied. Ultimately, the resulting strain for steps 2 and 3 are different for the glass wool and the stone wool sample as listed in Table 5.5. Furthermore no load measurement is possible in the current set-up. After each loading step, a scan of the material is acquired at a large field of view to visualize the thickness of the sample and then at a higher magnification to visualize the fibres.

Table 5.5: Applied strain ε at the different steps.

	Glass wool	**Stone wool**
ε (Step 1)	0 %	0 %
ε (Step 2)	72 %	53 %
ε (Step 3)	97 %	90 %

5.3.2 Quantitative analysis of the changes

The changes in the fibre orientation and pore distribution are analysed using the methods introduced in Chapter 2.

5.3.2.1 Change of orientation during compression

The histograms of the distributions of the elevation angles for each step are given in Figure 5.5. Each distribution is fitted to the probability density function introduced in Chapter 2, Eq. (2.9) to help the comparison between the two samples at different step.

A general observation is that the values obtained for β, the anisotropy parameter of Eq. (2.9) when no strain is applied (step 1) are lower than the ones estimated in Chapter 2. This is probably a consequence of the smaller volume size examined here. The parameter β increases with increasing applied compression strains from step 1 to step 2. This confirms the assumptions that the fibres undergo rearrangement and reorientation during the compression. From step 2 to step 3, β decreases for the glass wool sample. This could be the result of the curvature of the fibres due to the intersection with another fibre as the packing of the fibres increases at high strain.

5.3.2.2 Change of pores structures during compression

Using the local thickness method presented in Chapter 2, the mean pore size m_p is found to be around 121μm and 114 μm at the initial state. The histograms associated to the distribution of the pore size for each step are given in Figure 5.6. The mean value and the standard deviation decrease during compression. The decrease of the standard deviation indicates that the uniformity of the material increases with the applied strain.

5.3.3 Qualitative analysis

Analysis of the slices of the scanned data after compressing a glass wool sample to a 97% strain reveals that numerous fibres are broken. A few broken fibres are observed at a strain of 72 % as well but not to the same extent. Fractures are preferentially located on thick glass wool fibres. At an applied strain of 53 %, no broken fibres are detected in the images obtained from the scanning of stone wool. At 90%, the fractures of several stone wool fibres are noticed. Figure 5.7, top shows a few representative examples of broken fibres found in the glass wool (top) and in the stone wool (bottom) where the fractures are highlighted by red arrows.

Similarly to the glass wool specimen, the fractures in stone wool are located on thick fibres as well as on the shots. The presence of fractures on thick fibres can be linked to the fact that the probability of finding a surface flaw leading to the failure of the fibre is high for thick fibres. A

higher number of broken fibres is obtained after compression of glass wool than after compression of stone wool. This could be due to the larger strain applied but also could be explained by the presence of a population of thick glass wool fibres as evidenced in 2.7.2.

The breakage of the fibres into shorter pieces can help the rearrangement and reorientation of the fibres during loading and unloading of the specimen as the sliding of the fibres is easier for shorter fibres. This could facilitate the thickness recovery after compression and explain why the glass wool presents better recovery behaviour than the stone wool sample since it has been shown in Chapter 2, 2.7.2 that thick fibres are present in glass wool.

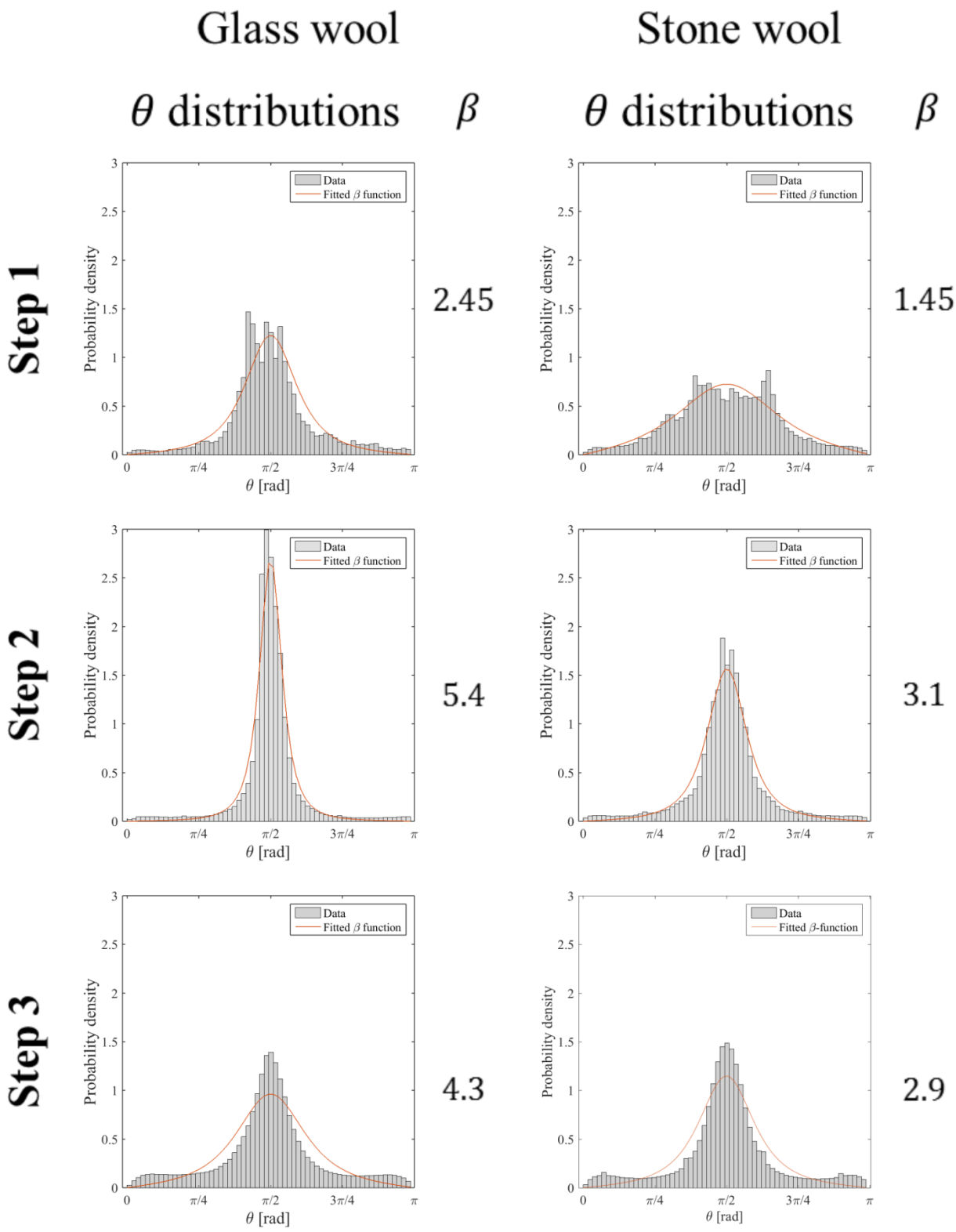

Figure 5.5: Variations of the orientation distribution during compression.

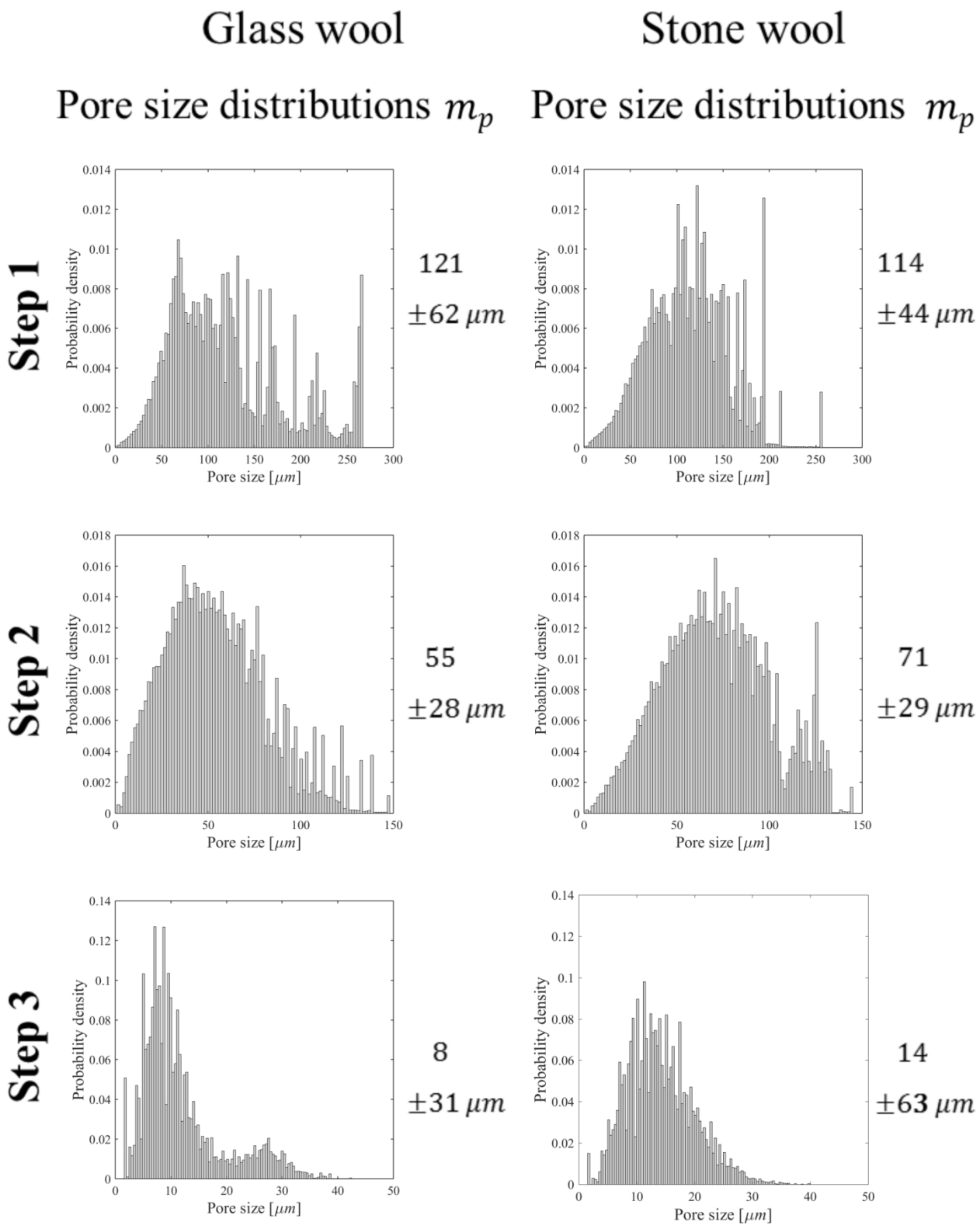

Figure 5.6: Variations of the pore sizes distribution during compression.

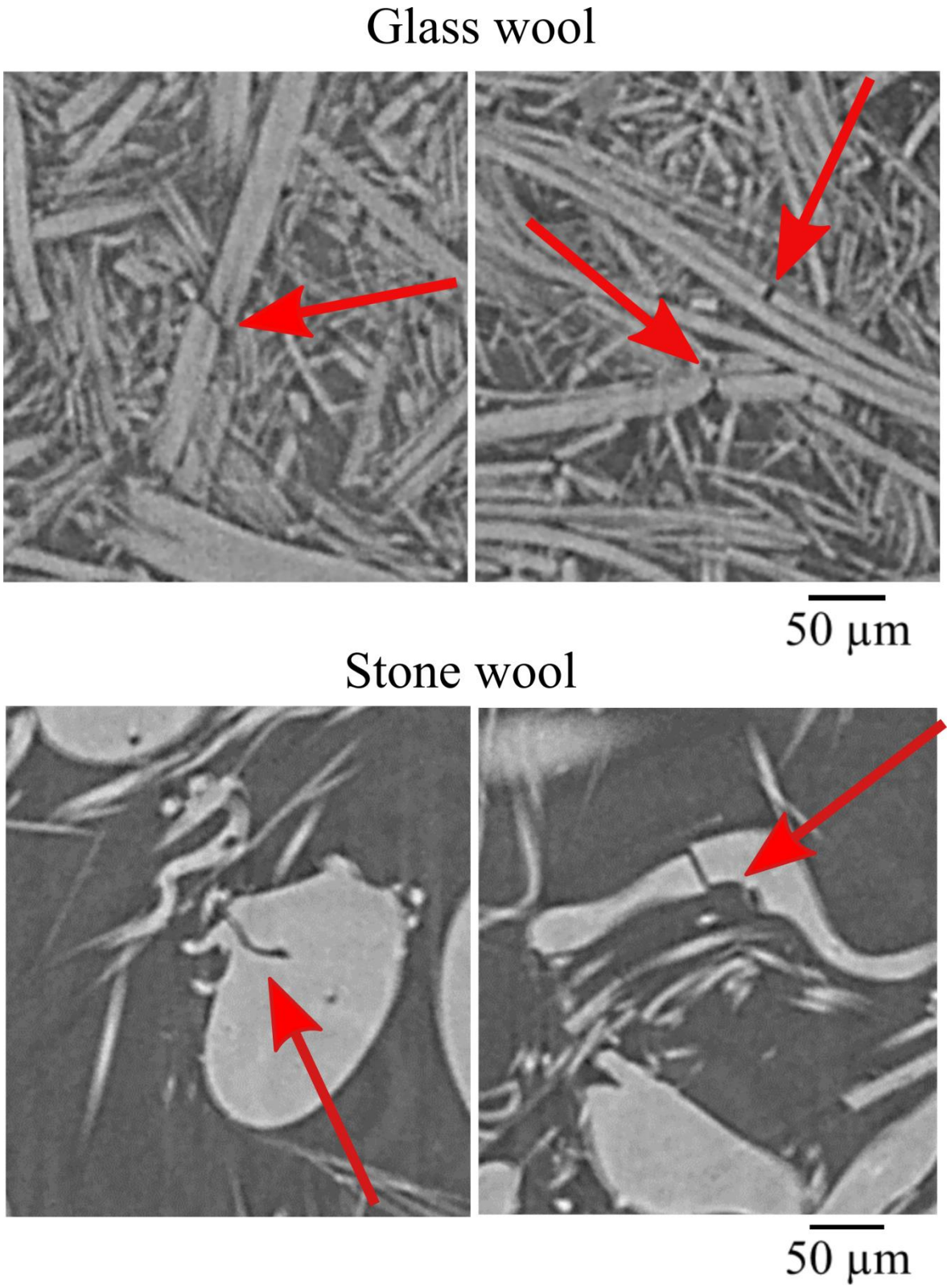

Figure 5.7: Fibre damages after application of the third level of strain.

5.4 Comparison with modelling

To validate some of the hypothesis about the mechanisms behind the compression and recovery of mineral wool samples formulated in the experimental section, a FEM model of a random fibre network representative of the stone wool and the glass wool sample is developed.

5.4.1 Implementation of the FEM model

The model is similar to the one described in Chapter 4. Fibres are modelled as beams and the binder bonds as springs. The boundary conditions implemented are the PMUBC. A compressive strain is applied. Two analytical rigid plates are added since the boundary conditions are defined for the nodes at the boundaries only. Indeed as the compression progresses, some of the fibres below the boundaries may not be subjected to any strain and stick out.

A general contact procedure is implemented in Explicit and a hard contact preventing penetration between two bodies is defined. The friction between the surfaces in contact can be adjusted.

In this section, since only the parameters related to the spring behaviour and contact are studied, the simulations are carried out on the smaller volumes where δ the size parameter introduced in Chapter 4 has a value of 1. If a study of the effect of microstructure parameter on the compression would be conducted, the size of the volume should be increased and several realizations should be performed for each fibre structure configurations.

5.4.2 Results of the FEM model

5.4.2.1 Simple model

In this first model, the bonds are modelled as axial and rotational springs without any failure behaviour. No friction behaviour is defined between the fibres and thus the sliding of the fibres is not limited. A compressive cycle is applied and the resulting plot of the stress-strain variations is shown in Figure 5.8, left. The hysteresis observed experimentally is reproduced by the model. However the linear elastic part is not as steep as expected. This most likely means that the bond density is too low.

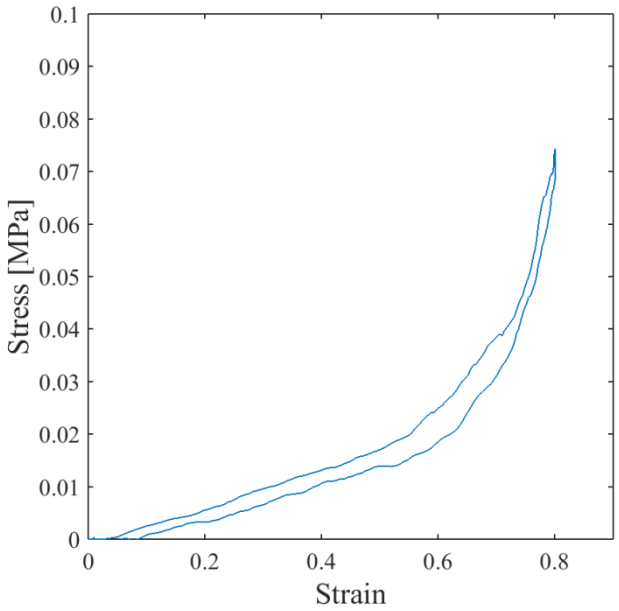

Figure 5.8: Plot of the strain-stress for one compression cycle of a simple model with no friction between the fibre surfaces and no failure of the bonds.

5.4.2.2 Effect of friction

The friction coefficient defining the tangential component of the contact forces between two fibres is adjusted between 0.1 and 0.8. The resulting stress-strain plots are given in Figure 5.9, right. As the friction coefficient increases, the hysteresis increases and the rearrangement created during loading become less and less reversible.

5.4.2.3 Effect of the bond failure

A simple failure criterion for the spring elements representing the binder bonds is implemented in the model: When the force in the spring element is superior to 0.1 N, the element fails and is no longer active in the model. The results of this study are shown in Figure 5.9, right. The model without the bond failure behaviour presents the linear elastic slope at the beginning of the loading. This was also observed in the previous models and experimentally. On the other hand, the first part of the loading curve for the model with the bond failure criterion is not as steep. This confirms that the first linear part of the curve is controlled by the binder in the mineral wool material.

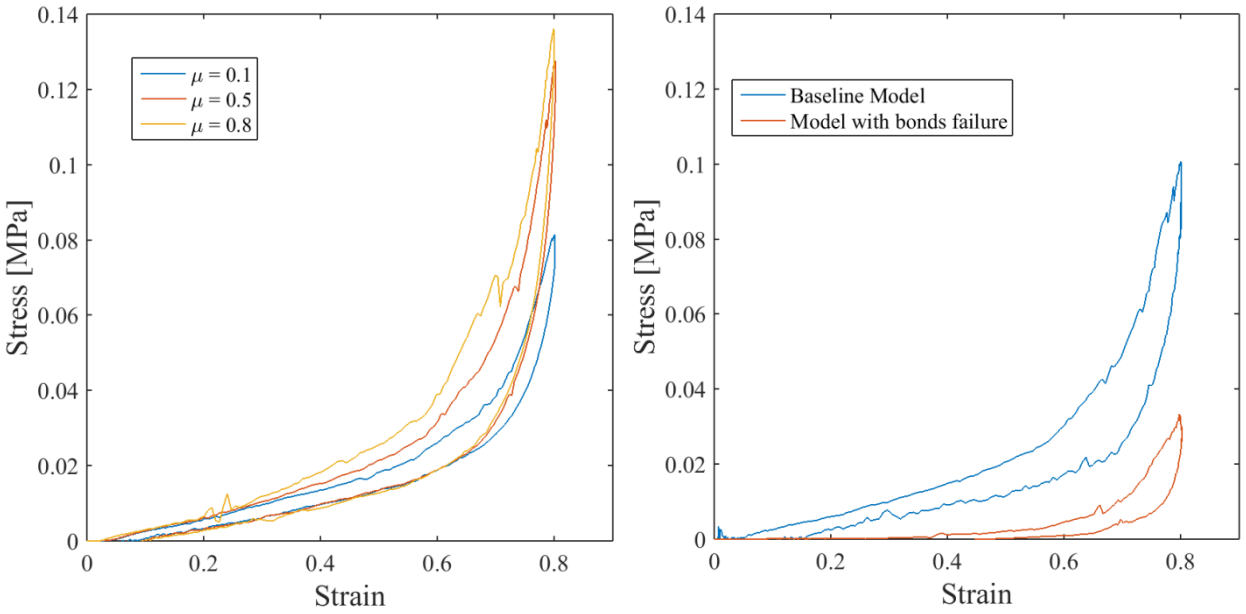

Figure 5.9: Plots of the strain-stress variations for one compression cycle of models with different value of friction coefficient μ (left) and with and without a failure criterion for the bonding elements (right).

5.5 Summary

In this chapter, the non-linear behaviour of mineral wool fibre networks under compressive loads is highlighted. A first linear elastic slope is observed at low applied strain during the first compression cycle. This behaviour disappears in the subsequent loading cycle providing that the applied load is high enough (for the stone wool, this threshold is evaluated at 60 kPa). The hysteresis indicates that irreversible changes in the fibre structure take place during the compression. A residual strain subsides when the pressure goes back to 0 kPa after a cycle indicating that the samples do not recover fully their initial thickness. The recovery is more incomplete for the stone wool sample than the glass wool sample.

The stress variations as a function of the fibre volume fraction after one cycle are well described by a Power law as predicted by similar results in the literature. A modified van Wyk model where the incompressible volume is included is fitted to the secondary loading curves of a glass wool and a stone wool sample. The value of the exponent of the Power law increases with the loading cycles and is significantly higher for the stone wool curves. These findings do not agree with the theory of Toll where the orientation is reflected by the exponent of the power law where a higher exponent

should be obtained for the material presenting a stronger orientation in the x-y plane. In the present study, the glass wool specimen should have the highest value. This indicates that some of the hypotheses Toll used to develop his analytical model are not realistic for the material studied here.

The changes of the fibre and pore structures are confirmed by X-ray investigations of samples at different compression stages. During compression, the fibres reorient and a more lamellar structure is obtained. This reorientation is more significant for the stone wool sample which initially does not present a structure as lamellar as the glass wool material. The distribution of the pores becomes narrower with the increasing compressive loads and centres around smaller mean values.
At the end of the compression steps, the fibre materials present more uniformity in terms of pores distribution and inclination with the z-axis. The fact that the changes in glass wool sample are not as drastic as the ones experimented by the stone wool sample could explain why the recovery properties of the latter are worse than those of the former. Another important result of the X-ray investigations is the evidence of fibre damage at high strain. At such high strain, the fibre volume fraction is well above the maximal fibre volume fraction found when fitting the experimental curves to the modified van Wyk model and the only way to sustain the high load for the fibre structure is the breakage of the fibres into smaller pieces.

To better explain the effect of the hysteresis and the lack of recovery, the FEM model of Chapter 4 is developed to test the virtual volumes under a compressive cyclic loading case. The simplest implementation of the model with no friction reproduces the hysteresis observed in the experiments. Other findings highlight the role of the friction on the size of the hysteresis. It is shown that improving the sliding between the fibre surface results in a higher thickness recovery.

6 Conclusions

This PhD work fulfilled the three goals that have been outlined in the introduction. The first goal is related to the characterization of the fibre structure of mineral wool materials. Two imaging techniques have been employed for this task: SEM and X-ray tomography. Analysis of the data obtained by X-ray tomography using tools developed or implemented in this PhD gives information on the fibre orientation, fibre diameter and pore size distribution of stone wool and glass wool materials. The findings can be summarized as follows:

- Glass wool and stone wool fibres are preferably oriented horizontally in the x-y plane. This orientation preference is even more marked for glass wool than stone wool. In the x-y plane, the glass wool fibres possess a preferential orientation compared to the stone wool fibres.
- The mean fibre diameter of the two materials is similar but their distribution is different. Two populations of glass wool fibres can be differentiated in terms of fibre diameter: One presenting a fibre diameter smaller than the stone wool fibres and one significantly larger.
- Finally the distribution of the pore size demonstrates that the glass wool fibres are arranged with more uniformity than the stone wool fibres.

At the end of Chapter 2, it is proposed that the origins of the quantified differences can be traced back to the respective production process of glass wool and stone wool.

In order to quantify the effect of the fibre structure on the mechanical properties of the products, a numerical homogenization approach is adopted. The first step consists of the generation of a virtual fibre network using probability densities fitted to the distributions obtained in Chapter 2. The generation algorithm satisfies several important criteria such as:

- Non-overlaps of the fibres.
- Control of the fibre curvature and main orientation.
- Possibility to generate high aspect ratio fibres.

Important modifications are brought to the fibre model proposed in the literature to better represent a real mineral wool fibre: The fibre is modelled as a chain of spherocylinders rather than a chain of overlapping spheres. This change in the fibre model entails further modifications of the algorithm to detect overlap between fibres. The fitted virtual volumes are imported in an FEM model where the fibres are modelled as beams and the binder as springs. The following statements are established based on extensive simulation campaigns:

- Both boundary conditions (PMUBC and PBC) converge towards the same effective properties when the volumes have a size parameter δ superior or equal to 1.6.
- The effect of the number of realizations is studied as well: After 10 realizations, the relative error is less than 10%.
- Large fibre networks exhibit a transverse isotropic behaviour.
- Highly lamellar structures such as glass wool and loosely lamellar as observed in the stone wool material will affect the resulting elastic properties of the product considerably.

Finally, all the methods developed for the characterization of mineral wool materials and the modelling of their mechanical properties are applied to the study of the compressive behaviour of glass wool and stone wool.

- The residual strain is higher for stone wool than for glass wool which confirms the superior thickness recovery of the latter. The fit of the experimental curves with the generalized van Wyk model where the variations of the pressure applied with the fibre volume fraction are expressed by a power law gives a higher exponent for the power law and a lower incompressible volume for stone wool compared to glass wool. This could partly explain the difference in thickness recovery.
- The hysteresis can be attributed to the reorganization of the fibres inside the material. In-situ X-ray CT evidences the changes in fibre orientation and pore structure as well as the presence of fibre damages.
- The FEM modelling confirms that friction between fibres plays an important role on the size of the hysteresis and the thickness recovery. It is found that a higher friction between the fibres prevents the rearrangement of the fibres and limits the recovery.

To conclude, the model developed in this PhD work is a valuable tool for the mineral wool industry. Important parameters governing the elastic and compressive properties can be identified and their influence on the mineral wool product can be assessed without extensive experimentations.

7 Perspectives

Further work will focus on the characterization of two important characteristics of the mineral wool fibre networks:

- Quantification of the fibre length.
- Distribution of the binder.

The former is not possible in the current study because of the limited size of the volume considered in X-ray tomography. The latter is never evidenced in the data obtained in this PhD work. Future investigations will explore the possibility of increasing the contrast between the organic binder and the inorganic fibres using special contrast agents often used in the observation of biological samples.

The methodology developed in this work provides new descriptors to quantify the mineral wool product at a microscopic and a mesoscopic scale. These new descriptors will help explaining differences in product properties observed from one factory line to another. For example, different techniques are employed in the ROCKWOOL Group to collect the fibres after the cascade spinning process resulting in a different arrangement of the fibres. The effect of the fibre collection can now be quantified with the developed methodology.

With regards to the elastic properties, other parameters such as the fibre aspect ratio, the distribution of the binder and the local variations of the fibre volume fraction will be studied as well. With the FEM model developed, the effect of changes in the fibre structure due to a different production process can be predicted in terms of elastic properties. This virtual testing will support or even replace expensive line trials and prototypes and guide the developer of a new product towards the optimized fibre structure for a specific application.

Finally, an extensive study of different parameters such as fibre aspect ratio, curvature, orientation, initial fibre volume fractions, and bond density will be conducted in order to understand the role of these parameters on the hysteresis observed during cyclic compression. The results of these investigations should further solidify the understanding of the mechanisms of deformation and relaxation inside mineral wool products subjected to such loads during packaging and transport. The findings will hopefully be translated into specific recommendations for improvement of the thickness recovery of mineral wool products. The current results underline the importance of

friction on the hysteresis and thickness recovery of the products. In the mineral wool fibre network, oil is often added to promote the water-repellence of the products. It would be interesting to evaluate whether the oil can act as a lubricant facilitating sliding of the fibres and help the recovery.

8 References

[1] O. Väntsi, T. Kärki, Resour. Conserv. Recycl. 104 (2015) 38.

[2] O. Väntsi, T. Kärki, Constr. Build. Mater. 55 (2014) 220.

[3] A. Cheng, W.-T. Lin, R. Huang, Mater. Des. 32 (2011) 636.

[4] EURIMA, Http://www.eurima.org/about-Mineral-Wool/production-Process.html (2016).

[5] K.K. Jakobsen, Insulation System for Covering a Facade of a Building, 2014.

[6] B. Bellmann, H. Muhle, O. Kamstrup, U.F. Draeger, Exp. Toxicol. Pathol. Off. J. Gesellschaft Für Toxikologische Pathol. 47 (1995) 195.

[7] M. Guldberg, Ann. Occup. Hyg. 42 (1998) 233.

[8] N. Kohyama, Ind. Health 35 (1997) 126.

[9] A. Campopiano, A. Cannizzaro, F. Angelosanto, M.L. Astolfi, D. Ramires, A. Olori, S. Canepari, S. Iavicoli, Regul. Toxicol. Pharmacol. 70 (2014) 393.

[10] J.-Y. Buffiere, E. Maire, J. Adrien, J.-P. Masse, E. Boller, Exp. Mech. 50 (2010) 289.

[11] J.P. James, H.-W. Choi, J.G. Pharoah, Int. J. Hydrogen Energy 37 (2012) 18216.

[12] A. Pfrang, S. Didas, G. Tsotridis, J. Power Sources 235 (2013) 81.

[13] H. Tran, P. Doumalin, C. Delisee, J.C. Dupre, J. Malvestio, a. Germaneau, J. Mater. Sci. 48 (2012) 3198.

[14] E. Maire, P. Colombo, J. Adrien, L. Babout, L. Biasetto, J. Eur. Ceram. Soc. 27 (2007) 1973.

[15] G. Gaiselmann, I. Manke, W. Lehnert, V. Schmidt, Image Anal. Stereol. 32 (2013) 57.

[16] H. Altendorf, D. Jeulin, Image Anal. Stereol. 28 (2009) 143.

[17] S. Pandita, I. Verpoest, Compos. Sci. Technol. 63 (2003) 311.

[18] P. Badel, E.V. Sallé, E. Maire, P. Boisse, Int. J. Mater. Form. 2 (2009) 189.

[19] J. Pazmino, V. Carvelli, S. V. Lomov, Compos. Part A Appl. Sci. Manuf. 61 (2014) 76.

[20] X. Zeng, L.P. Brown, A. Endruweit, M. Matveev, A.C. Long, Compos. Part A Appl. Sci. Manuf. 56 (2014) 150.

[21] I. Straumit, S. V Lomov, M. Wevers, Compos. Part A 69 (2015) 150.

[22] C.N. Eberhardt, a. R. Clarke, J. Microsc. 206 (2002) 41.

[23] M. Tausif, B. Duffy, S. Grishanov, H. Carr, S.J. Russell, Microsc. Microanal. (2014) 1.

[24] M. Aronsson, in:, 16th Int. Conf. Pattern Recognit., 2002.

[25] S. Rolland du Roscoat, M. Decain, X. Thibault, C. Geindreau, J.-F. Bloch, Acta Mater. 55 (2007) 2841.

[26] F. Hild, E. Maire, S. Roux, J.-F. Witz, Acta Mater. 57 (2009) 3310.

[27] E. Maire, J. Adrien, F. Hild, S. Roux, J.-F. Witz, in:, Conf. Proc. Soc. Exp. Mech., 2013, pp. 291–298.

[28] P. Perona, J. Malik, IEEE Trans. Pattern Anal. Mach. Intell. 12 (1990) 629.

[29] J. Bigun, G.H. Granlund, J. Wiklund, IEEE Trans. Pattern Anal. Mach. Intell. 13 (1991) 775.

[30] J. Weickert, in:, Proc. Comput. Anal. Images Patterns, 6th Int. Conf. CAIP '95 Prague, Czech Republic, Sept. 6–8, 1995, 1995, pp. 230–237.

[31] U. Köthe, Ger. Assoc. Pattern Recognit. (2003) 25.

[32] M.D. Budde, J. a. Frank, Neuroimage 63 (2012) 1.

[33] L.J. Van Vliet, F.G.A. Faas, Proc. - Int. Conf. Pattern Recognit. 3 (2006) 856.

[34] H. Scharr, M.J. Black, H. Haussecker, in:, Proc. Ninth IEEE Int. Conf. Comput. Vis., IEEE, 2003, pp. 840–847 vol.2.

[35] N. Lassoued, P. Babin, G. Della Valle, M.F. Devaux, A.L. Réguerre, Food Res. Int. 40 (2007) 1087.

[36] C. Peyrega, D. Jeulin, C. Delisée, J. Lux, Image Anal. Stereol. 28 (2009) 129.

[37] J. Lux, C. Delisée, X. Thibault, Image Anal. Stereol. 25 (2006) 25.

[38] G. Standfest, S. Kranzer, A. Petutschnigg, M. Dunky, J. Adhes. Sci. Technol. 24 (2010) 1501.

[39] J. Lux, A. Ahmadi, C. Gobbé, C. Delisée, Int. J. Heat Mass Transf. 49 (2006) 1958.

[40] C. Redenbach, I. Vecchio, Compos. Sci. Technol. 71 (2011) 107.

[41] R. Moreno, M. Borga, in:, SPIE 8314 Med. Imaging, San Diego, 2012.

[42] J. Becker, R. Flückiger, M. Reum, F.N. Büchi, F. Marone, M. Stampanoni, J. Electrochem. Soc. 156 (2009) B1175.

[43] R. Dougherty, K.-H. Kunzelmann, Microsc. Microanal. 13 (2007) 1678.

[44] K. Palagyi, A 3D-Subiteration Thinning Algorithm for Extracting Medial Lines, 1998.

[45] D. Stoyan, J. Mecke, S. Pohlmann, Ser. Stat. 11 (1980) 281.

[46] H. Altendorf, D. Jeulin, Phys. Rev. E 83 (2011) 041804.

[47] K. Schladitz, S. Peters, D. Reinel-Bitzer, A.Wiegmann, J. Ohser, Comput. Mater. Sci. 38 (2006) 56.

[48] a. R. Koenig, R.D. Hamilton, T.E. Laskowski, J.R. Olson, J.F. Gordon, V.R. Christensen, C.D. Byers, Anal. Chim. Acta 280 (1993) 289.

[49] Otsu, IEEE Trans. Syst. Man. Cybern. 9 (1979) 62.

[50] G. Matheron, Random Sets and Integral Geometry, Wiley, New York, 1975.

[51] J. Dirrenberger, S. Forest, D. Jeulin, Int. J. Solids Struct. 51 (2014) 359.

[52] R. Thiedmann, F. Fleischer, C. Hartnig, W. Lehnert, V. Schmidt, J. Electrochem. Soc. 155 (2008) B391.

[53] M. Tatlier, L. Berhan, Phys. Status Solidi 246 (2009) 2018.

[54] O. Wirjadi, Models and Algorithms for Image-Based Analysis of Microstructures, Kaiserslautern University, 2009.

[55] S. Kärkkäinen, A. Miettinen, T. Turpeinen, J. Nyblom, P. Pötschke, J. Timonen, Image Anal. Stereol. 31 (2012) 17.

[56] M. Faessel, C. Delisée, F. Bos, P. Castéra, Compos. Sci. Technol. 65 (2005) 1931.

[57] D. Durville, J. Mater. Sci. 40 (2005) 5941.

[58] J. Feder, J. Theor. Biol. 87 (1980) 237.

[59] F. Naddeo, N. Cappetti, A. Naddeo, Comput. Mater. Sci. 81 (2014) 239.

[60] Y. Pan, Stiffness and Progressive Damage Analysis on Random Chopped Fiber Composite Using FEM, Rutgers, The State University of New Jersey, 2010.

[61] H. Moussady, A New Definition of the Representative Volument Element in Numerical Homogenization Problems and Its Application to the Performance Evaluation of Analytical Homogenization Models, Ecole Polytechnique de Montréal, 2013.

[62] N. Provatas, M. Haataja, J. Asikainen, S. Majaniemi, M. Alava, T. Ala-Nissila, Colloids Surfaces A Physicochem. Eng. Asp. 165 (2000) 209.

[63] A. Ekman, A. Miettinen, T. Turpeinen, K. Backfolk, J. Timonen, Nord. Pulp Pap. Res. J. - Pap. Phys. 27 (2012) 270.

[64] A. Kulachenko, T. Uesaka, Mech. Mater. 51 (2012) 1.

[65] L.T. Curto, Joana M R, Eduardo, in:, XXI Tec. Conf. Exhib. CIADICYP, Lisbon, Portugal, 2010.

[66] Y. Pan, L. Iorga, A. a. Pelegri, Compos. Sci. Technol. 68 (2008) 2792.

[67] Q. Wang, B. Maze, H.V. Tafreshi, B. Pourdeyhimi, Model. Simul. Mater. Sci. Eng. 15 (2007) 855.

[68] A. Bezrukov, D. Stoyan, Part. Part. Syst. Charact. 23 (2006) 388.

[69] E. Ghossein, M. Lévesque, J. Comput. Phys. 253 (2013) 471.

[70] K. Kremer, G.S. Grest, J. Phys. Condens. Matter 2 (1990) SA295.

[71] J. Moscinski, Bargiel Monika, Rycerz; Katarzyna, Jacobs Patrick, Mol. Simul. 3

(1989).

[72] G. Gaiselmann, D. Froning, C. Tötzke, C. Quick, I. Manke, W. Lehnert, V. Schmidt, Int. J. Hydrogen Energy 38 (2013) 8448.

[73] MATLAB, Version 8.15.0 (2015a), The MathWorks Inc., Natick, Massachusetts, 2015.

[74] Dassault Systèmes, Notes 92 (2012) 815.

[75] L.T. Harper, C. Qian, T.A. Turner, S. Li, N.A. Warrior, Compos. Sci. Technol. 72 (2012) 204.

[76] L.T. Harper, C. Qian, T.A. Turner, S. Li, N.A. Warrior, Compos. Sci. Technol. 72 (2012) 225.

[77] Z. Lu, Z. Yuan, Q. Liu, Comput. Mater. Sci. 90 (2014) 123.

[78] H. Berger, S. Kari, U. Gabbert, R.R. Ramos, J.B. Castillero, R.G. Díaz, J. Mech. Mater. Struct. 2 (2007) 1561.

[79] X. Hou, M. Acar, V. V. Silberschmidt, Comput. Mater. Sci. 50 (2011) 1292.

[80] E. Demirci, M. Acar, B. Pourdeyhimi, V. V Silberschmidt, Comput. Mater. Sci. 50 (2011) 1286.

[81] F. Farukh, E. Demirci, B. Sabuncuoglu, M. Acar, B. Pourdeyhimi, V. V. Silberschmidt, Int. J. Solids Struct. 51 (2014) 1670.

[82] A. Ridruejo, C. González, J. LLorca, J. Mech. Phys. Solids 58 (2010) 1628.

[83] B. Sabuncuoglu, M. Acar, V. V. Silberschmidt, Comput. Mater. Sci. 79 (2013) 143.

[84] L. Berhan, J. Appl. Phys. 95 (2004) 5027.

[85] W.A. Bosbach, PLoS One 10 (2015) e0143011.

[86] Q. Liu, Z. Lu, Z. Hu, J. Li, Mater. Sci. Eng. A 587 (2013) 36.

[87] C. Huet, J. Mech. Phys. Solids 38 (1990) 813.

[88] K. Sab, Eur. J. Mech. A Solids 11 (1992) 585.

[89] T. Kanit, S. Forest, I. Galliet, V. Mounoury, D. Jeulin, Int. J. Solids Struct. 40 (2003) 3647.

[90] D.H. Pahr, P.K. Zysset, Biomech. Model. Mechanobiol. 7 (2008) 463.

[91] I. Gnip, S. Vejelis, V. Kersulis, S. Vaitkus, Constr. Build. Mater. 24 (2010) 2124.

[92] V. Tarnow, J. Acoust. Soc. Am. 108 (2000) 2243.

[93] J.-F. Witz, S. Roux, F. Hild, J. Rieunier, J. Eng. Mater. Technol. 130 (2007) 1.

[94] C.M. van Wyk, J. Text. Inst. Trans. (1946).

[95] S. Toll, Polym. Eng. Sci. 38 (1998) 1337.

[96] B. Neckář, Text. Res. J. 67 (1997) 123.

[97] D. Poquillon, B. Viguier, E. Andrieu, J. Mater. Sci. 40 (2005) 5963.

[98] M. Baudequin, G. Ryschenkow, S. Roux, Eur. Phys. J. B - Condens. Matter Complex Syst. 12 (1999) 157.

[99] A. Allaoui, Comportement Mécanique et Électrique Des Enchevêtrements de Nanotubes de Carbone, École Centrale Paris, 2005.

[100] L. Mezeix, C. Bouvet, J. Huez, D. Poquillon, J. Mater. Sci. 44 (2009) 3652.

[101] S.A. McDonald, P. Reischig, C. Holzner, E.M. Lauridsen, P.J. Withers, A.P. Merkle, M. Feser, Sci. Rep. 5 (2015) 14665.

Appendix

[P1]: Microstructural characterization of stone wool fibre network

MICROSTRUCTURAL CHARACTERIZATION OF STONE WOOL FIBRE NETWORK

L. Chapelle[a,b*], P. Brøndsted[b], Y. Kusano[b] , M. R. Foldschack[a]

[a] *Group Research & Development, Rockwool International A/S, Hovedgaden 584, 2640 Hedehusene, Denmark*
[b] *Department of Wind Energy, Section of Composites and Materials Mechanics, Technical University of Denmark, Risø Campus, Frederiksborgvej 39, 4000 Roskilde, Denmark*
**lucie.chapelle@rockwool.com*

Keywords: stone wool, 3D image analysis, x-ray tomography

Abstract
Understanding the mechanical properties of fibrous network as complex as stone wool materials requires a relevant description of their microstructure and architecture. In this study, different methods have been proposed to characterize the fibre orientation, diameter and length of fibres as well as the number density of fibre contacts. The methods are based on image analysis of 3D datasets which have been obtained by x-ray tomography. Validation of the proposed methods was demonstrated by testing generated virtual fibrous network with known fibre characteristics.

1. Introduction

Fibrous materials such as stone wool find applications in the building industry as thermal and acoustic insulators. Previous studies have focused on their thermal and acoustic properties [1-4]. However, other properties such as mechanical strength and durability are also of interest. It is because, for example, during transportation, storage or installation on the construction site, stone wool products are compressed. The macroscopic mechanical properties of stone wool materials are highly influenced by the microstructure such as the fibre network geometry, in particular the orientation distribution of the fibres and the number density of contact points between fibres. Characterization of the microstructure of stone wool is therefore needed to gain an understanding of the macroscopic mechanical properties of stone wool.

X-ray tomography is a powerful tool for the characterization of complex microstructure and their evolution under varying conditions. For instance, porosity content, shape, fibre orientation, diameter, length and tortuosity have been measured and estimated for stone wool by processing and analysing 3D datasets obtained by x-rays tomography [5-8]. Other x-ray tomography experiments involved in-situ loading to observe the strain field during compression of stone wool [9]. Studies have also focussed on detecting fibre contacts. Most of proposed methods consist of extracting the geometrical skeleton of the fibres using a homotopic thinning algorithm. The obtained branches are then classified and merged when belonging to a same fibre [5,10-12]. A method has been proposed in [13] using a local orientation map to detect fibre contacts and then proceed to fibre segmentation.
In this work, we propose methods to estimate the fibre orientation and diameter distribution in a fibrous network where individual fibre segmentation is not a pre-requisite. We also propose

a method based on fibre segmentation to find the number of contacts between fibres and determine their length distribution.

2. Materials and methods

2.1 Materials

Stone wool fibres studied are discontinuous glass fibres with a diameter of approximately 3 µm and a length up to a centimetre. They are normally produced by a wheel centrifuge process known as cascade spinning where droplets of melts are drawn into fibres by centrifugal forces. Binder and refined mineral oil are subsequently added to make the material both stable and water repellent. The treated stone wool is then heated in order to cure the binder. The sample chosen for the study is taken from a semi-rigid insulation board commercialized under the name ROCKWOOL Super Flexibatts® with a density of approximately 50 kg/m^3.

2.2 Image Acquisition

Tomography scans were carried out using a high resolution micro-CT system at the Technical University of Denmark (DTU) Imaging Centre. The sample was rotated with an angular increment of 0.1125º. To increase the signal to noise ratio (SNR) of the images, 3200 frames were captured and averaged for each projection on a 2012 x 2012 bit detector array. The 3D image has a size of 1960 x 2012 x 1970 voxels with a voxel size of 0.7964^3 µm^3.

2.3 Fibre orientation

The orientation of the fibres in stone wool was determined using the structure tensor analysis [14]. Let I be the discrete function describing the grey-value intensities of a 3D image and let $p \in \mathbb{R}^3$ be a point belonging to a fibre on I. Because the intensity values along a fibre are locally constant, a vector $v \in \mathbb{R}^3$ exists such that:

$$\big(I(p+v) - I(p)\big)^2 \approx 0 \tag{1}$$

$$|v| = 1 \tag{2}$$

An orientation vector $w(p)$ can be found by setting:

$$w(p) = argmin_{|v|=1}\left(\big(I(p+v) - I(p)\big)^2\right) \tag{3}$$

The expression from equation (1) can be decomposed into a Taylor series:

$$\big(I(p+v) - I(p)\big)^2 \approx \big(v^T \nabla I(p)\big)^2 = v^T \nabla I(p) v^T \nabla I(p) = v^T (\nabla I(p) \nabla I(p)^T) v \tag{4}$$

The minimization problem becomes then:

$$w(p) = argmin_{|v|=1}(v^T(ST)v) \tag{5}$$

where $\boldsymbol{ST} = \boldsymbol{\nabla I(p)\nabla I(p)^T}$ designates the structure tensor.

The orientation vector, *w(p)* is thus the eigenvector corresponding to the smallest eigenvalues of the structure tensor.

The image is first smoothed with an isotropic Gaussian kernel K_ρ of size m_1 and standard deviation ρ. A derivative along each direction *x*, *y* or *z* is computed for each voxel by convolving the image with Sobel-type Sharr operators. The component (J_{ij}) of the structure tensor is expressed as the product of the derivative of the image in the direction *i* with the derivative in the direction *j*, convolved with a second Gaussian filter of kernel size m_2 and standard deviation σ.

$$ST = \begin{bmatrix} J_{xx} & J_{xy} & J_{xz} \\ J_{xy} & J_{yy} & J_{yz} \\ J_{xz} & J_{yz} & J_{zz} \end{bmatrix} \; where \; J_{ij} = K_\sigma * \left(\frac{\partial (K_\rho * I)}{\partial i} \cdot \frac{\partial I (K_\rho * I)}{\partial j} \right) \tag{6}$$

2.4 Fibre diameter

The size distribution of an object of a set *X* can be assessed through successive openings by a structuring element of growing size. This is referred to as granulometry by openings. For each voxel *p* of an image *I*, we can define the granulometric or pattern spectrum, $PS_{\gamma_n}(p)$ as:

$$\forall\, n > 0, PS_{\gamma_n}(p) = \varphi\left(\psi_n\big(I(p)\big)\right) - \varphi\big(\psi_{n-1}(I(p))\big) \tag{7}$$

where ψ_n is an opening with a structuring element of size *n* and φ is a measure function. For example for a grayscale image, this can simply be the intensity of the voxel. If *X* is the set of fibres and if the structuring element is a ball of radius n, the granulometric curve carries information about the distribution of the diameter of the fibres. The method has mostly been used on binary images. However, during the conversion from grayscale to binary images, some of the information is lost. For example, the voxels corresponding to the edge of the fibre are either set to the background or to the fibre and this will lead to errors in the estimation of the fibre diameter. It is therefore advantageous to work on grayscale images rather than binary.

Commonly, the thickness of the object is then expressed as the scale for which the pattern spectrum reaches its maximal value. However, different maximum values can be reached at different scales. To take into account this effect, we follow the methodology presented in [15]. The expression also includes a scale parameter to correct the bias induced by the edge effect: the intensity of the voxels at the fibre edges reflects the fact that the edges are a mixture of the fibre and the background. Therefore, they should "count" less in the measure of the thickness. The resulting expression for the thickness of a voxel *p* belonging to *I*, $Th(I)(p)$ is given in eq. (8).

$$Th(I)(p) = 2\frac{\sum I(p)\, PS_{\gamma_n}(p)}{\sum PS_{\gamma_n}(p)} - \frac{M - I(p)}{M - m} \tag{8}$$

with *M* and *m* being the maximum and minimum intensities of the image I respectively.

2.5 Number of fibre contacts and fibre segmentation

When the structure tensor is computed for the orientation estimation, and then the eigenvalues and eigenvectors are calculated, another indicator known as the coherency can be extracted from the maximal and minimal eigenvalues, λ_1 and λ_3. The coherency is a measure of how homogeneous the orientation is in a neighbourhood. For a neighbourhood with a preferential orientation (i.e. along a fibre), the coherency value is close to 1. On the other hand, a neighbourhood without a preferential orientation (i.e. the contact zone where a fibre intersects another fibre) results into a value close to 0 for the coherency. The expression for the coherency at a voxel *p*, $C_t(p)$ is given by:

$$C_t(p) = \left(\frac{\lambda_1(p) - \lambda_3(p)}{\lambda_1(p) + \lambda_3(p)}\right)^2 \tag{9}$$

We compute the coherency for each voxel and threshold the 3D images with this value. The value of the voxels with a coherency value higher than 0.9 is set to zero. As a result, the voxels corresponding to contact zones between fibres with different orientations are removed. We can then proceed to a simple labelling of the fibres based only on the connectivity of the voxels: we consider the 26 neighbours of each voxel and set to the same label all connected voxels. After the thresholding process, the value of the voxels belonging to a fibre where locally the orientation varies abruptly (e.g. fibres extremities) is also set to zero. The last step consists of reconstructing the fibres so that they recover their original shape and volume. We also reconstruct the contact zones and attribute them to the fibres with the lowest label.

2.6 Fibre length

The length of the fibres is extracted from the segmented fibres data: we first calculate the volume of each fibre V_{fib} and then determine the length l knowing the fibre diameter from the local thickness map since we have the following relation:

$$V_{fib} = \int_o^L \pi r^2 dl \tag{10}$$

3. Results and discussion

3.1 Validation using virtual network generation

3.1.1 Virtual network generation

A fibre is modelled as a straight cylinder. Fibres are deposited one by one inside a box. Whenever a fibre intersects with the boundary of the box, the fibre is cut. As the fibre is

deposited on top of the previously generated fibres, there is no overlapping of the fibres. The fibre diameter, length and orientation are controlled by statistical distributions (Poisson distribution for the fibre length and uniform distribution for the fibre diameter and orientation). The orientation angle of the fibres is constrained to the *x-y* plane as we expect the real fibre network to tend to have a planar orientation. A visualisation of the generated virtual fibrous network is given in Figure 1.

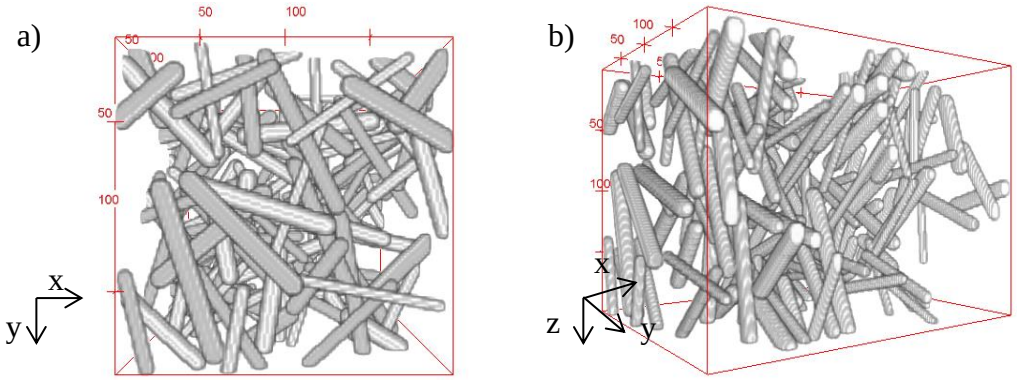

Figure 1. Virtual fibrous network: a) x-y view and b) 3D view

3.1.2 Comparison between input data and data obtained by image analysis

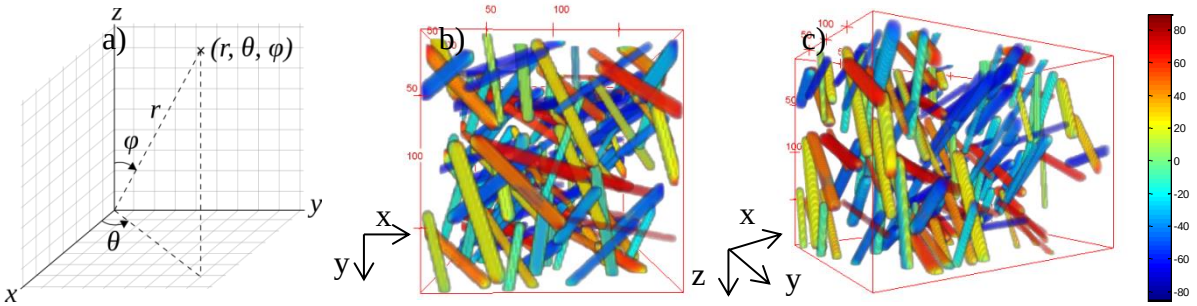

Figure 2. a) Description of the orientation of a point in a 3D space, b) visualization of the fibre orientation of the virtual fibrous network: *x-y* view and c) 3D view (orientation angle in the *x-y* plane is indicated by the colour)

The orientation of a point in 3D can be defined by two angles θ and φ (cf. Figure 2.a). Figures 2.b and 2.c show the estimated orientation of the fibres in the x-y plane (angle θ). We also estimate the orientation angle φ and found as expected a constant value. The graphs of the orientation distribution in the *x-y* plane from Figure 3.a indicate that there is a good correlation between the image analysis measurements and the inputs data from the model. Source of deviation between the real and estimated orientation distribution could be the error in the orientation estimation at the ends of the fibres due to their round shape. We have obtained as well a good agreement between the real and estimated diameter distributions in the virtual fibrous network as presented in the graph of the Figure 3.b.

a) b)

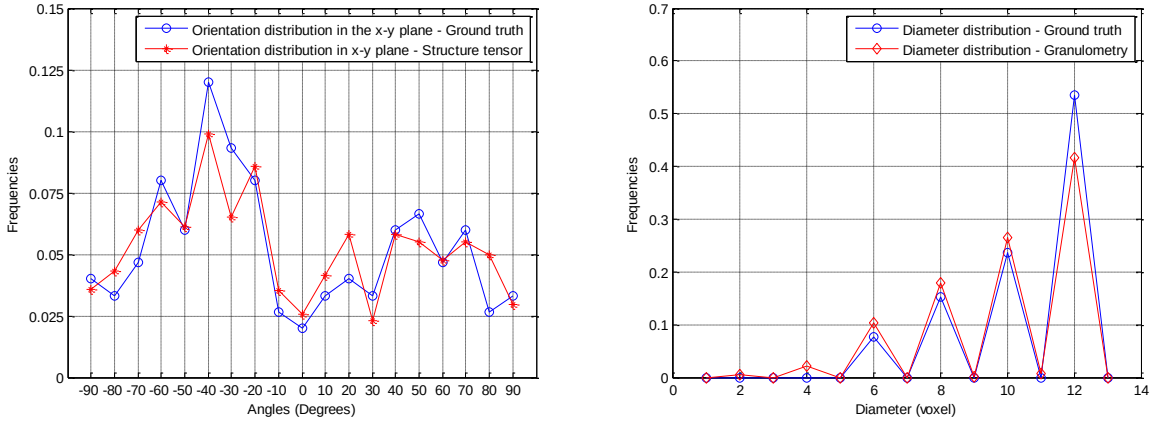

Figure 3. a) Comparison of the real orientation distribution with the estimated orientation distribution and b) of the real diameter distribution with the estimated diameter distribution of the virtual fibrous network.

The contact detection procedure was applied to the virtual fibrous network in order to segment the fibres. Results are shown in Figure 4 where a different colour is randomly allocated to each fibre. Note that that contact zone can be allocated with a different colour than the rest of the fibre. After segmentation, 146 fibres were found instead of 150. The deviation in the results can be attributed to the facts that fibres with similar orientation in contact may not be distinguished (e.g. parallel fibres) and/or that if a fibre has several intersections, it can completely disappear during the thresholding. We could not compare the estimated and input length distribution as fibres are cut during the volume generation process and thus the length is modified automatically.

It is noted that the good correlation between the expected numerical results and the image analysis measurements validate the proposed method for the fibre diameter and orientation as shown in Figure 3. Regarding the contact detection, fibre segmentation and length measurement, the method leads to reasonable results but will be further improved.

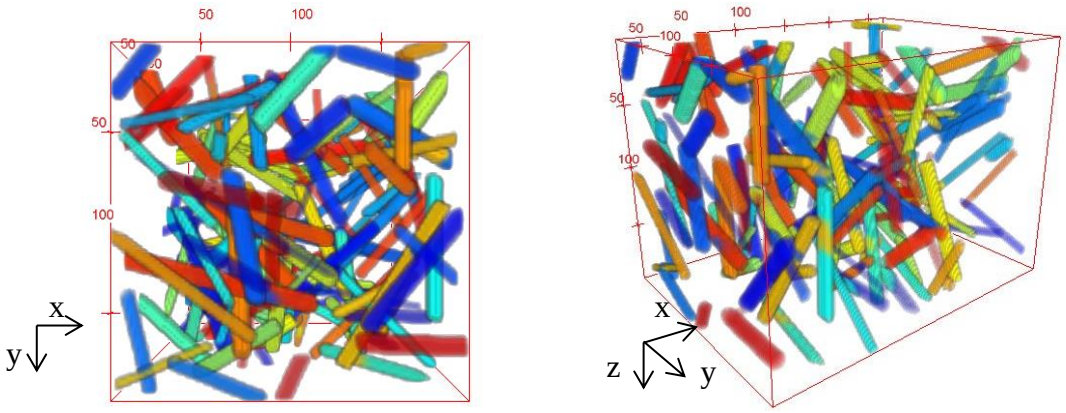

Figure 4. Visualization of the fibre network with random colour allocation for each fibre label

3.2 Real material: stone wool fibre network

In order to reduce the computational effort, only small volumes (400x400x600 voxels) were considered. A visualisation of the volume for the stone wool microstructure is given in Figure

5. The fibres present a wide range of diameters and seem to be oriented quite randomly in the *x-y* plane.

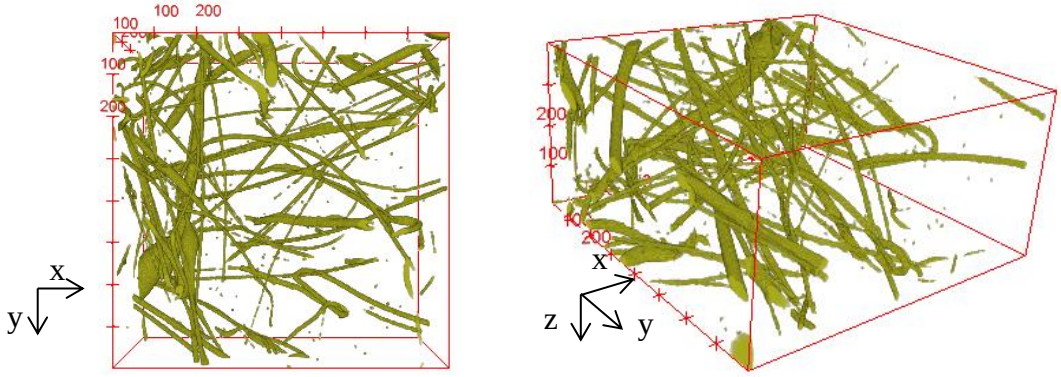

Figure 5. Microstructure of a stone wool sample extracted from a Super flexibatts® product

The results presented in Figure 6.a confirm that the fibres do not show a preferential orientation in the *x-y* plane. Figure 6.b indicates that the orientation φ of the fibres is centred on 40º.

According to the results of Figure 7.2, the fibre radius distribution presents two main peaks centred at 1.4 and 3.3 µm. After segmentation of the fibre network (Figure 7.b), we estimated the number of contacts to be 10 for a total of 121 fibres. We have also estimated the length of each fibre (Figure 7.c), however as the volume considered is really small compared to the length of the fibres, we are only measuring the lengths of fibre segments.

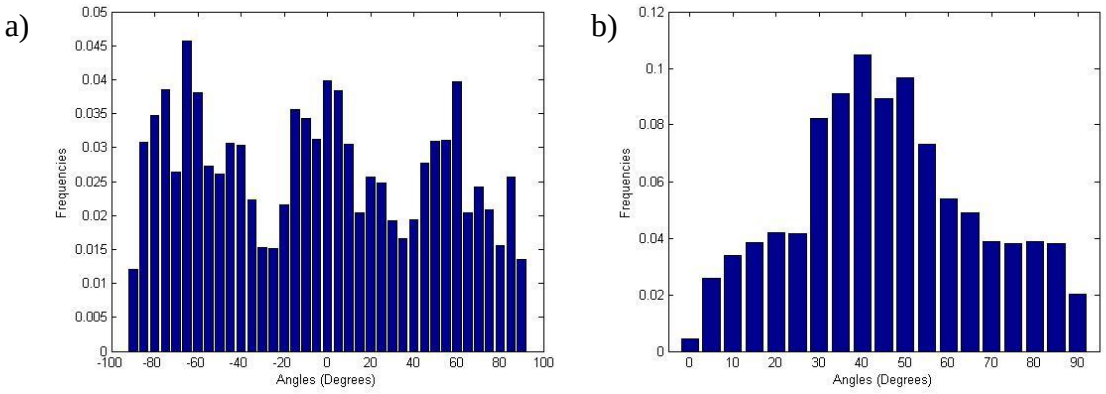

Figure 6. a) Orientation distribution described by the angle θ (*x-y* plane) and b) by the angle φ of a sample taken from a Super Flexibatts®

a) b) c)

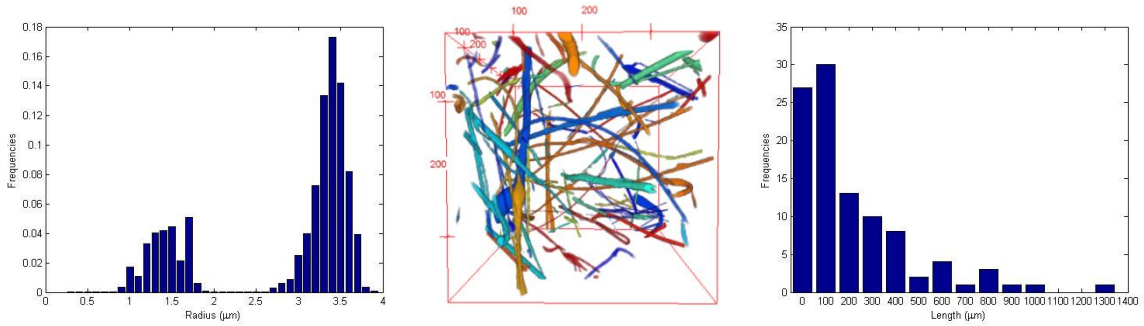

Figure 7. a) Fibre radius distribution and b) fibre segmentation of a sample taken from a Super Flexibatts®

The methods developed in this study have proven to be suitable for the characterization of stone wool microstructure. In order to extract information representative of the material, further studies will be conducted working on larger volume. Fibres are not the only components of stone wool. It also contains shots which are droplets of solidified melt inherent to the fiberization process, and binder. To fully characterize the microstructure of the stone wool product, methods to quantify the binder and the shots distribution are being developed.

4. Conclusion

In this work, we propose methods for characterization of complex fibre networks, such as stone wool, based on image analysis of 3D datasets obtained by x-ray tomography. Estimation of the orientation and diameter of the fibre does not require for preliminary segmentation of the fibres. However, to determine the number of contact points as well as the length of the fibres, we need to first be able to distinguish each fibre. Methods have been validated using a virtual fibrous network. Once full characterization is achieved, a virtual fibrous network using the real material inputs can be created. An analysis should then be performed in order to determine the minimal achievable size for the volume to be statistically representative of a stone wool product. Finally using this volume as an input in a finite-element analysis, mechanical properties of stone wool will be predicted.

References

[1] F. M. B. Andersen and S. Dyrbøl. Modelling radiative heat transfer in fibrous materials: the use of Planck mean properties compared to spectral and flux-weighted properties. *Journal of Quantitative Spectroscopy and Radiative Transfer*, 60(4):593-603, 1998.

[2] J. Lux, A. Ahmadi, C. Gobbé and C. Delisée. Macroscopic thermal properties of real fibrous materials: Volume averaging method and 3D image analysis, *International Journal of Heat and Mass Transfer*, 29:1958-1973, 2006

[3] C. Peyrega and D. Jeulin. Estimation of acoustic properties and of the representative volume element of random fibrous media, *Journal of Applied Physics*, 113(10):-

[4] C. Jensen and R. Raspet. Thermoacoustic properties of fibrous materials, *Journal of Acoutic Society of America*, 127(6):3470-3484, 2010

[5] J. Lux, C. Delisée and X. Thibault. 3D characterization of wood based fibrous materials: an application, *Image Analysis & Stereology*, 25:25-35, 2006

[6] M. Krause, J. M. Hausherr, B. Burgeth, C. Hermann and W. Krenkel. Determination of the fibre orientation in composites using the structure tensor and local X-ray transform, *Journal of Material Science*, 45:888-896, 2010

[7] H. Altendorf and D. Jeulin. 3D directional mathematical morphology for analysis of fiber orientation, *Image Analysis and Stereology*, 28(3):143-153, 2009
[8] A. Miettinen, C. L. Luengo-Hendriks, G. Chinga-Carrasco, E. K. Gamstedt and M. Kataja. A non-destructive X-ray microtomography approach for measuring fibre length in short-fibre composites, *Composites Science and Technology*,72:1901-1908, 2012
[9] F. Hild, E. Maire, S. Roux and J. F. Witz, Three-dimensional analysis of a compression test on stone wool, *Acta Materialia*, 67(11):3310-3320, 2009
[10] J. P. Masse, L. Salvo, D. Rodney, Y. Bréchet and O. Bouasziz. Influence of relative density on the architecture, and mechanical behaviour of steel metallic wool, *Scripta Materialia*, 54(7):1379-1383, 2006
[11] J. C. Tan, J. A. Elliott and T.W. Clyne. Analysis of tomography images of bonded fibre network to measure distributions of fibre segment length and fibre orientation, *Advanced Engineering Materials*, 8(6):495-500, 2006
[12] H. Yang and B. W. Lindquist, Three-dimensional image analysis of fibrous materials, Proceedings *SPIE 4115*, Applications of Digital Image Processing XXIII, 275, pages 275-282
[13] J. Viguié, P. Latil, L. Orgéas, P. J. J. Dumont, S. Rolland du Roscoat, J.-F. Bloch, C. Marulier and O. Guiraud, Finding fibres and their contacts within 3D images of disordered fibrous media, *Composites Science and Technology*, 89:202-210, 2013
[14] J. Bigun and G. Granlund, Optimal orientation detection of linear symmetry. In *IEEE First International Conference on Computer Vision*, pages 433-438, 1987.
[15] R. Moreno, M. Borga and O. Smedby. Estimation of trabecular thickness in gray-scale through granulometric analysis. In *Conference on Medical Imaging – Image processing*, 8314, 2012

[P2]: Generation of non-overlapping fiber architecture

GENERATION OF NON-OVERLAPPING FIBER ARCHITECTURE

L. Chapelle[1,2], M. Lévesque[3], P. Brøndsted[2], M. R. Foldschack[1], Y. Kusano[2]

[1]Group Development, ROCKWOOL International A/S,
Hovedgaden 584, DK-2640 Hedehusene, Denmark
E-mail: lucie.chapelle@rockwool.com, web page: http://rockwool.com
Email: mathilde.foldschack@rockwool.com, web page: http://rockwool.com

[2]Department of Wind Energy, Technical University of Denmark
P.O. Box 49, Frederiksborgvej 399, DK-4000 Roskilde, Denmark
Email: pobr@dtu.dk, web page: http://www.dtu.dk

[3]Laboratory for Multiscale Mechanics (LM2), CREPEC, Département of Mechanical Engineering, École Polytechnique de Montréal, C.P. 6079, succ. Centre-ville, Montréal, QC, H3C3A7, Canada Email: martin.levesque@polymtl.ca, web page: http://www.polymtl.ca/lm2

Keywords: Random periodic packing, Curved fibers, Fiber orientation

ABSTRACT

Numerical models generating actual fiber architecture by including parameters such as the fiber geometry and arrangement are a powerful tool to explore the relation between the fiber architecture and mechanical properties. The generation of virtual architectures of fibrous materials is the first step toward the computation of their physical properties. In this work, a realistic 3D model is developed to describe the architecture of a complex fiber structure. The domain of application of the model could include natural fibers composites, wood fibers materials, papers, mineral and steel wools and polymer networks. The model takes into account the complex geometry of the fiber arrangement in which a fiber can be modeled with a certain degree of bending while keeping a main fiber orientation. The model is built in two steps. First, fibers are generated as a chain of overlapping spheres or as a chain of overlapping sphero-cylinders. At the end of the first step, a system of overlapping fibers is obtained. In order to obtain a hard-core configuration where fibers cannot overlap other fibers, we use an iterative method called the force-biased algorithm. It applies virtual forces on each point of the fiber: a repulsion force to suppress the overlap between two fibers and a bending and stretching force to ensure that the fiber structure is kept unchanged. The model can be used as the geometrical basis for further finite-element modelling.

1 INTRODUCTION

The generation of a packing of objects in a space can either be designated as a soft-core or hard-core process. In a soft-core model, the overlap of the packed object is allowed which is not realistic from a physical point of view. However the simplicity of implementation of those processes has made it a quite popular tool for the microstructure generation of complex materials. One of the first soft-core processes generating a packing of fibers was introduced by Matheron [50]. It made use of dilated Poisson lines to create straight infinite cylinders [50]. Later, lines were generated by a Poisson process in [36,47,51,52] to model respectively the microstructure of a nonwoven material, the gas diffusion layer of proton exchange membrane fuel cells and the fiber structure of thermal and acoustic materials. Soft-core models were developed further to consider fibers with a more complex geometry. For example, to model curved fiber system, several soft-core processes include bending of the fibers through random walks whose direction are controlled by von Mises-Fischer distribution

[54,55]. Others have introduced bending of the fibers by interpolating points with B-splines [56,57].
The random sequential adsorption (RSA) model is probably the most commonly used method to construct hard-core systems because its principle is relatively simple even though its implementation can be a bit tricky for objects with a complex geometry. The RSA scheme iteratively generates objects and tries to place them in such a way that they do not intersect. Initially created for the packing of spheres, the process was then applied on cylinders by Feder [58]. Bezrukov and Stoyan proposed an algorithm for the generation of random packing of ellipsoids of revolution [68]. Contacts between ellipsoids are detected and a force biased algorithm is applied to translate and rotate the particles that overlap. Both approaches achieve relatively low volume fraction (10 – 15 % for isotropic orientation with a fiber aspect ratio of 10). Recently, Naddeo et al. used an RSA based microstructure generation method with fibers shaped as cylinders but very little details on the overlap detection was provided [59]. On the other hand, in [60], the implementation of the contact detection of two cylinders is given. The problem of the RSA based method is that for fibers with an isotropic orientation distribution and high aspect ratio, only low volume fractions can be achieved as a jamming limit is reached when no new positions can be found. Modifications of the RSA algorithm can be made so that when a fiber position is rejected because it overlaps another fiber with a certain distance, a translation of this distance is applied to the fiber. Using this algorithm, microstructures with volume fractions up to 38 and 29% and randomly oriented fibers with aspect ratios of 10 and 30, respectively, were generated [61].

Another type of model based on the deposition of straight fibers can achieve hard-core configurations [62]. In that model, fibers are deposited in an iterative manner from the top of the cell and whenever they enter in contact with another fiber, they stop their falls. This approach gives high fiber volume fraction, but the fiber orientation is limited to the plane. The deposition technique is widely used for paper-like materials where the assumption of an in-plane fiber orientation distribution is quite realistic [63–65]. The fiber bending model was also included in [66]. When an overlap is detected, fibers are bent to accommodate the intersection with other fibers. Straight fibers are modelled as convex prism with two dodecagon end-faces while several convex irregular polyhedral are used in case of curved fibers. Wang et al. modeled non-woven fiber-webs by a similar deposition algorithm where the orientation was limited to a plane [67].
Some other hard-core models took inspiration in molecular dynamics simulations. For example, Ghossein et al. used an event-driven molecular dynamics algorithm to generate spheres and ellipsoids with a very high aspect ratio (i.e.>10) in a hard-core packing configuration [69,102]. Recently, Altendorf et al. presented a model combining some of the ideas discussed previously [46]. Firstly, bended fibers are modelled as ball chains by a random walk [103]. Secondly, similar to Wirjadi [54] and Karkkainen et al. [55] the orientation distribution can be controlled in spite of the bending. Thirdly, the force-biased approach is applied for sphere packing [71] and [68] and fourthly, the design of energies in molecular dynamics is used to define the forces [71]. It produces a random hard-core fiber model with a controllable bending and high volume fraction. The level of bending is controlled by two parameters in the multivariate von Mises Fisher distribution. As mentioned earlier, the fibers are represented as chains of spheres with defined centers and radii. The spheres are connected through random walk paths. This first step gives a soft-core system of bending fibers. To produce a hard-core configuration, a force biased approach is used. Two kinds of forces are applied to the sphere centers: repulsion and recover forces. The repulsion force prevents the overlap of fibers and the recover force maintains the sphere chain structure.

Gaiselmann et al. also represented the fibers by a chain of spheres but generated the fibers midpoints with a Poisson point process and the fibers by random 3D polygonal tracks [72]. The overlap of the fibers was suppressed using a force-biased algorithm as well [71].

In the present work, a modified version of the algorithm from Altendorf et al. [46] is implemented. The modification includes the use of a chain of sphero-cylinders for the fiber model, the possibility of modeling the fiber bending using spline interpolation and the introduction of more realistic forces for the transformation into a non-overlapping fiber network.

2 GENERATION OF A SOFT-CORE FIBERS NETWORK

2.1 Fiber model

2.1.1 Chain of spheres

The first model studied in this work is the one adopted from [46,104] where a fiber is modelled as a chain of overlapping spheres. The coordinates of the first sphere center of the chain are generated according to a uniform law in the intervals $[0 - x_{max}]$, $[0 - y_{max}]$ and $[0 - z_{max}]$ where x_{max}, y_{max} and z_{max} are the length of the sides of the observation cell chosen for the generation. The coordinates of a point $i \in \mathbb{N}\backslash\{0\}$ representing the center of a sphere belonging to the fiber are generated iteratively from the coordinates of their previous neighbor x_{i-1}:

$$x_i = x_{i-1} + \mu_i \cdot \frac{r_i}{2} \tag{1}$$

r_i and μ_i are respectively the fiber radius and the direction of the fiber at the point i.
A realization of a fiber is shown in the figure below (Fig. 1).

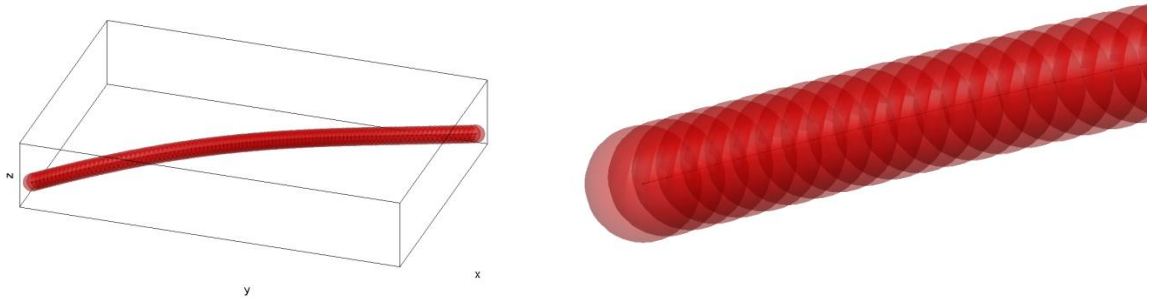

Figure 1: Fiber modelled as a chain of spheres.

2.1.2 Chain of sphero-cylinder

A new discretization is proposed here where the fiber is modelled as a chain of overlapping sphero-cylinders. The generation process is similar to the one proposed in section 2.1.1. The only difference is the length of the step between two points. The first spherical part of the sphero-cylinder overlaps with the spherical part of the previous sphero-cylinder. If μ_i designates the direction, l_i the height of the cylinder part and x_{i-1} the position of its previous neighbour, then the position of the point i is:

$$x_i = x_{i-1} + \mu_i \cdot l_i \tag{2}$$

The geometry of the sphero-cylinder and a fiber modelled by a walk of points obtained using the sphero-cylinder model are represented in the figure below (Fig. 2).

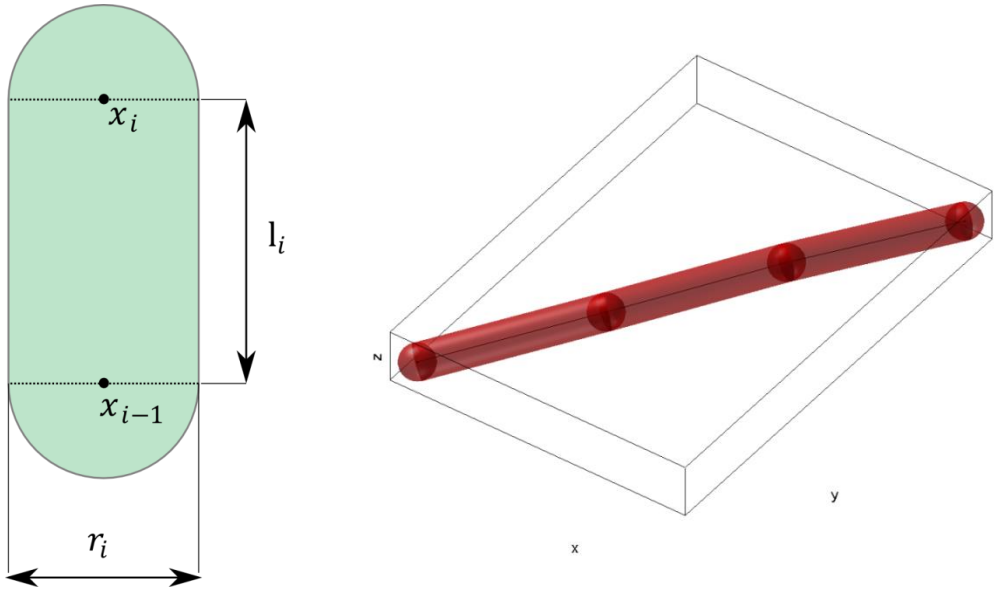

Figure 2: Fiber modelled as a chain of sphero-cylinders.

2.2 Models for the fiber orientation

2.2.1 Main fiber orientation

The distribution proposed in [47] was chosen to define the orientation of the fibers. The density associated to this distribution is a function $p_\beta(\theta, \varphi)$ of elevation $\theta \in [0, \pi)$ and azimuth $\varphi \in [0, \pi)$:

$$p_\beta(\theta, \varphi) = \frac{1}{4\pi} \frac{\beta \sin\theta}{(1 + (\beta^2 - 1)\cos\theta)^{3/2}} \tag{3}$$

$\beta \in \mathbb{R}+\backslash\{0\}$ is the anisotropy parameter. We can notice that the distribution is independent from φ.The angles definition and a plot of the probability density function for two values of β is given in Fig. 3. The case $\beta = 1$ describes an isotropic fiber system and results in the uniform distribution on the sphere. For increasing β the fibers tend to be more and more parallel to the xy-plane. For $\beta \to 0$, the distribution concentrates around the z-axis.

To sample directions selected from the distribution, the inverse cumulative distribution $G(\theta)$ is needed. Indeed, if u is a uniform variable on [0,1], then $G^{-1}(u)$ follows the distribution given by G.

The cumulative distribution $G(\theta)$ is given by:

$$G(\theta) = \frac{1}{2} - \frac{\beta}{2\sqrt{\cos^{-2}\theta + (\beta^2 - 1)}} \tag{4}$$

And the inverse of $G(\theta)$ is:

$$G^{-1}(x) = \cos^{-1}\left(\frac{x}{\sqrt{x^2 - \beta x^2 + \beta^2}}\right) \tag{5}$$

The following procedure is applied:

- x_1 and x_2 are sampled from a uniform distribution in $(0,1)$
- Find θ such that $x_1 = G(\theta)$: $\theta = G^{-1}(x_1)$
- Find φ such that $x_2 = F(\varphi)$: $\varphi = 2\pi x_2$

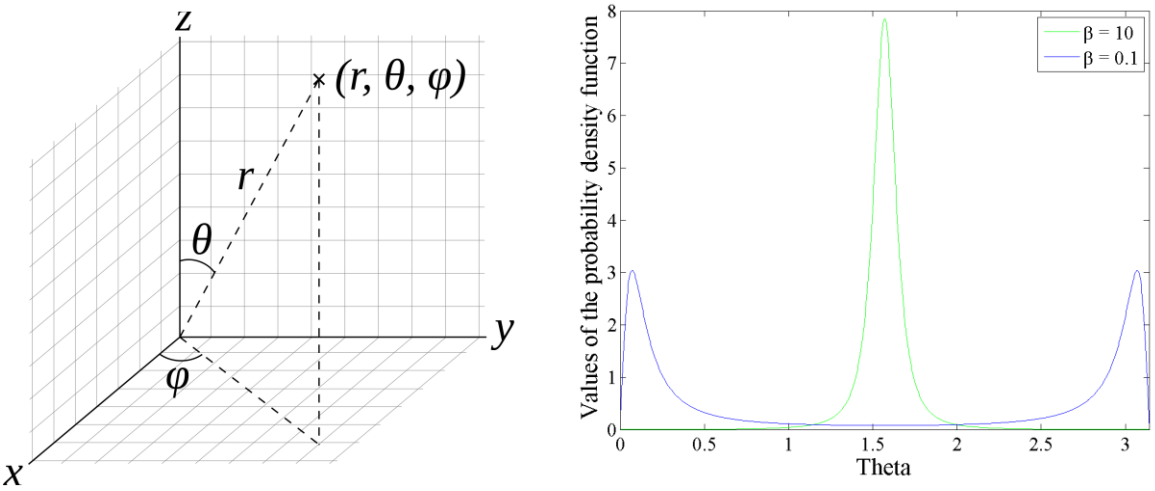

Figure.3: Angle definition and probability density function for the β distribution with $\beta = 10$ and $\beta = 0.1$.

Figure 4 shows different realization of an overlapping fiber network with different values of β.

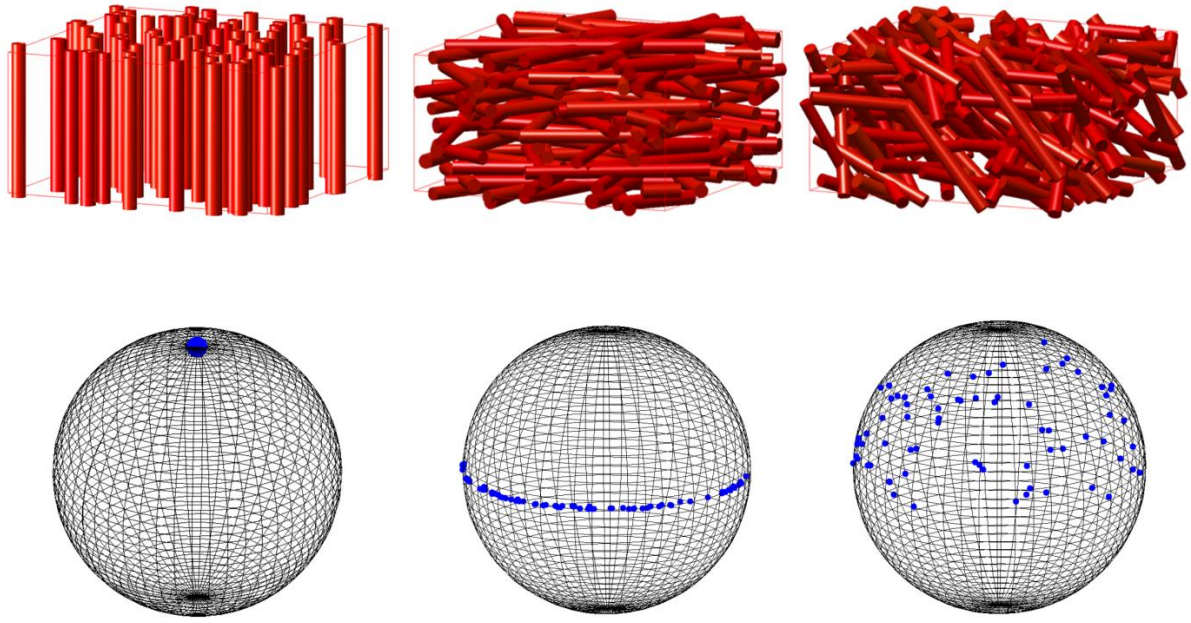

Figure.4: Top: Realization with $\beta = 0$ (left), $\beta = 100$ (middle) and $\beta = 1$ (right). Bottom: corresponding directions on the unit sphere.

2.2.2 Fiber bending using von-Mises Fischer distribution

The von-Mises Fischer (vMF) distribution is a well-known distribution used to describe the orientation of objects with a preferred direction and a reliability parameter. The probability density element of a vMF distribution for a vector u with a preferred direction vector μ and a reliability parameter κ is:

$$f(u|\mu,\kappa) = \frac{\kappa}{2\pi(e^{\kappa} - e^{-\kappa})} e^{\kappa\mu^T u} \tag{6}$$

We present in table 1 the algorithm for sampling a vector from a vMF distribution. Details of the implementation can be found in [105,106].

Kärkkainen et al. and later Altendorf and Jeulin have extended the univariate von Mises-Fischer distribution to a multivariate one in order to make use of two preferred directions and two reliability parameters [46,55]. One of the preferred directions is the main fiber orientation while the other is set to be the direction of the previous element of the fiber.

The probability density function of a bivariate von Mises-Fischer distribution for a sampled direction $\mathbf{u}$ with preferred directions $\boldsymbol{\mu_1}$ and $\boldsymbol{\mu_2}$ and corresponding reliability parameters , $\boldsymbol{\kappa_1}$ and $\boldsymbol{\kappa_2}$ is:

$$f(u|\mu_1,\kappa_1,\mu_2,\kappa_2) = \frac{|\kappa_1\mu_1+\kappa_2\mu_2|}{2\pi(e^{|\kappa_1\mu_1+\kappa_2\mu_2|}-e^{-|\kappa_1\mu_1+\kappa_2\mu_2|})}\, e^{(\kappa_1{\mu_1}^T u+\kappa_2{\mu_2}^T u)^T u} \tag{7}$$

To generate random directions following a bivariate von Mises-Fischer distribution, we use the same algorithm as presented before as the bivariate function can be written as a classical von Mises-Fischer distribution by setting:

$$\kappa = |\kappa_1\mu_1+\kappa_2\mu_2| \text{ and } \mu = \frac{\kappa_1\mu_1+\kappa_2\mu_2}{\kappa} \tag{8}$$

Table 6: Sampling a vector from a vMF distribution

Algorithm 1
Define a vector w_k with mean direction $\mu = (0,0,1)^T$ distributed according to a vMF distribution
$w_k = (\sqrt{1-W^2V}, W)^T$ where V and W are independent random variables, $V \in \mathbb{R}^2$ is a uniformly distributed vector on the unit circle, and $W \in [-1;1]$ follow the density: $f(v|\kappa) = \frac{\kappa}{(e^{\kappa}-e^{-\kappa})} e^{\kappa v}$
Compute the cumulative function of f: $F(x) = \frac{\kappa}{(e^{\kappa}-e^{-\kappa})}\left(\frac{1}{\kappa}e^{\kappa x} - \frac{1}{\kappa}e^{-\kappa}\right)$
Compute the inverse of F: $F^{-1}(y) = \frac{1}{\kappa}\log\left(e^{-\kappa} + \kappa\frac{e^{\kappa}-e^{-\kappa}}{\kappa}y\right)$
Draw a scalar y from a uniform distribution in the interval (0,1)
Compute W: $F^{-1}(y) = W$
Draw a variable V from a uniform distribution on the unit circle
Compute $w_k = (\sqrt{1-W^2V}, W)^T$
Apply a rotation matrix to generate a vector with a mean direction other than $(0,0,1)^T$

2.2.3 Bending introduced by splines

In this approach, a line is generated in 3D using the orientation distribution defined in 2.2.1 and curvature points are added around this line by adding a deviation parameter to points belonging to the line.

$$p_{2i} = p_{1i} + \Delta s = \begin{pmatrix} x_{1i} \\ y_{1i} \\ z_{1i} \end{pmatrix} + \begin{pmatrix} \Delta s_x \\ \Delta s_y \\ \Delta s_z \end{pmatrix} \tag{9}$$

The points are then used as control points to generate a cubic spline. The degree of curvature and tortuosity of a fiber can be controlled by adjusting the number of points that deviates from the line and the deviation parameter, $\Delta\mathbf{s}$.

2.3 Generation of a system with overlapping fibers

A system with overlapping fibers is created using either the chain of spheres or chain of sphero-cylinders approach. The bending and orientation of the chain is described by the distribution described in section 2.2. The algorithm for the generation of a system of overlapping fibers is given in table 2.

Table 7: Generation of a system of overlapping fibers

Algorithm 2:
Ask for inputs for the fiber main orientation (β), the fibre bending ($\kappa_1, \mu_1, \kappa_2, \mu_2$ or Δs), the fibre aspect ratio, the fiber volume fraction (V_f) and the size of the cell
Initialize variables (current volume V, array containing the future fibre data points)
WHILE $\|V - V_f\| \leq$ small number
WHILE $\|$desired aspect ratio $-$ current aspect ratio$\| \leq$ small number
$$x_i = x_{i-1} + \mu_i \cdot l_i$$
END WHILE
IF points exits through a face
Create a periodic images
Delete element completely outside of the cell
END IF
END WHILE

At the end of this step, a periodic system with overlapping fibers is obtained with controlled orientation, bending and aspect ratio of the fibers.

3 GENERATION OF A HARD-CORE FIBRE NETWORK

To transform the overlapping system of fibers into a hard-core one, we use the force-biased algorithm first introduced by Moscinski et al. for the packing of hard spheres [71]. Virtual forces are applied on overlapping spheres until the overlap is completely prevented. Later, Altendorf and Jeulin extended the force-biased algorithm to fiber structure and added two additional forces that ensure that the fiber stretching and bending is constrained as well [46]. In this work, the expressions for the forces are expressed as a function of the material properties. The forces are applied by small increment until the total energy of the system reaches a minimum threshold level.

3.1 Repulsion forces

The force needed to repulse two objects overlapping is inspired from the Hertz contact between two hard surfaces where the overlap is treated as the deformation.

$$F_{repulsion} = K_r \left(\frac{r_1 r_2}{r_1 + r_2} \right) \delta^{3/2} \tag{10}$$

The algorithm for the implementation of the repulsion force is presented in table 3.

Table 8: Repulsion force for two spheres or sphero-cylinders that overlaps

Algorithm 3
Compute distance between the two centers or minimal distance between the axis of the sphero-cylinders $d_{i,j}$
Calculate the overlap: $\delta = \max(0, r_i + r_j - d_{i,j})$
Calculate the force and potential
IF $d_{i,j} = 0$
Create a unit random direction vector $u = 2 \cdot \text{rand}(3,1) - 1$

$F_{repulsion} = K_r \left(\frac{r_1 r_2}{r_1 + r_2}\right) \delta^{3/2} u$

ELSE

$$F_{repulsion} = K_r \left(\frac{r_1 r_2}{r_1 + r_2}\right) \delta^{\frac{3}{2}} \cdot \left(\frac{x_j - x_i}{\|x_j - x_i\|}\right)$$

END IF

For a fast implementation of the repulsion force, the search of candidate points that are susceptible to overlap is optimized by using a near neighbor list [107]. The cell containing the fibers is divided into smaller sub-cells. The neighbors of a point are searched in the cell where the point belongs as well as the adjacent cells.

3.2 Bending and tension forces

To ensure that the fiber keeps its structure while being under the action of the repulsion forces, two forces are introduced that constraint the relative motion of the elements of the fibers. The first one is limiting the stretching of the fiber axis. It acts like a spring with a constant K_S and is a function of the elongation:

$$F_{stretching} = \frac{K_S}{l_0}\left(\frac{l_i - l_0}{l_0}\right) \tag{11}$$

where l_0 is the intial distance between two elements (spheres or sphero-cylinders) and l_i is the current distance after the application of forces. The forces are applied at the centers of the spherical parts of the sphero-cylinder or at the centers of the spheres depending on the elements chosen for the discretization of the fiber.

Under tensile load, the strain and the stress can be expressed as:

$$\varepsilon = \frac{l_0 - l_i}{l_0} \text{ and } \sigma = \frac{F}{S} = \frac{K_S}{l_0 \pi r^2}\left(\frac{l_i - l_0}{l_0}\right) \tag{12}$$

By analogy with Hooke´s law, we identify the spring constant K_S as:

$$K_S = E_F l_0 \pi r^2 \tag{13}$$

The bending of the three consecutives elements of a fiber is also constrained by another force acting like a torsional spring with a constant K_B:

$$F_{bending} = K_B(\theta_i - \theta_0) \tag{14}$$

where θ_0 the intial angles between three consectutives points and θ_i the current angle. A simple system with three consecitive points (i, j, k) that can be either the centers of overlapping spheres or the centers of the spherical parts of the sphero-cylinders is displayed in the figure below (Fig. 5).

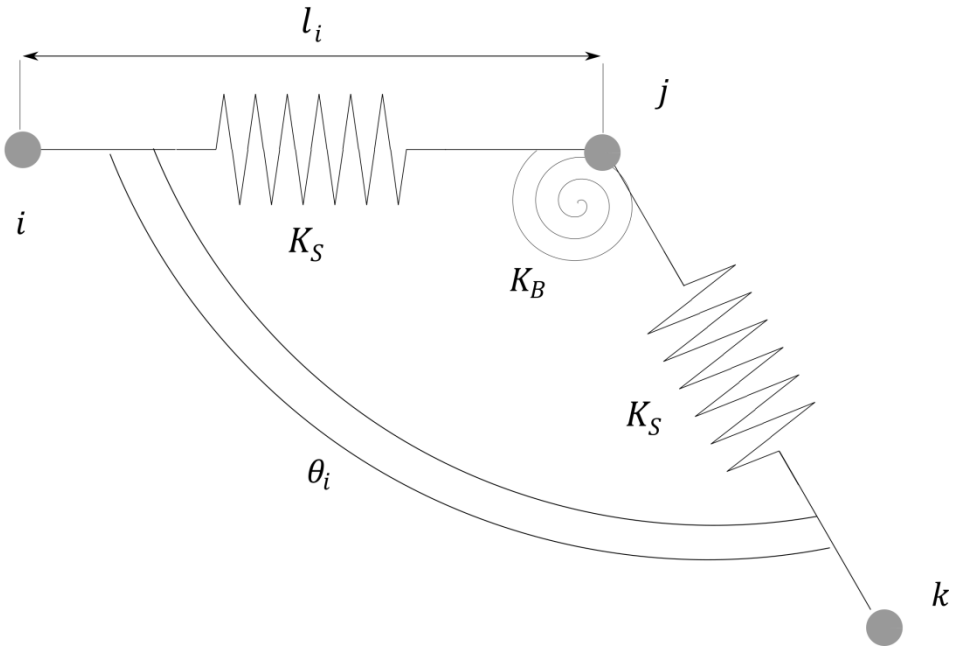

Figure 5: Representation of the system considered for the application of the forces.

We also seek to express the constant K_B as a material parameter. Consider a fiber discretized in N elements (spheres or sphero-cylinders) clamped in one end and loaded with a force F in the other end. Assuming that the work in tension/compression is negligible, we show that the potential energy E is:

$$E = \sum_{i=1}^{N-2} \left(\frac{1}{2} K_B (\theta_i - \pi)^2 \right) - F\delta \tag{15}$$

where δ is the deflection (Fig. 6).

We assume small strains and expressed the deflection as the sum of the displacement as a function of the current angles θ_i:

$$\frac{x_i}{l_0} = \sin(\pi - \theta_i) \approx \pi - \theta_i \Rightarrow \frac{\delta}{l_0} = \sum_{i=1}^{N-2} (N - i - 1)\,(\pi - \theta_i) \tag{16}$$

The beam is in equilibrium when the energy reaches a minimal value. Thus we derive the energy and solve θ_i for the equation $\frac{\partial E}{\partial \theta_i} = 0$

$$\begin{aligned} \frac{\partial E}{\partial \theta_i} = K_B(\theta_i - \pi) + Fl_0(N - i - 1) = 0 \Leftrightarrow \pi - \theta_i \\ = \frac{Fl_0}{K_B}(N - i - 1) \end{aligned} \tag{17}$$

Replacing $(\theta_0 - \theta_i)$ in equ. (13) and using the expression of the sum of squares:

$$\frac{\delta}{l_0} = \sum_{i=1}^{N-2} \frac{Fl_0}{K_B} \cdot (N-i-1)\,(N-i-1) = \frac{Fl_0}{6K_B}(N-2)(N-1)(2N-3) \tag{18}$$

Normalizing with the diameter D of the fibre:

$$\frac{\delta}{D} = \frac{F}{3}\left(\frac{L}{D}\right)^3 \cdot \left(\frac{D^2}{K_B l_0}\right)\left(1-\frac{l_0}{L}\right)\left(1-\frac{l_0}{2L}\right) \tag{19}$$

By analogy with the beam theory, we obtain an expression for the bending constant depending on material parameters:

$$\frac{\delta}{D} = \frac{FD^2}{3E_f I}\left(\frac{L}{D}\right)^3 = \frac{F}{3}\left(\frac{L}{D}\right)^3 \cdot \left(\frac{D^2}{K_B l_0}\right)\left(1-\frac{l_0}{L}\right)\left(1-\frac{l_0}{2L}\right) \Leftrightarrow K_B = \frac{E_f I}{l_0}\left(1-\frac{l_0}{L}\right)\left(1-\frac{l_0}{2L}\right) \tag{20}$$

And if the length of the elements is negligible compared to the length of the fiber, we obtain:

$$K_B \approx \frac{E_f I}{l_0} \tag{21}$$

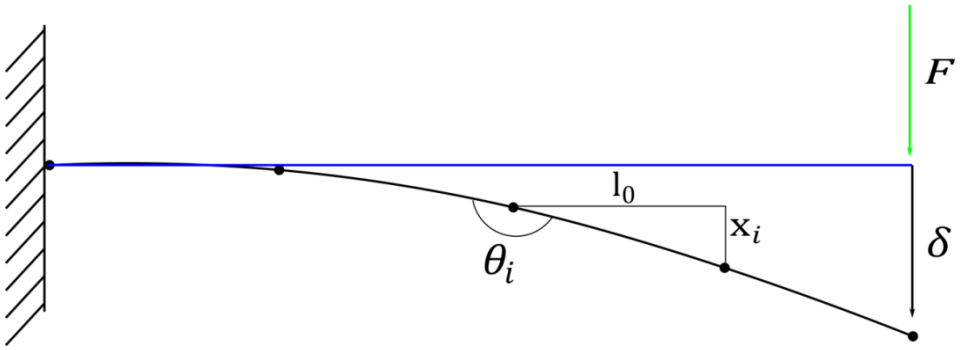

Figure.6: Bending of a discretized fiber.

3.4 Examples of hard-core fibers network

Figure 7 shows the realization of two hard-core fibers networks. Their main characteristics are defined in table 4. We control the fiber radius distribution by drawing the values from a lognormal law. By adjusting the value of the scale parameter σ of the lognormal law, the spread of the distribution can be tuned. Based on the radius and the aspect ratio we calculate the total length of the fiber and the number of discretization points for the fiber model.

Table 9: Parameter for fibers network generation

	Fiber model	Fiber volume fraction	Aspect ratio	Main fiber orientation (β)	Bending
A	Sphero-cylinders	10 %	50	50	mvMF ($\kappa_1 = 5$ and $\kappa_2 = 500$)
B	Spheres	10 %	50	50	mvMF ($\kappa_1 = 5$ and $\kappa_2 = 500$)
C	Sphero-cylinders	10 %	50	50	splines
D	Spheres	10 %	50	50	splines

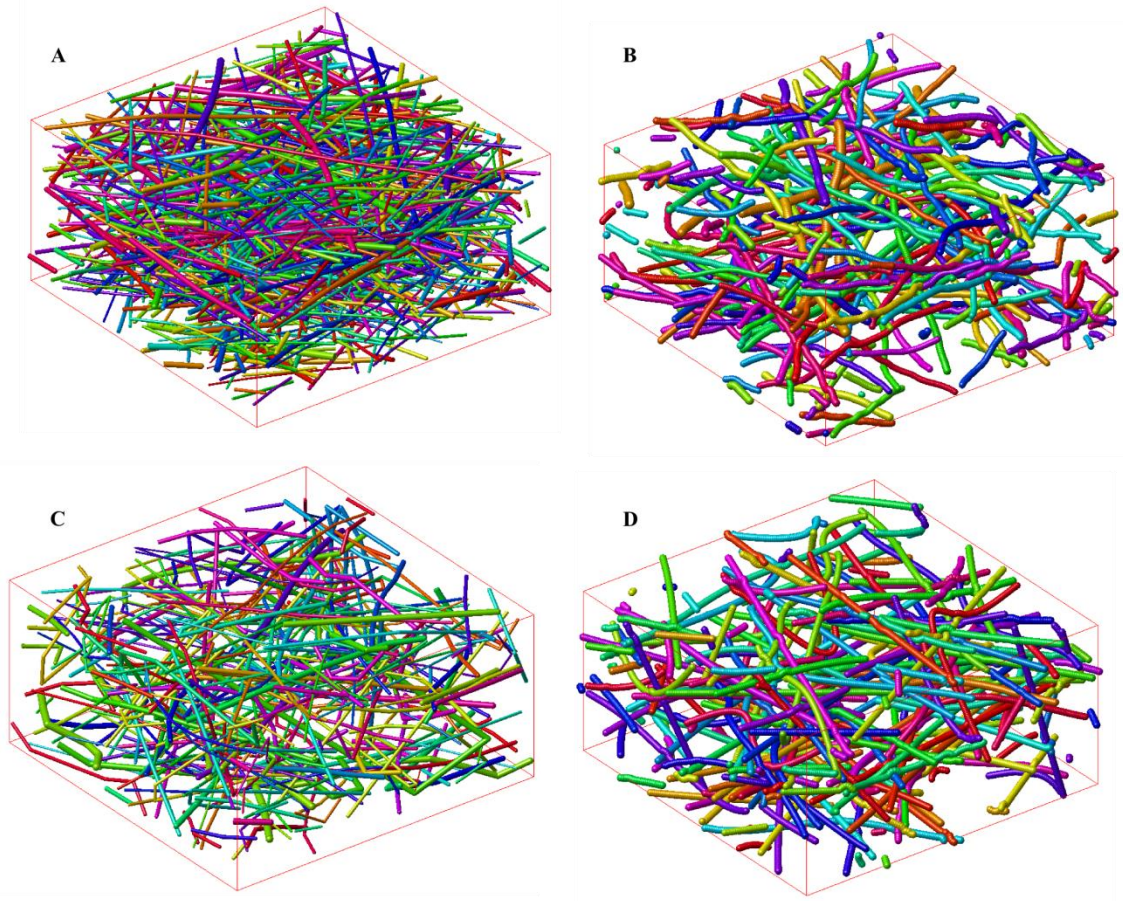

Figure 7: Realization of hard-core fibers systems.

4 DISCUSSION & CONCLUSION

We present here a modification of the algorithm originally proposed by Altendorf and Jeulin for the generation of a system of hard-core fibers [46]. In the modified algorithm, the fiber is modeled as a chain of sphero-cylinders rather than a chain of spheres. This implementation reduces the computational effort for the transformation of the overlapping system into a non-overlapping one as fewer points are considered when applying the forces. The bending of the fibers can be controlled using either a multivariate von Mises-Fischer distribution or a cubic b-spline interpolation. A near-neighbor list is built to determine which points are susceptible to overlap. This increases significantly the speed of the algorithm. The forces applied during the transformation of the system into a non-overlapping one are expressed as a function of material parameters and geometry.

REFERENCES

[1] G. Matheron, Random Sets and Integral Geometry, Wiley, New York, 1975.
[2] C. Peyrega, D. Jeulin, C. Delisée, J. Lux, Image Anal. Stereol. 28 (2009) 129.
[3] Schladitz, Katja, Peters Stefanie, Reinel-Bitzer Doris, Wiegmann, Andreas, J. Ohser, Comput. Mater. Sci. 38 (2006) 56.
[4] J. Dirrenberger, S. Forest, D. Jeulin, Int. J. Solids Struct. 51 (2014) 359.

[5] R. Thiedmann, F. Fleischer, C. Hartnig, W. Lehnert, V. Schmidt, J. Electrochem. Soc. 155 (2008) B391.
[6] O. Wirjadi, Models and Algorithms for Image-Based Analysis of Microstructures, Kaiserslautern University, 2009.
[7] S. Kärkkäinen, A. Miettinen, T. Turpeinen, J. Nyblom, P. Pötschke, J. Timonen, Image Anal. Stereol. 31 (2012) 17.
[8] M. Faessel, C. Delisée, F. Bos, P. Castéra, Compos. Sci. Technol. 65 (2005) 1931.
[9] D. Durville, J. Mater. Sci. 40 (2005) 5941.
[10] J. Feder, J. Theor. Biol. 87 (1980) 237.
[11] A. Bezrukov, D. Stoyan, Part. Part. Syst. Charact. 23 (2006) 388.
[12] F. Naddeo, N. Cappetti, A. Naddeo, Comput. Mater. Sci. 81 (2014) 239.
[13] Y. Pan, Stiffness and Progressive Damage Analysis on Random Chopped Fiber Composite Using FEM, Rutgers, The State University of New Jersey, 2010.
[14] H. Moussady, A New Definition of the Representative Volument Element in Numerical Homogenization Problems and Its Application to the Performance Evaluation of Analytical Homogenization Models, Ecole Polytechnique de Montréal, 2013.
[15] N. Provatas, M. Haataja, J. Asikainen, S. Majaniemi, M. Alava, T. Ala-Nissila, Colloids Surfaces A Physicochem. Eng. Asp. 165 (2000) 209.
[16] A. Ekman, A. Miettinen, T. Turpeinen, K. Backfolk, J. Timonen, Nord. Pulp Pap. Res. J. - Pap. Phys. 27 (2012) 270.
[17] A. Kulachenko, T. Uesaka, Mech. Mater. 51 (2012) 1.
[18] L.T. Curto, Joana M R, Eduardo, in:, XXI Tec. Conf. Exhib. CIADICYP, Lisbon, Portugal, 2010.
[19] Y. Pan, L. Iorga, A. a. Pelegri, Compos. Sci. Technol. 68 (2008) 2792.
[20] Q. Wang, B. Maze, H.V. Tafreshi, B. Pourdeyhimi, Model. Simul. Mater. Sci. Eng. 15 (2007) 855.
[21] E. Ghossein, M. Lévesque, J. Comput. Phys. 253 (2013) 471.
[22] E. Ghossein, M. Lévesque, Int. J. Solids Struct. 49 (2012) 1387.
[23] H. Altendorf, D. Jeulin, Phys. Rev. E 83 (2011) 041804.
[24] D. Rodney, M. Fivel, R. Dendievel, Phys. Rev. Lett. 95 (2005) 108004.
[25] J. Moscinski, Bargiel Monika, Rycerz; Katarzyna, Jacobs Patrick, Mol. Simul. 3 (1989).
[26] G. Gaiselmann, D. Froning, C. Tötzke, C. Quick, I. Manke, W. Lehnert, V. Schmidt, Int. J. Hydrogen Energy 38 (2013) 8448.
[27] C.G. Joung, N. Phan-Thien, X.J. Fan, J. Nonnewton. Fluid Mech. 99 (2001) 1.
[28] S. Jung, (2009) 1993.
[29] G. Ulrich, J. R. Stat. Soc. 33 (1984) 158.
[30] W. Mattson, B.M. Rice, Comput. Phys. Commun. 119 (1999) 135.

[P3]: Stiffness prediction of statistically equivalent fibre networks representative of a specific mineral wool material

Stiffness prediction of statistically equivalent fibre networks representative of a specific mineral wool material

L. Chapelle[1,2], M. Lévesque[3], L. Pilgaard Mikkelsen[2], M. R. Foldschack1, Y. Kusano[2], P. Brøndsted[2]

[1]Group Development, ROCKWOOL International A/S,
Hovedgaden 584, DK-2640 Hedehusene, Denmark

[2]Department of Wind Energy, Technical University of Denmark
P.O. Box 49, Frederiksborgvej 399, DK-4000 Roskilde, Denmark

[3] Laboratory for Multiscale Mechanics (LM2), CREPEC, Départment of Mechanical Engineering, École Polytechnique de Montréal, Montréal, QC, H3C3A7, Canada

Abstract

A virtual fibre network where a fibre is modelled as a chain of spherocylinder is generated. The parameters for the generation are estimated from the characterization of a mineral wool sample. The generated volume is statistically representative of a mineral wool material and is then used in a finite-element model where fibres are modelled as beams and solved for its elastic properties. The variations of the elastic properties are studied with respect to the size and type of boundary conditions. Both periodic boundary conditions and periodic mixed uniform boundary conditions are considered and lead to the same elastic properties when the size of the volumes considered becomes sufficiently large. For large volumes, the numerically determined elastic properties indicate that the generated volumes present a transverse isotropic behaviour. Comparing with experimental results from the literature, we conclude that the model proposed where the fibre is modelled with beam elements succeeds in predicting accurately the stiffness of mineral wool fibres networks.

1. Introduction

Mineral wool designates the random network of inorganic fibres held together by an organic binder. Mineral wool products are widely used in the building industry as a thermal or acoustic insulator. In recent years, focus on the mechanical properties of mineral wool has intensified as a result of the development of new business segments where mineral wool

products have become part of the load bearing structures in the building envelope. Mineral wool fibres network´s mechanical properties are closely related to the fibres arrangement as well as their morphology.

Numerical homogenization can be used to relate overall properties to that of local constituents. Numerical homogenization relies on the microstructure´s automatic generation. Recently, several approaches inspired by molecular dynamics simulations have been proposed for the automatic generation of a microstructure with non-overlapping inclusions. Bezrukov and Stoyan have developed an algorithm for the generation of random packing of ellipsoids of revolution where contacts between the ellipsoids were detected and virtual forces was applied to translate and rotate the overlapping particles [68]. Ghossein and Lévesque used an event driven molecular dynamics algorithm to generate spheres and ellipsoids with a very high aspect ratio in a hard-core packing configuration [69]. Altendorf et al modelled a fibre as a chain of sphere with a controllable curvature and high volume fraction [46]. Gaiselmann et al. adopted the same chain of sphere model but with random 3D polygonal tracks to represent the fibre centreline [72]. In the two later examples, the system of fibres is then transformed into a non-overlapping fibre network by using a virtual force to reduce the overlap as described by [68] and additional virtual forces to keep the fibre structure. In this paper, the algorithm presented by Altendorf is implemented but some modifications are brought in order to fit better our application.

The evaluation of the effective properties of the automatic generated network requires that the volume generated is a representative volume element (RVE). The RVE is defined as a volume large enough to represent the geometry of the product and small enough to limit the computational costs. FEM is commonly used to solve for the effective properties of an RVE and is a powerful tool to gain insight in the mechanical properties of complex fibre materials. The influence of the boundary conditions on the computation of the effective properties of a material has been addressed by several papers in the literature. The kinematic uniform boundary conditions (KUBC) and the periodic boundary conditions (PBC) are the most extensively used boundary conditions in numerical homogenization. In general, for volume elements that are not representative, the boundary conditions give different elastic properties. When the volume element is representative, all boundary conditions converge towards effective properties. PBC were found to converge faster towards the exact effective than

KUBC [89]. We consider as well in this study the mixed uniform boundary conditions (MUBC) introduced by Hazanov et al. which combine uniform displacement and traction constraints [108]. Pahr and Zysset demonstrated that a special case of the MUBC, designated as periodicity compatible mixed uniform boundary conditions (PMUBC) were equivalent to the PBC. In [109], the PMUBC showed good convergence properties when applied to bone tissue.

To the authors´ best knowledge, there are currently no numerical models describing accurately the complex 3D architecture of mineral wool fibres (in terms of fibre morphology and orientation). For that reason, we use a the algorithm proposed by Altendorf and Jeulin [46] to generate fibre networks mimicking the real arrangement of the fibre in a mineral wool sample. The finite-element strategy is presented and the capabilities of the model will be illustrated by showing the results of a study of the variations of the component of the stiffness tensor with respect to two types of boundary conditions (PBC and PMUBC) and to the size of the generated volume element. The following convention has been adopted, unless specified otherwise: scalars are denoted by italic lower case letters (i.e. *a*); column vectors and matrices are denoted by italic boldfaced lower case letters (i.e. ***a***) and italic boldfaced upper case Latin letters (i.e. ***A***).

2. Methods

2.1 Generation of a virtual fibre network for mineral wool material

2.1.1 Generation algorithm developed by Altendorf and Jeulin

For the generation of a virtual periodic fibre network, the approach from Altendorf and Jeulin presented in details in [46] is implemented in MATLAB [73]. Thereby, a fibre is modelled as a chain of overlapping spheres where the main direction of the chain is controlled by an orientation distribution depending on a parameter β. This orientation distribution was first introduced in [45]. The density associated to this distribution is the function $p_\beta(\theta, \varphi)$ of elevation angle $\theta \in [0, \pi[$, azimuth angle $\varphi \in [0, \pi[$ and anisotropy parameter β is a real positive scalar given in Eq. 2.1.

$$p_\beta(\theta, \varphi) = \frac{1}{4\pi} \frac{\beta \sin\theta}{(1 + (\beta^2 - 1)\cos\theta)^{3/2}} \tag{0.1}$$

When β is set to the value of 1, the generated orientation vectors are uniformly distributed on the unit sphere. For increasing values of β, the fibers tend to be more and more horizontally orientated. For low values of β, the distribution concentrates around the z-axis.
The orientation of each individual spheres of the chain depends on the main fibre orientation vector drawn from the density function of Eq. 2.1 and the orientation of its previous neighbour in the chain. Practically, this is achieved by using a multivariate von Mises-Fisher distribution with two preferred orientations. The probability density function of a multivariate von Mises-Fisher distribution for a vector $\boldsymbol{u}$ with two preferred direction vectors $\boldsymbol{\mu_1}$ and $\boldsymbol{\mu_2}$ and two concentration parameters $\kappa_1$and κ_2 is given in Eq. 2.1.

$$f(u|\boldsymbol{\mu_1}, \kappa_1, \boldsymbol{\mu_2}, \kappa_2) = \frac{|\kappa_1\boldsymbol{\mu_1} + \kappa_2\boldsymbol{\mu_2}|}{2\pi(e^{|\kappa_1\boldsymbol{\mu_1}+\kappa_2\boldsymbol{\mu_2}|} - e^{-|\kappa_1\boldsymbol{\mu_1}+\kappa_2\boldsymbol{\mu_2}|})} e^{\left(\kappa_1{\boldsymbol{\mu_1}}^T\boldsymbol{u}+\kappa_2{\boldsymbol{\mu_2}}^T\boldsymbol{u}\right)^T\boldsymbol{u}} \tag{2.2}$$

This approach is particularly attractive for mineral wool fibre networks which present a certain degree of curvature. However, the implementation for the generation of a virtual volume of mineral wool fibres does not succeed in representing in a realistic manner the curvature observed in mineral wool fibres. Some modifications are thus brought to the algorithm to best adapt to the case of a mineral wool material and as a result, an alternative fibre model is proposed in this paper.

2.1.2 The spherocylinder fibre model

In the present work, a fibre is discretized as a chain of overlapping spherocylinders (Figure 2.1). To create a fibre, the position of a point $\boldsymbol{x_A}$, which corresponds to a centre of a sphere contained in one end of the spherocylinder, is drawn from a uniform distribution over the intervals $[0; L_x]$, $[0; L_y]$ and $[0; L_z]$ where L_x, L_y and L_z gives the size of the generation cell. From there the position of the second point $\boldsymbol{x_B}$, which corresponds to a centre of another sphere, contained in the other end of the first spherocylinder, is computed using the orientation unit vector $\boldsymbol{\mu_A}$ and the height of the spherocylinder l_A. The overall process for the generation of one spherocylinder element of a fibre is summarized in Eq. (2.3).

$$\boldsymbol{x_B} = \boldsymbol{x_A} + \boldsymbol{\mu_A} \cdot l_A \tag{2.3}$$

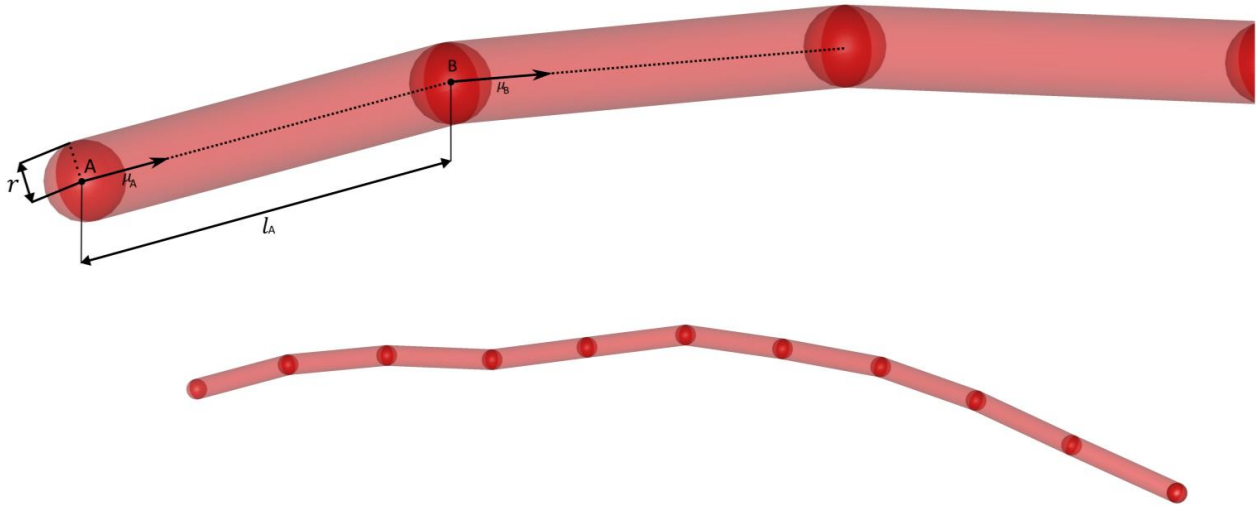

Figure 2.1: Representation of the spherocylinders chain model.

2.1.3 Reduction of the overlaps in the spherocylinders fibre model

To transform the fibre network into a non-overlapping system, translations are applied as described in [46]. In the present work, the translation required to reduce the overlap is implemented differently than in [46] as the model for a fibre is changed from a chain of overlapping spheres to a chain of overlapping spherocylinders. To determine if two fibres overlap with each other, the minimal distance between the centreline of two neighbouring spherocylinders is determined. If the minimal distance is less than the sum of the radii of the spherocylinders, an overlap is detected. To reduce the overlap, a translation proportional to the overlap is applied to the points of the spherocylinders corresponding to the minimal distance. The detailed implementation of the search of the points leading to the minimal distance between two spherocylinders is given in appendix A. The spherocylinders are also given an axial and rotational stiffness. Therefore when they move to supress the overlaps, they become subjected together with their close neighbours to translations and rotations as defined in [46] to limit the bending and the stretching of a spherocylinder with respect to the other spherocylinders of a fibre. To increase the speed of the search of overlapping spherocylinders, the candidates for the search are built using a nearest neighbour list.

2.2.3 Fitting to a mineral wool product

The fibre orientation and diameter distributions of a typical mineral wool product were obtained by X-ray computed tomography. In this case, the product under consideration is a stone wool light-density product. The orientation distribution is fitted to the density function

of Eq. (2.1) and the fibre diameter distribution is fitted to a lognormal function. The curvature parameters are roughly estimated after several numerical experiments and the values giving the best visual agreement with the real data was selected. Further work on the image analysis of the data will be conducted in the future to assess the curvature parameters in a more rigorous manner. The length of the fibres could not be determined from X-ray computed tomography data because the volumes considered are too small to include the full length a mineral wool fibre. For this study, it is decided that the fibre length will be kept constant and 250 times higher than the fibre diameter. The parameters selected for the generation of the virtual fibre structure are given in Table 2.1.

Table 2.1: Parameters for the generation of a virtual mineral wool fibre network.

Fibre orientation	β function (Eq. 1)	1.7
Fibre diameter	lognormal (mean fibre diameter: $\bar{d}$)	$\bar{d} = 4.00 \pm 2\ \mu m$
Fibre curvature	multivariate von Mises-Fischer (Eq. 2)	$\kappa_1 = 100$ and $\kappa_2 = 1$
Fibre volume fraction	-	1 %

2.2 Numerical homogenization

2.2.1 Boundary conditions

Two types of boundary conditions were selected: periodicity compatible mixed uniform boundary conditions (PMUBC) and periodic boundary conditions (PBC).

To enforce the PBC, the following conditions on the displacements at the boundaries are applied (Eq. (2.4)).

$$\boldsymbol{u_i^{k+}} - \boldsymbol{u_i^{k-}} = \varepsilon_{ij}^0 \left(\boldsymbol{x_j^{k+}} - \boldsymbol{x_j^{k-}}\right) \tag{2.4}$$

where $\boldsymbol{u_i^{k+}}$ and $\boldsymbol{u_i^{k-}}$ are the displacements on two opposite boundary surfaces$(i = 1,2,3)$, ε_{ij}^0 a component of the applied strain field ε^0 and $\boldsymbol{x_j^{k+}}$ and $\boldsymbol{x_j^{k-}}$ the coordinates of two points on opposite boundary surfaces. The right side of the equation is constant as the term $\left(\boldsymbol{x_j^{k+}} - \boldsymbol{x_j^{k-}}\right)$ is constant for each pair of the parallel boundary surfaces.

The PMUBC developed by Pahr et al. [90] combine strain and stress constraint. Table 2.2 details the sets of boundary conditions for a normal and shear strain case. The definitions of the face are given in Figure 2.2. The other loading cases are defined in a similar fashion. The

variables u_i and t_i for $i = 1,2,3$ are respectively the components of the displacements and tractions vectors on the boundary.

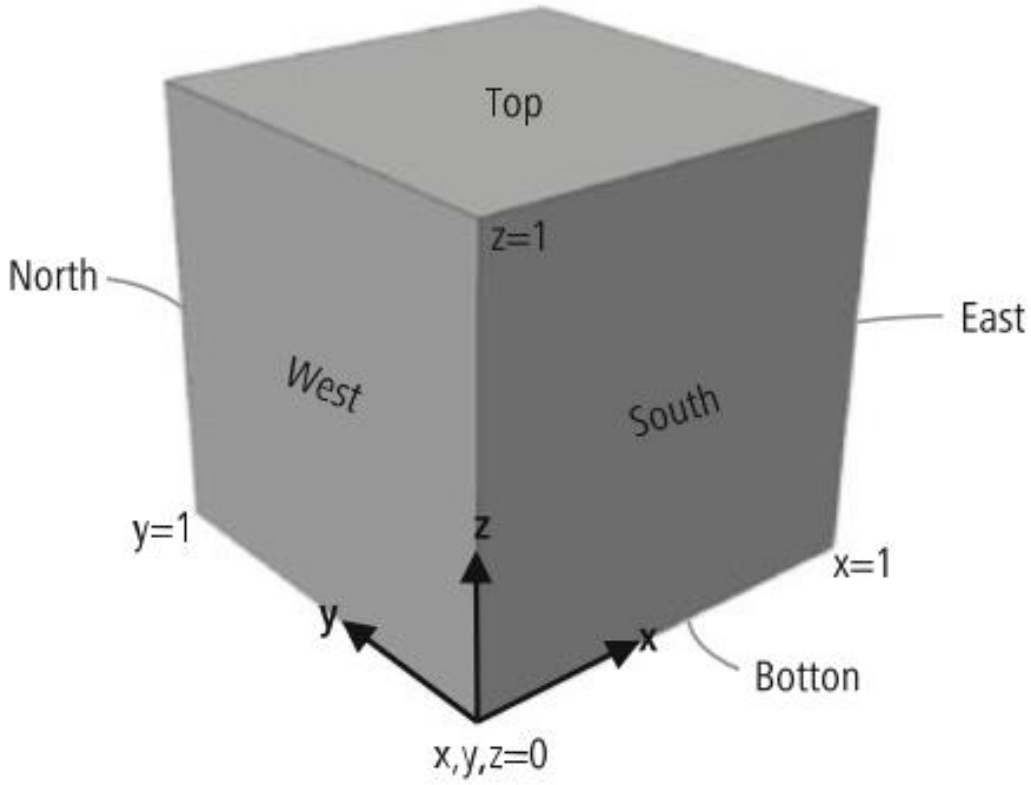

Figure 2,2: Definition of the face of the simulation cell (from [109]).

Table 2.2: PMUBC for a normal case and a shear case.

Load case	Top	Bottom	East	West	North	South
x-tension	$t_1 = 0$ $t_2 = 0$ $u_3 = 0$	$t_1 = 0$ $t_2 = 0$ $u_3 = 0$	$u_1 = -L\varepsilon_{11}/2$ $t_2 = 0$ $t_3 = 0$	$u_1 = L\varepsilon_{11}/2$ $t_2 = 0$ $t_3 = 0$	$t_1 = 0$ $u_2 = 0$ $t_3 = 0$	$t_1 = 0$ $u_2 = 0$ $t_3 = 0$
xy-shear	$t_1 = 0$ $t_2 = 0$ $u_3 = 0$	$t_1 = 0$ $t_2 = 0$ $u_3 = 0$	$t_1 = 0$ $u_2 = -L\varepsilon_{12}/2$ $t_3 = 0$	$t_1 = 0$ $u_2 = -L\varepsilon_{12}/2$ $t_3 = 0$	$u_1 = -L\varepsilon_{12}/2$ $t_2 = 0$ $t_3 = 0$	$u_1 = L\varepsilon_{12}/2$ $t_2 = 0$ $t_3 = 0$

2.2.2 Determination of the components of the stiffness tensor

The apparent elastic tensor $\boldsymbol{C}$ of a volume element element is computed through:

$$\boldsymbol{\Sigma} = \boldsymbol{C}\boldsymbol{E} \tag{2.5}$$

where $\boldsymbol{\Sigma}$ and $\boldsymbol{E}$ are the macroscopic stress and strain tensor.

In order to obtain all the components of the apparent elasticity tensor C, each generated fibre network is solved using 6 deformations states:

$$\boldsymbol{E}^1 = \begin{bmatrix} \varepsilon \\ 0 \\ 0 \\ 0 \\ 0 \\ 0 \end{bmatrix} \quad \boldsymbol{E}^2 = \begin{bmatrix} 0 \\ \varepsilon \\ 0 \\ 0 \\ 0 \\ 0 \end{bmatrix} \quad \boldsymbol{E}^3 = \begin{bmatrix} 0 \\ 0 \\ \varepsilon \\ 0 \\ 0 \\ 0 \end{bmatrix} \quad \boldsymbol{E}^4 = \begin{bmatrix} 0 \\ 0 \\ 0 \\ \varepsilon \\ 0 \\ 0 \end{bmatrix} \quad \boldsymbol{E}^5 = \begin{bmatrix} 0 \\ 0 \\ 0 \\ 0 \\ \varepsilon \\ 0 \end{bmatrix} \quad \boldsymbol{E}^6 = \begin{bmatrix} 0 \\ 0 \\ 0 \\ 0 \\ 0 \\ \varepsilon \end{bmatrix} \tag{2.6}$$

Each deformation state gives a column of the apparent elastic tensor. To obtain the average of the stress over the volume considered, the reaction force at the reference points where the displacement was imposed are extracted and the stress are derived by dividing the resulting reaction force by the area of the face of the volume at the boundary considered.

2.3 Implementation

The FEM model is built in Abaqus [110]. The fibres are modelled as 1D Timoshenko beam elements. The mesh convergence is obtained with 3 elements per fibre. The bonds between the fibres created by the binder are modelled as springs with axial and rotational stiffness (connector elements in Abaqus). The creation of a bond between two fibres depends on the distance between these two fibres. When the distance between two fibres surfaces is below an adjustable threshold (in this study 0.05 mm), a bond is created. The bonds are shows in red in Figure 2.3.

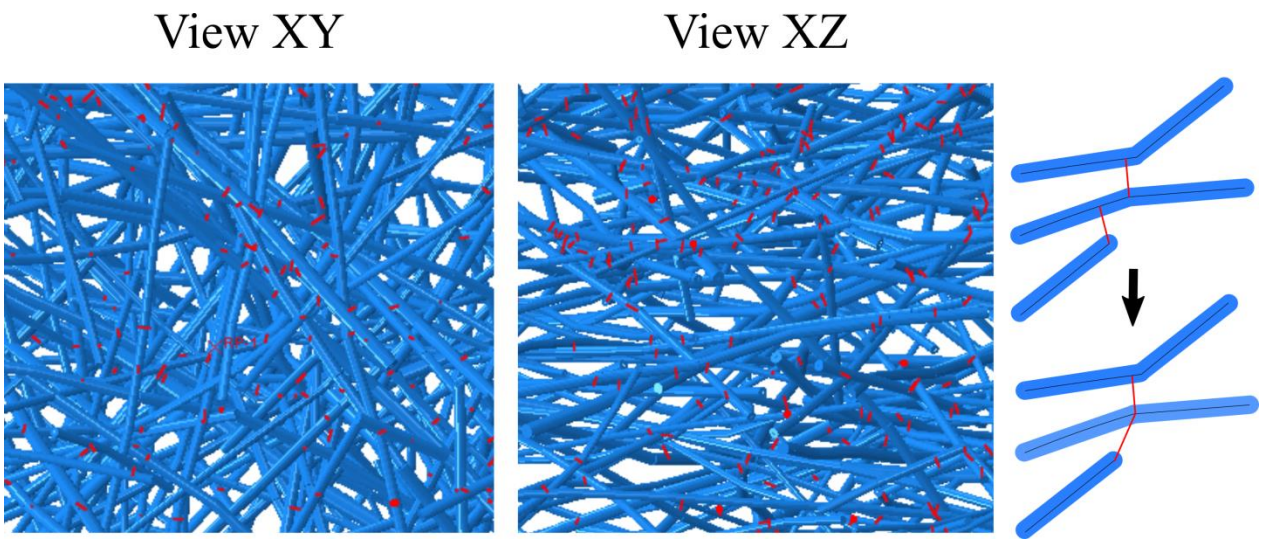

Figure 2.3: View of fibre network model where the red segments represent the connector element between the beam elements.

A quasi-static analysis is run using an explicit procedure. In the explicit dynamics procedure, out-of-balance forces are propagated as stress waves between neighbouring elements. The time increment of the simulation is a function of the smallest characteristic element length, the material Young's modulus and the material density. By increasing the material density and the element size, we can reduce the time increment and obtain an optimal solution with respect to the computational time of the quasi-static simulation. In practise, we use the mass scaling option in Abaqus to scale the time increment and accelerate the simulation.
The energy balance between the kinetic energy and the internal energy is checked in order to evaluate if the solution represents a quasi-solution response. In order to avoid small elements that would slow down the simulation, the nodes created by the connectors along the fibre axis are merged to any other nodes within a distance of 0.05 (Figure 2.3).

The constraints on nodal displacements at the boundaries are implemented by defining equations constraints and using dummy nodes. The dummy nodes are introduced through reference points which are not directly linked to the model. A displacement is imposed to the dummy node to represent the quantity $\varepsilon_{ij}^{0}\left(\boldsymbol{x_j^{k+}} - \boldsymbol{x_j^{k-}}\right)$. A Python script was written to pair the nodes of a face with their periodic nodes on the opposite face and impose periodic displacement using the equation option in Abaqus and dummy nodes.

PMUBC were simpler to implement: the displacements of the nodes at the different boundaries of the cell were linked respectively to six different dummy nodes (one for each face). The external strain is applied through the six dummy nodes.

3 Results and discussion

In this section, the method for the generation of a random fibre network mimicking a mineral wool product is generated. The model convergence towards the effective properties is then evaluated in terms of boundary conditions and number of realizations. Finally, the obtained stiffness tensor is compared to the transverse isotropic case and the size of the RVE determined.

3.1 Generation of random fibre network

The random fibre networks used in the FEM simulations are generated according to the characteristics presented in Table 2. This leads to slender fibres with high aspect ratio, mostly oriented in the x-y plane and presenting a moderate curvature. A realization of a volume generated is given in Figure 3.1 with the corresponding histograms on a unit sphere of their fibre orientations. These histograms confirm that the orientation information of the generated fibres is not altered significantly during the transformation into a non-overlapping fibre network as they are almost identical.

The deviation angles for each element of a fibre before and after the removal of the overlaps is calculated for 30 generated networks of different sizes. The mean and maximal values are given in Table 3. While the orientation of a few elements of the fibres deviates significantly from their initial orientation, the orientation information entered as input is conserved as indicated by the low value of the mean deviation angle.

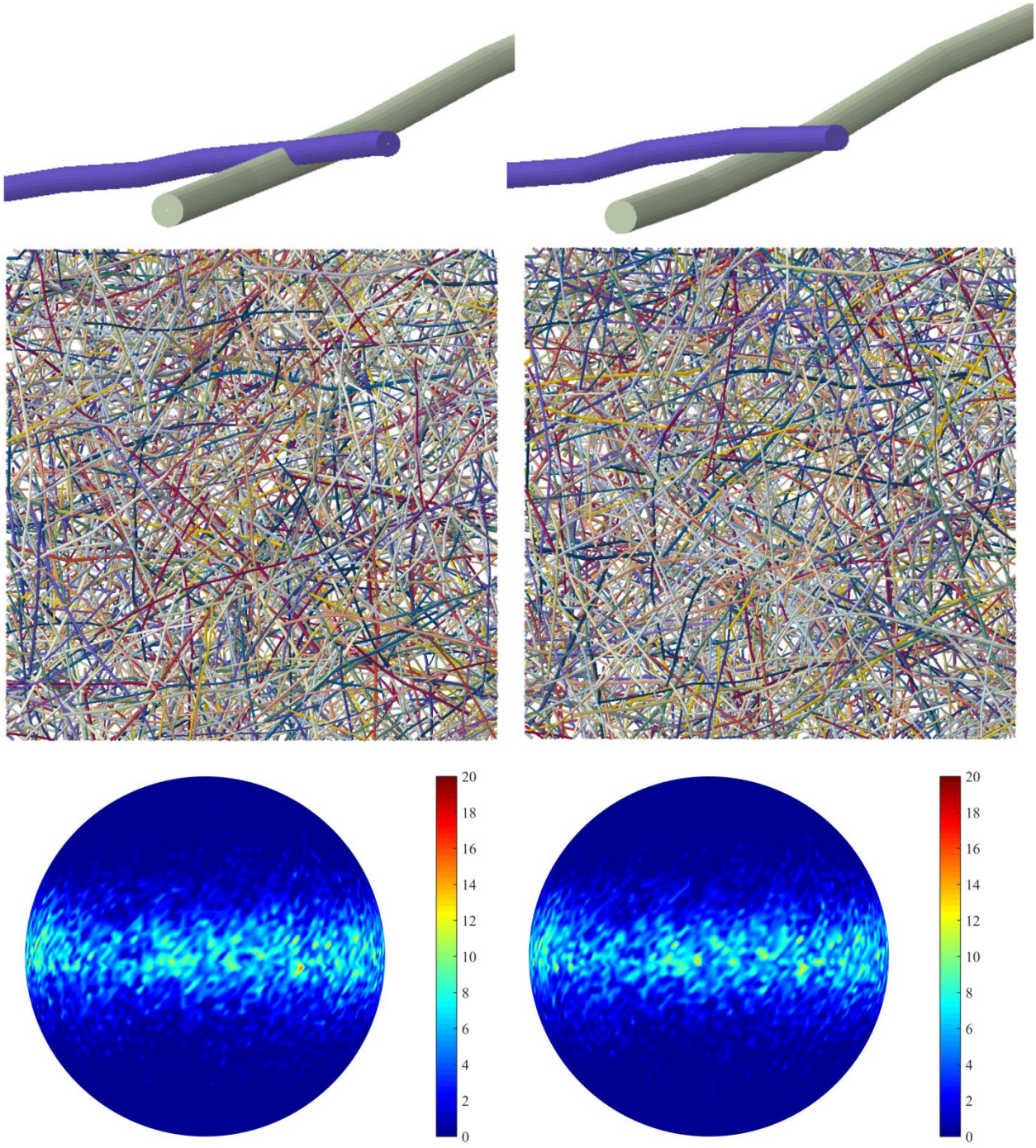

Figure 3.1: Fibres, fibre networks and histograms on the unit sphere of the orientations distribution before (left) and after (right) the reduction of overlaps.

Table 3.1: Deviation angles of the fibre orientation before and after the application of translation to reduce the overlaps.

Volume	Mean value of the deviation angle [rad]	Maximal value of the deviation angle [rad]

1.00	0.02	0.18
1.73	0.02	0.23
2.74	0.02	0.27
4.10	0.02	0.25
5.83	0.02	0.29
8.00	0.02	0.29

3.2 Convergence of PBC and PMUBC realizations with the volume size

PMUBC and PBC are studied over an increasing size of volume elements. The ratio of the volume element side length over the fibre length δ is used as an indicator of the size of the volume considered. This ratio δ varies from 1 to 2 with an increment of 0.2. For each type of boundary conditions, volume sizes and loading cases, 5 cubic volumes generated with the parameters from Table 3.1 are solved. Figure 3.2 shows the plots of the values of different components as a function of the parameter δ where the points represent the individual result of a simulation and the solid line the mean values for the 5 realizations for each δ.

The scale of the plot makes it difficult to see the variations for the largest volumes because the scatter of the data is large and the estimated values high for the smallest volumes. For that reason, the same plots are represented with different limits for the axis to focus on the convergence for the larger volumes.

When the parameter δ is less than 1.4, the apparent values of the stiffness components are largely overestimated and scatter over a wide range. The scatter is significantly reduced when δ becomes larger than 1.4. The overestimation and scatter of the stiffness components values are greater with the PMUBC than with the PBC for small volumes. As the size of the volume increases, the influence of the boundary type diminishes and the two boundary conditions converges from above towards the effective values for the components C_{11}, C_{22} and C_{33}, respectively 242 kPa, 254 kPa and 20 kPa.

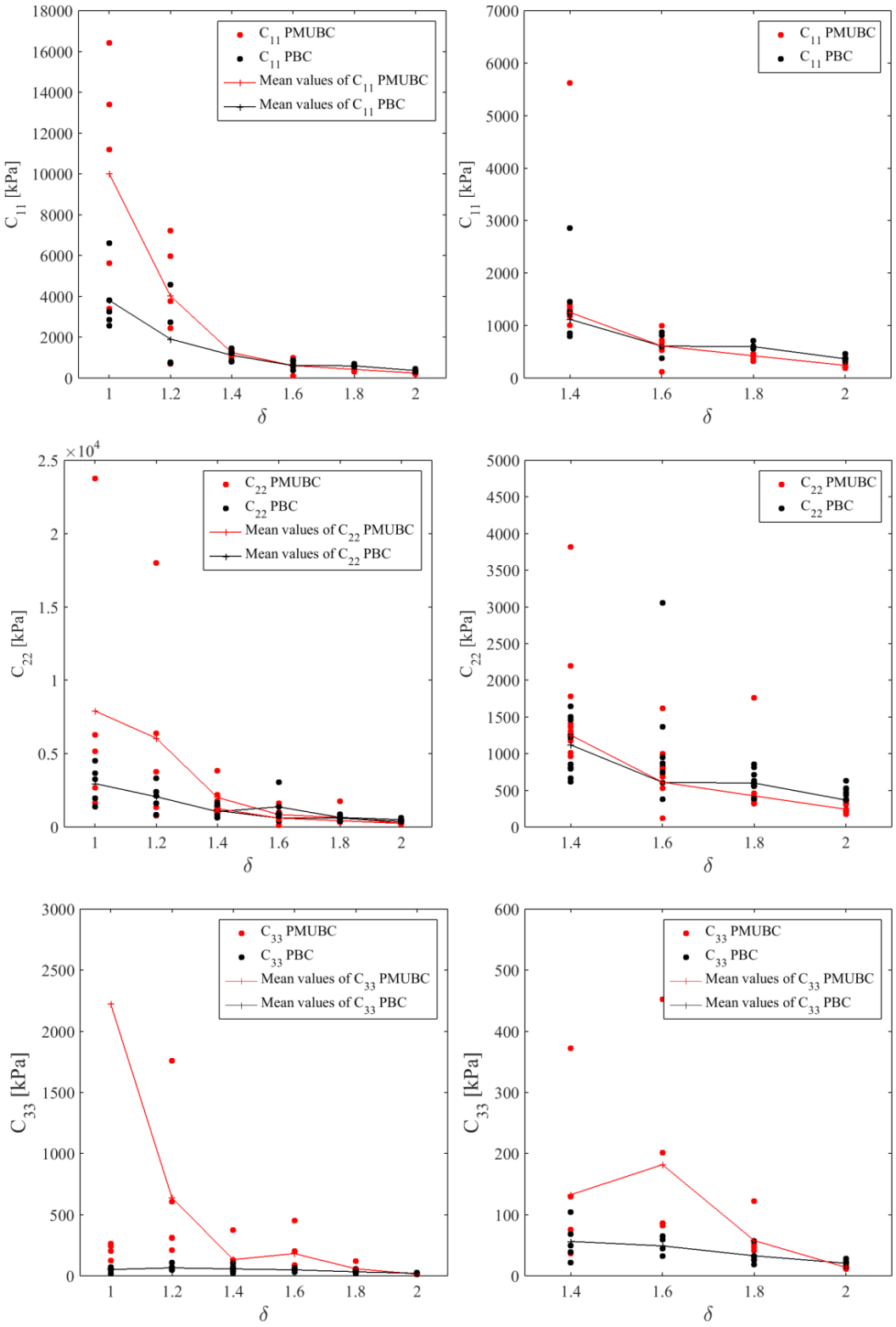

Figure 3.2: Convergence of C_{11} (top), C_{22} (middle) and C_{33} (bottom) as a function of δ, the ratio of the cell size over the fibre length.

Even though the PMUBC converge slower than the PBC towards the effective properties, they will be adopted for the rest of the study as they are faster to implement.

3.3 Convergence of the mean and standard deviation with the number of realizations

Because of the stochastic nature of the generated fibre networks, the values of the stiffness components vary from one realization to another. In this section, the variability of the stiffness components as a function of the number of realizations is studied by computing the relative error ε_{rel} of the component C_{11}.

The relative error is defined as follow:

$$\varepsilon_{rel} = \frac{2D_Z}{Z\sqrt{n}} \tag{3.1}$$

where D_Z is the standard deviation and $\bar{Z}$ the mean values of the apparent properties.

All simulations are performed on a cubic volume element with a side length twice as long as the fibre length. Results are presented in Figure 3.3.

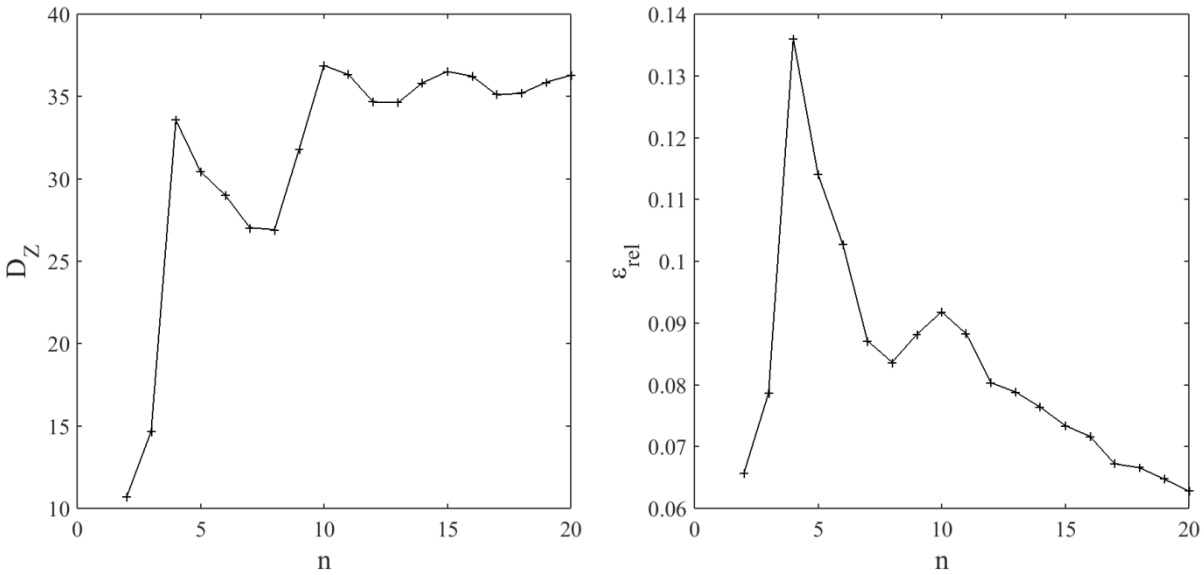

Figure 3.3: Convergence of the mean value (left) and the normalized standard deviation (right) of C_{11} as a function of the number of realizations.

The standard deviation varies drastically from 2 to 5 realizations but starts converging towards 0.15 after 5 realizations. After 10 realizations, the relative error is below 10% and after 20, below 7.5%.

3.4 Deviation from transverse isotropy

The orientations of the fibres drawn from the probability density function of Eq. (2.1) should create symmetry around the z-axis. It is therefore expected that the generated mineral wool network is transverse isotropic. In the transverse isotropic case, the following relationships between the components can be obtained:

$$\begin{aligned} C_{11} &= C_{22} \\ C_{13} &= C_{23} \\ C_{44} &= C_{55} \\ C_{66} &= \frac{C_{11} - C_{12}}{2} \end{aligned} \tag{3.2}$$

The aforementioned components are computed for 5 simulations with PMUBC for the 6 different sizes. The results of the computation are shown in Figure 3.4. We observed that C_{11} and C_{22} starts converging towards the same value when δ reaches 1.6. The C_{13} and C_{23} components exhibit a similar behaviour. We also verify that C_{44} and C_{55} are equal to each other.

The components of the transverse isotropic stiffness tensor are computed by calculating the mean and standard deviation for the 5 volumes where δ is equal to 2.

$$\boldsymbol{C} = \begin{pmatrix} 241.5 \pm 66.9 & 16.4 \pm 9.36 & 1.6 \pm 1.9 & 0 & 0 & 0 \\ 20.0 \pm 20.9 & 254.6 \pm 86.5 & 1.7 \pm 1.0 & 0 & 0 & 0 \\ 2.1 \pm 0.7 & 2.2 \pm 1.1 & 13.9 \pm 3.0 & 0 & 0 & 0 \\ 0 & 0 & 0 & 50.5 \pm 4.9 & 0 & 0 \\ 0 & 0 & 0 & 0 & 51.1 \pm 6.8 & 0 \\ 0 & 0 & 0 & 0 & 0 & 74.3 \pm 4.7 \end{pmatrix} \tag{3.3}$$

There exist only a few papers dealing with the characterization of the stiffness component of mineral wool. Tarnow [92] reported values of 390 kPa and 16 kPa respectively for the C_{11} and C_{33} components for a glass wool sample with a fibre volume fraction of 2%. Witz et al. [93] obtained a similar value for the same components C_{11} = 353 kPa and a lower value for $C_{33} = 1.53$ kPa. The discrepancy between the values of C_{11} reported in the literature and the one we computed can be explained than the fibre network has been fitted to data from a stone wool sample where the orientation of the fibres is not as lamellar as the orientation of the glass wool fibres.

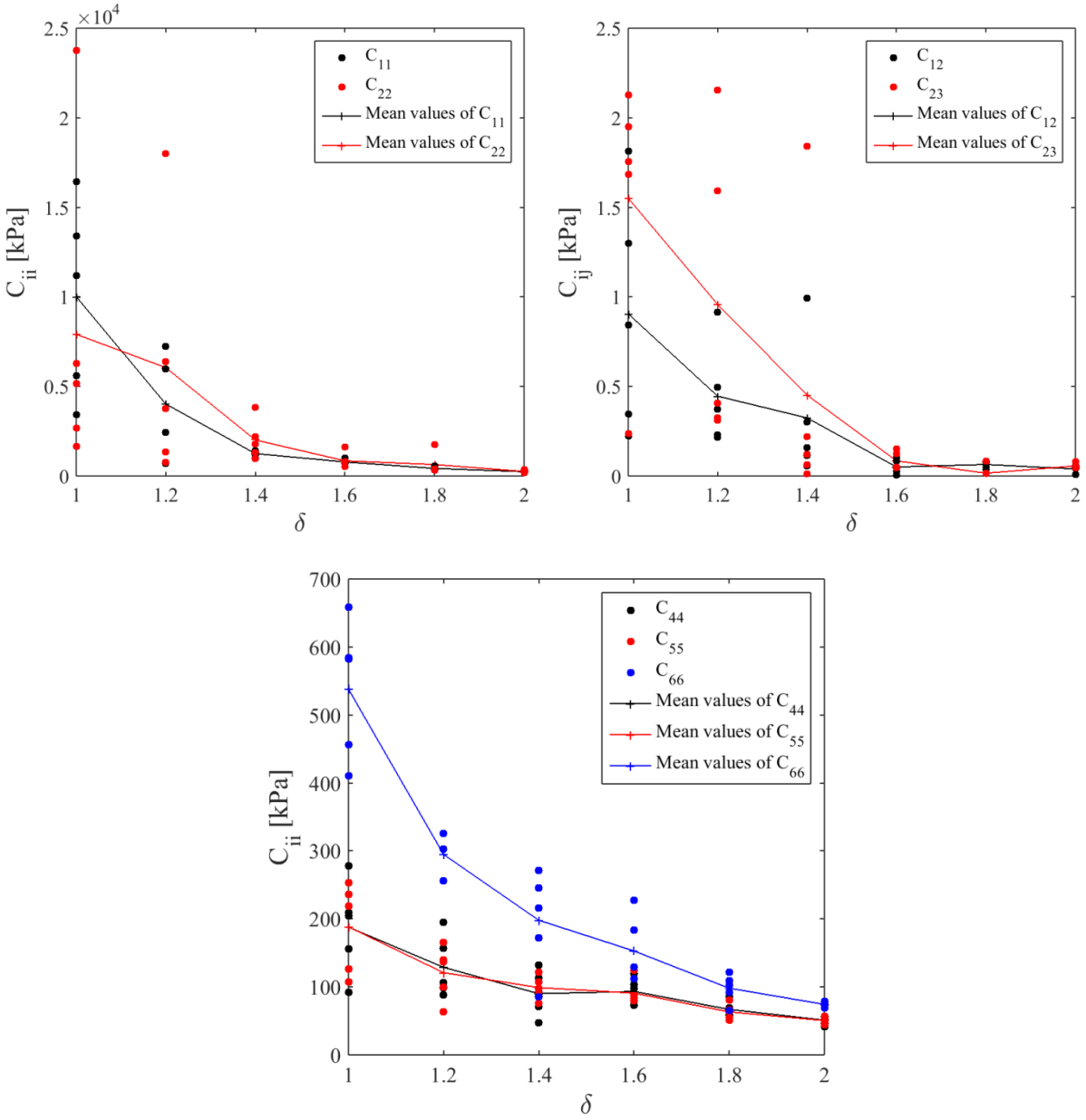

Figure 3.4 : Convergence of different components of the stiffness as a function of δ, the ratio of the cell size over the fibre length for PMUBC.

4 Conclusion

Non overlapping virtual fibre networks have been generated by implementing a modified version of the algorithm of Altendorf and Jeulin. In the new implementation developed here, the fibre is modelled as a chain of spherocylinders. Modification of the fibre model result in changes in the overlap detection algorithm and we have presented here a method to find the shortest distance between two spherocylinders. The generated volumes are representative of the real mineral wool fibre networks since the inputs for the generation have been estimated from the characterization of a real sample of mineral wool. We have

confirmed that the removal of the overlaps does not cause a change in the main fibre orientation as entered as inputs.

The elastic properties are predicted using the generated geometries in a FEM model where the fibres are modelled with beam elements. The estimated properties depend greatly on the size of the volume considered for the simulation and the type of boundary applied. We have studied the effect of two types of boundary conditions: the PBC and the PMUBC. For sufficient large volumes, both types of boundary conditions give equivalent results. As the results of the simulation become independent of the type of boundary conditions for the large volumes, we can conclude that these volumes are representative volume elements.
As expected, the relative error decreases with the number of realizations. After 10 realizations, the relative becomes less than 10 %.

Finally, we confirmed that the tensor obtained by the simulation is indeed transverse isotropic and we have studied the deviation from the transverse isotropic case as a function of the volume size. Already volumes with a side 1.6 times longer than the fibre length show a strong transverse isotropic behaviour.

References

[1] A. Bezrukov, D. Stoyan, Part. Part. Syst. Charact. 23 (2006) 388.

[2] E. Ghossein, M. Lévesque, J. Comput. Phys. 253 (2013) 471.

[3] H. Altendorf, D. Jeulin, Phys. Rev. E 83 (2011) 041804.

[4] G. Gaiselmann, D. Froning, C. Tötzke, C. Quick, I. Manke, W. Lehnert, V. Schmidt, Int. J. Hydrogen Energy 38 (2013) 8448.

[5] T. Kanit, S. Forest, I. Galliet, V. Mounoury, D. Jeulin, Int. J. Solids Struct. 40 (2003) 3647.

[6] S. Hazanov, M. Amieur, Int. J. Eng. Sci. 33 (1995) 1289.

[7] T. Blöß, M. Welsch, Lect. Notes Appl. Comput. Mech. 74 (2015) 101.

[8] MATLAB, Version 8.15.0 (2015a), The MathWorks Inc., Natick, Massachusetts, 2015.

[9] D. Stoyan, J. Mecke, S. Pohlmann, Ser. Stat. 11 (1980) 281.

[10] D.H. Pahr, P.K. Zysset, Biomech. Model. Mechanobiol. 7 (2008) 463.

[11] Abaqus, Documentation, Notes 92 (2011) 815.

[12] V. Tarnow, J. Acoust. Soc. Am. 108 (2000) 2243.

[13] J.-F. Witz, S. Roux, F. Hild, J. Rieunier, J. Eng. Mater. Technol. 130 (2007) 1.

Appendix

We consider two lines L_1 and L_2 passing respectively through the pair of points (P_1, P_2) and (Q_1, Q_2). Let $\boldsymbol{u} = P_2 - P_1$ and $\boldsymbol{v} = Q_2 - Q_1$. The equations for the lines can be expressed as a function of the vectors $\boldsymbol{u}$ and $\boldsymbol{v}$, the points P_1 and P_2 and the parameters s and t:

$$P(s) = P_1 + s\boldsymbol{u}$$
$$Q(t) = Q_1 + t\boldsymbol{v}$$

There exist two points P_m and Q_m belonging respectively to L_1 and L_2 such as the distance between L_1 and L_2 at these points is minimal. The segment $[P_m Q_m]$ with direction vector $\boldsymbol{w} = Q_m - P_m$ is orthogonal to both lines L_1 and L_2.
This condition can be translated into the system of two equations:

$$\begin{cases} \boldsymbol{u}.\boldsymbol{w} = 0 \\ \boldsymbol{v}.\boldsymbol{w} = 0 \end{cases}$$

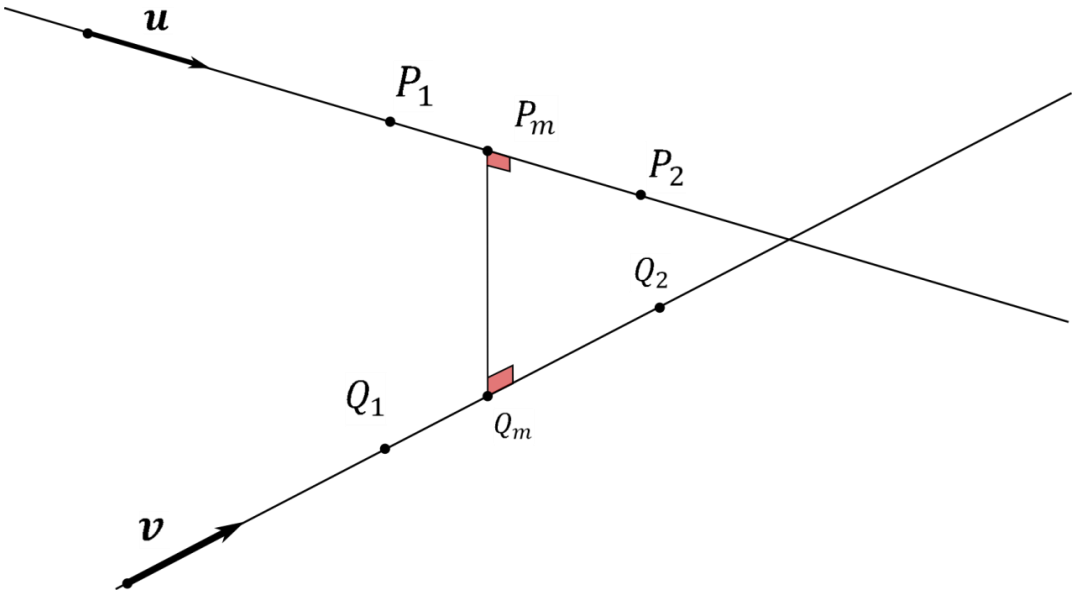

Figure 0.8: Representation of the different variables for the search of the shortest distance between two lines.

We set:

$\boldsymbol{w_1} = P_1 - Q_1$ and $\boldsymbol{w} = Q_m - P_m = P_0 + s_m\boldsymbol{u} - Q_0 - t_m\boldsymbol{v} = w_1 + s_m\boldsymbol{u} - t_m\boldsymbol{v}$

The system of equations becomes then:

$$\begin{cases} s_m(\boldsymbol{u}.\boldsymbol{u}) - t_m(\boldsymbol{u}.\boldsymbol{v}) = -\boldsymbol{u}.\boldsymbol{w_1} \\ s_m(\boldsymbol{v}.\boldsymbol{u}) - t_m(\boldsymbol{v}.\boldsymbol{v}) = -\boldsymbol{v}.\boldsymbol{w_1} \end{cases}$$

If $(\boldsymbol{u}.\boldsymbol{u})(\boldsymbol{v}.\boldsymbol{v}) - (\boldsymbol{u}.\boldsymbol{v})(\boldsymbol{u}.\boldsymbol{v}) \neq 0$, the solutions of the systems are:

$$s_m = \frac{(\boldsymbol{u}.\boldsymbol{v})(\boldsymbol{v}.\boldsymbol{w_1}) - (\boldsymbol{v}.\boldsymbol{v})(\boldsymbol{u}.\boldsymbol{w_1})}{(\boldsymbol{u}.\boldsymbol{u})(\boldsymbol{v}.\boldsymbol{v}) - (\boldsymbol{u}.\boldsymbol{v})(\boldsymbol{u}.\boldsymbol{v})}$$

$$t_m = \frac{(\boldsymbol{u}.\boldsymbol{u})(\boldsymbol{v}.\boldsymbol{w_1}) - (\boldsymbol{u}.\boldsymbol{v})(\boldsymbol{u}.\boldsymbol{w_1})}{(\boldsymbol{u}.\boldsymbol{u})(\boldsymbol{v}.\boldsymbol{v}) - (\boldsymbol{u}.\boldsymbol{v})(\boldsymbol{u}.\boldsymbol{v})}$$

The minimal distance between the two lines is then:

$$d_m = \left| w_0 + \frac{(\boldsymbol{u}.\boldsymbol{v})(\boldsymbol{v}.\boldsymbol{w_1}) - (\boldsymbol{v}.\boldsymbol{v})(\boldsymbol{u}.\boldsymbol{w_1})}{(\boldsymbol{u}.\boldsymbol{u})(\boldsymbol{v}.\boldsymbol{v}) - (\boldsymbol{u}.\boldsymbol{v})(\boldsymbol{u}.\boldsymbol{v})}\boldsymbol{u} - \frac{(\boldsymbol{u}.\boldsymbol{u})(\boldsymbol{v}.\boldsymbol{w_1}) - (\boldsymbol{u}.\boldsymbol{v})(\boldsymbol{u}.\boldsymbol{w_1})}{(\boldsymbol{u}.\boldsymbol{u})(\boldsymbol{v}.\boldsymbol{v}) - (\boldsymbol{u}.\boldsymbol{v})(\boldsymbol{u}.\boldsymbol{v})}\boldsymbol{v} \right|$$

If $(\boldsymbol{u}.\boldsymbol{u})(\boldsymbol{v}.\boldsymbol{v}) - (\boldsymbol{u}.\boldsymbol{v})(\boldsymbol{u}.\boldsymbol{v}) = 0$, the lines are parallel and the distance separating the lines is constants. The distance can be evaluated by setting one of the parameter and solving for the other.

Let R_m and T_m be the points corresponding to the shortest distance between two segments. R_m and T_m coincide respectively with the points P_m and Q_m unless one of the following conditions is met:

- If $s_m < 0$, the point P_m lies outside of the segment: the point R_m corresponding to the shortest distance between the two segments is P_1.
- If $s_m > 1$, the point P_m lies outside of the segment: the point R_m corresponding to the shortest distance between the two segments is P_2.
- If $t_m < 0$, the point Q_m lies outside of the segment: the point T_m corresponding to the shortest distance between the two segments is Q_1.
- If $t_m > 1$, the point Q_m lies outside of the segment: the point T_m corresponding to the shortest distance between the two segments is Q_2.